SANDIA REPORT

SAND2015-10859
Unlimited Release
Printed December 2015

Multi-scale Modeling of Plasticity in Tantalum

Hojun Lim, Corbett C. Battaile, Jay D. Carroll, Thomas E. Buchheit, Christopher R. Weinberger and Brad L. Boyce

Prepared by
Sandia National Laboratories
Albuquerque, New Mexico 87185 and Livermore, California 94550

Sandia National Laboratories is a multi-program laboratory managed and operated by Sandia Corporation,
a wholly owned subsidiary of Lockheed Martin Corporation, for the U.S. Department of Energy's
National Nuclear Security Administration under contract DE-AC04-94AL85000.

Sandia National Laboratories

Issued by Sandia National Laboratories, operated for the United States Department of Energy by Sandia Corporation.

NOTICE: This report was prepared as an account of work sponsored by an agency of the United States Government. Neither the United States Government, nor any agency thereof, nor any of their employees, nor any of their contractors, subcontractors, or their employees, make any warranty, express or implied, or assume any legal liability or responsibility for the accuracy, completeness, or usefulness of any information, apparatus, product, or process disclosed, or represent that its use would not infringe privately owned rights. Reference herein to any specific commercial product, process, or service by trade name, trademark, manufacturer, or otherwise, does not necessarily constitute or imply its endorsement, recommendation, or favoring by the United States Government, any agency thereof, or any of their contractors or subcontractors. The views and opinions expressed herein do not necessarily state or reflect those of the United States Government, any agency thereof, or any of their contractors.

Printed in the United States of America. This report has been reproduced directly from the best available copy.

Available to DOE and DOE contractors from
U.S. Department of Energy
Office of Scientific and Technical Information
P.O. Box 62
Oak Ridge, TN 37831

Telephone: (865) 576-8401
Facsimile: (865) 576-5728
E-Mail: reports@adonis.osti.gov
Online ordering: http://www.osti.gov/bridge

Available to the public from
U.S. Department of Commerce
National Technical Information Service
5285 Port Royal Rd
Springfield, VA 22161

Telephone: (800) 553-6847
Facsimile: (703) 605-6900
E-Mail: orders@ntis.fedworld.gov
Online ordering: http://www.ntis.gov/help/ordermethods.asp?loc=7-4-0#online

SAND2015-10859
Unlimited Release
Printed December 2015

Multi-scale Modeling of Plasticity in Tantalum

Hojun Lim* and Corbett C. Battaile and
Computational Materials and Data Science,
Sandia National Laboratories, MS 1411, Albuquerque, NM 87185
*hnlim@sandia.gov

Jay D. Carroll, Thomas E. Buchheit and Brad L. Boyce
Metallurgy and Materials Joining,
Sandia National Laboratories, MS 0889, Albuquerque, NM 87185

Christopher R. Weinberger
Department of Mechanical Engineering and Mechanics,
Drexel University, Philadelphia, PA 19104

Abstract

In this report, we present a multi-scale computational model to simulate plastic deformation of tantalum and validating experiments. In atomistic/ dislocation level, dislocation kink-pair theory is used to formulate temperature and strain rate dependent constitutive equations. The kink-pair theory is calibrated to available data from single crystal experiments to produce accurate and convenient constitutive laws. The model is then implemented into a BCC crystal plasticity finite element method (CP-FEM) model to predict temperature and strain rate dependent yield stresses of single and polycrystalline tantalum and compared with existing experimental data from the literature. Furthermore, classical continuum constitutive models describing temperature and strain rate dependent flow behaviors are fit to the yield stresses obtained from the CP-FEM polycrystal predictions. The model is then used to conduct hydrodynamic simulations of Taylor cylinder impact test and compared with experiments.

In order to validate the proposed tantalum CP-FEM model with experiments, we introduce a method for quan- titative comparison of CP-FEM models with various experimental techniques. To mitigate the effects of unknown subsurface microstructure, tantalum tensile specimens with a pseudo-two-dimensional grain structure and grain sizes on the order of millimeters are used. A technique combining an electron back scatter diffraction (EBSD) and high resolution digital image correlation (HR-DIC) is used to measure the texture and sub-grain strain fields upon uniaxial tensile loading at various applied strains. Deformed specimens are also

analyzed with optical profilometry measurements to obtain out-of- plane strain fields. These high resolution measurements are directly compared with large-scale CP-FEM predictions.

This computational method directly links fundamental dislocation physics to plastic deformations in the grain-scale and to the engineering-scale applications. Furthermore, direct and quantitative comparisons between experimental measurements and simulation show that the proposed model accurately captures plasticity in deformation of polycrystalline tantalum.

Acknowledgment

This work is supported by the Predicting Performance Margins (PPM), Campaign 2 - Dynamic Materials Properties (C2-DMP) and Advanced Simulation and Computing - Physics and Engineering Models (ASC-P&EM) programs at Sandia National Laboratories.

Sandia National Laboratories is a multi-program laboratory managed and operated by Sandia Corporation, a wholly owned subsidiary of Lockheed Martin Corporation, for the U.S. Department of Energys National Nuclear Security Administration under contract DE-AC04-94AL85000.

Contents

Figures

Tables

Nomenclature

BCC Body Centered Cubic

CP-FEM Crystal Plasticity Finite Element Method

DIC Digital Image Correlation

EBSD Electron Back Scatter Diffraction

EDM Electro-Discharge Machining

EI model Elastic Interaction model

FCC Face Centered Cubic

FEM Finite Element Method

JC model Johnson-Cook model

LT model Line Tension model

MTS model Mechanical Threshold Stress model

OIM Orientation Imaging Microscopy

RRR Residual Resistance Ratio

SEM Scanning Electron Microscopy

ZA model Zerilli-Armstrong model

1 Introduction

Tantalum is a body-centered-cubic (BCC) transition metal that is widely used in many high temperature and strain rate applications. Despite strong scientific and engineering interests in BCC refractory metals such as tantalum, molybdenum, tungsten and niobium, they are generally underrepresented in computational materials science studies due to complex response compared to close-packed structured metals. For example, BCC metals are well-known to exhibit strong temperature and strain rate dependent flow and non-Schmid yield behavior [32, 96, 39, 103, 73]. These characteristics deviate from many close-packed metals, specifically those that are face-centered-cubic (FCC).

Various BCC computational models were developed at different length scales to capture these experimentally observed characteristics in BCC metals. In atomistic/dislocation level, dislocation kink-pair theory based on the thermally activated motion of screw dislocations is developed to describe the strong temperature and strain rate dependent flow stresses of various BCC single crystals [91, 93, 22, 9]. These models are based on a transition state theory and use the activation enthalpy to derive the temperature and strain rate dependent flow rule. The model successfully reproduced temperature and strain rate dependent flow behavior of tantalum [106], molybdenum [53, 52], tungsten [20] and niobium [94]. In continuum level, different analytical models are developed to reproduce the temperature and strain rate effects in polycrystalline BCC metals, e.g. Johnson-Cook (JC) [56, 55], Zerilli-Armstrong (ZA) [110] and Mechanical Threshold Stress (MTS) [41] models. These continuum models successfully reproduced temperature and strain rate dependent flow behaviors of various BCC polycrystals including Armco iron [56, 55, 110], steel alloys [56, 55], molybdenum [81, 30], tungsten and tungsten alloys, [56, 67], tantalum and tantalum alloys [111, 29, 82, 79, 85], niobium [79] and vanadium [80]. However, these analytical models are usually fit to macro-scale stress-strain response of polycrystals and only serve as a convenient fit to experimental data. Thus, most of these models in two length scales cannot provide descriptions of deformation at the scale of the microstructure.

Crystal plasticity (CP) models can be a convenient method to link these two extreme scales. In particular, modern crystal plasticity - finite element method (CP-FEM) models [86, 10, 6, 35], enforces inter-grain equilibrium and compatibility using a continuum finite elements and thus capable of incorporating heterogeneous grain structure with varying grain shapes, crystal orientations, and neighboring effects from other grains. However, most single crystal constitutive equations are developed specific to FCC metals, which exhibit far less dependence of the flow stress on temperature and strain rate as compared to BCC metals [86, 10, 34]. Most visco-plasitc constitutive formulations invoke a formulation that involves the rate of slip on individual slip systems [86, 11] but this is primarily a numerical device, and thus inappropriate for describing the physical temperature and strain rate dependence of the flow stress of BCC metals. Thus, the strain rate and temperature effects must be accounted for in the constitutive equations capturing these effects explicitly. While crystal plasticity models provide a link between the fundamental dislocation physics and continuum level response, no such complete models for BCC refractory metals have been developed.

In addition to complexities in modeling BCC metals, a direct and detailed comparison between the model predictions with experimental measurement have been very challenging. Although recent CP-FEM models successfully predicted texture and mechanical behaviors of polycrystalline FCC [6, 36, 87, 112, 99, 89, 7, 42], BCC [107, 103, 73, 4, 78] and HCP metals [76, 102, 1], as well as non-local size effects [84, 33, 72, 8], most of these models lack quantitative comparisons with experimental measurements. This limitation mainly attributed to the lack of information on subsurface microstructures [26] and different length scales in the simulations and experimental measurements. In order to overcome these obstacles in polycrystal specimens, many direct comparison of CP-FEM and experiments are conducted with a specimen with a simple microstructure, i.e. single crystals [109, 66] or coarse-grained specimens with a columnar grain through the thickness [108, 113, 36, 87, 90, 50, 31, 112, 14, 72]. These multi-crystal specimens, usually in the sheet form, are referred to as 'oligocrystals' and have a small numbers of grains, typically 3-20 grains within the gage section. Oligocrystal specimens are used to compare and validate CP-FEM models with experiments, e.g. predictions of hardening behavior [31, 72], texture evolution [36, 50, 31, 112, 60, 61], inter- and intra-grain strain fields [113, 87, 90, 50, 47, 112, 14, 60, 61, 99], deformed specimen shapes [60, 61] and activated slips [46, 108, 113, 36]. However, most previous studies focus on FCC metals and many lack direct and quantitative comparisons, even with simplified microstructures.

In this report, we present multi-scale modeling and experimental techniques to better understand the plastic deformation in tantalum. This report is based on three recent publications on modeling and experimental studies of tantalum [69, 70, 71] as well as further results that were not included in these publications. The purpose of this report is to integrate and discuss detailed simulation and experimental procedures and results. This report is comprised of two main topics. In Chapters 2, 3 and 4 we develop temperature and strain rate dependent single crystal constitutive equations for tantalum based on the dislocation kink-pair theory and single crystal data from the literature [106]. The novel constitutive equations based on the motion of thermally activated screw dislocations are implemented into BCC CP-FEM model to simulate plastic deformation of single- and polycrystals. CP-FEM is then used to parameterize various conventional continuum-scale analytical models that provide convenient constitutive formulations for approximating the effects of temperature and strain rate on plastic deformation of BCC metals. In Chapter 5, we validate the CP-FEM model with experimental measurements using tantalum oligocrystals. In addition, we discuss the limitations of the current approach and investigate influences of other constitutive effects in model predictions.

2 Dislocation Kink-Pair Theory

The dislocation kink-pair theory describes the temperature and strain rate dependent flow stresses in BCC metals by relating the stress required to move a dislocation over the Peierls potential, τ_p [91, 93, 22, 9]. The theory is based on the assumption that the flow stress resolved onto the active slip system, τ, is composed of thermal and athermal contributions as follows:

$$\tau(T,\dot{\gamma}) = \tau^*(T,\dot{\gamma}) + \bar{\tau}. \tag{1}$$

Here τ^* is the thermal component of the flow stress that depends on temperature (T) and strain rate ($\dot{\gamma}$) while $\bar{\tau}$ represents the athermal stress that is independent of strain rate and weakly dependent on temperature through the shear modulus. $\bar{\tau}$ accounts for long-range interactions such as the effects of forest dislocations, impurities, solutes and grain boundaries, and can be determined from the resolved shear stress above a critical temperature, $T_c(\dot{\gamma})$, where the thermal part of the lattice friction is negligible. For tantalum, measured athermal contribution, $\bar{\tau}$, obtained from the single crystal experiments is 27 MPa [106].

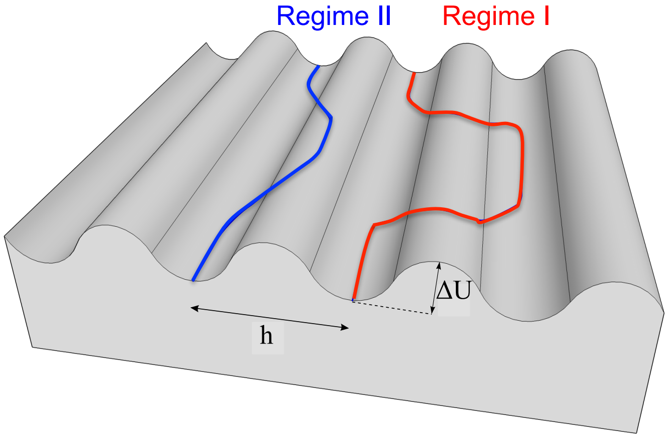

Figure 1. Illustration of Peierls barrier and dislocation kink-pair at two temperature regimes. One dislocation shows a bulge in the line (on the left), described by the line tension model in Regime II; and the second dislocation (right) has well formed kinks, described by the elastic interaction model in Regime I. The valleys and peaks are separated by the spacing h and the height of the Peierls potential is ΔU.

Following the work of Seeger et al. [91, 92, 93], there are three temperature regimes in the flow behavior of BCC metals. In the high temperature regime, above the critical temperature, $T_c(\dot{\gamma})$, the thermal dependence is similar to that of FCC metals. In this temperature regime, τ^* becomes negligible and often ignored. Below the critical temperature, $T_c(\dot{\gamma})$, BCC metals exhibit thermally activated flow that deviate from the behavior of FCC metals, and the mobility of screw dislocations is the main contribution to the high resistance to flow. Below $T_c(\dot{\gamma})$, there are two regimes that are divided by $\hat{T}(\dot{\gamma})$. In Regime I where $\hat{T}(\dot{\gamma}) < T < T_c(\dot{\gamma})$, the kinks are fully formed and well separated, and the energetics are controlled by the elastic repulsion between kinks. Thus, the kink-pair formation enthalpy, ΔH^*_{kp}, can be calculated using the Elastic Interaction (EI) model. Regime II ($T < \hat{T}(\dot{\gamma})$) is characterized by an activation barrier where the dislocation does not reach the adjacent Peierls valley. In this regime, kinks are not fully formed and can be described by the Line Tension (LT) model. Figure 1 illustrates the Peierls barrier and the transition states of the kink-pairs for Regime I and Regime II.

An Arrhenius expression relating the activation enthalpy, strain rate and temperature can be obtained by using a transition state theory as follows [91]:

$$\dot{\gamma} = \dot{\gamma}_0 \exp\left(-\frac{\Delta H^*_{kp}(\tau^*)}{k_\mathrm{B}T}\right) \tag{2}$$

where $\dot{\gamma}_0$ is a reference strain rate, ΔH^*_{kp} is the double kink activation enthalpy and k_B is the Boltzmann constant. $\dot{\gamma}_0$ depends weakly on temperature and, when compared directly to the exponential temperature dependence, can be approximated as a constant.

2.1 Elastic Interaction (EI) Model

In Regime I where $\hat{T}(\dot{\gamma}) < T < T_c(\dot{\gamma})$ is satisfied, the activation enthalpy associated with the repulsion of a fully-formed kink-pair, ΔH^*_{kp}, can be represented using the EI model as follows [91]:

$$\Delta H^*_{kp} = 2H_k - 2\sqrt{\frac{\mathcal{T} b h^3}{2}\tau^*}. \tag{3}$$

Here, H_k is the formation enthalpy of an isolated kink, h is the kink height, b is the Burger's vector and $\mathcal{T}$ is the pre-logarithmic dislocation line tension factor of a screw dislocation. Using Equations (2) and (3), a relationship between τ^*, temperature and strain rate in Regime I can be obtained:

$$\tau^*_I = \tau^{EI}_p \left(1 - \frac{k_\mathrm{B}T \ln(\dot{\gamma}_0/\dot{\gamma})}{2H_k}\right)^2 = \tau^{EI}_p \left(1 - \frac{T}{T_c(\dot{\gamma})}\right)^2 \tag{4}$$

where,

$$\tau^{EI}_p = \frac{2H_k^2}{\mathcal{T} b h^3} \quad \text{and} \quad T_c(\dot{\gamma}) = \frac{2H_k}{k_\mathrm{B}\ln(\dot{\gamma}_0/\dot{\gamma})}. \tag{5}$$

Note that the value of T_c in Equation (5) represents the temperature where the thermal part of the flow stress becomes zero for a given strain rate. $\dot{\gamma}_0$ is a material constant that is used in Arrhenius expression that relates the temperature and shear strain rate to the activation enthalpy in thermally activated deformation mechanism. The value of $\dot{\gamma}_0$ can be estimated from $\dot{\gamma}_0 = b\rho_m w d$, where ρ_m is the mobile dislocation density, w is the attempt frequency and d is the lattice spacing.

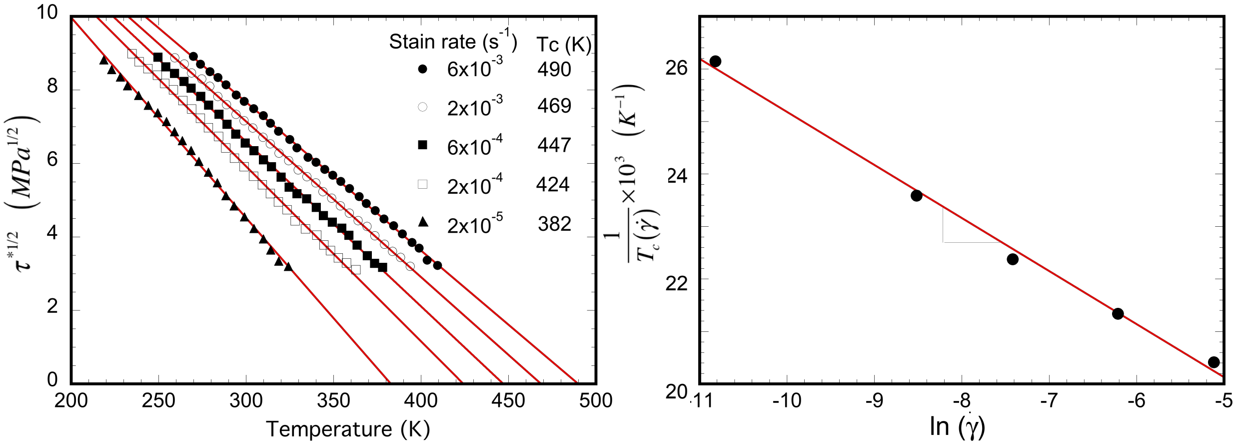

Figure 2. Plots of (a) $\tau^{*1/2}$ vs. temperature and (b) $1/T_c(\dot{\gamma})$ vs. $\ln(\dot{\gamma})$ used to find material constants of the EI model.

Equation (4) can be fit to single crystal experiments to determine material paraters for the EI model, e.g. $T_c(\dot{\gamma})$, τ_p^{EI}, $2H_k$, and $\dot{\gamma}_0$. For example, a linear fit to measured $\tau^{*1/2}$ and temperature can be used to obtain $T_c(\dot{\gamma})$ and τ_p^{EI} for each strain rate while $2H_k$ and $\dot{\gamma}_0$ can be obtained by the linear fit between $1/T_c(\dot{\gamma})$ and $\ln(\dot{\gamma})$ for Regime I. Figure 2 (a) and (b) show linear fits to tantalum single crystal experiments [106] to obtain material parameters in the EI model.

2.2 Line Tension (LT) Model

At low temperatures (Regime II), $\tau^{*1/2}$ is not linear in temperature and the LT model should be used to describe flow in this regime. The activation enthalpy of kink-pair formation, ΔH_{kp}^*, is determined using a simple dislocation line tension model that incorporates the shape of the Peierls potential in the formulation. Analytical expressions that relate the activation enthalpy, applied stress, temperature and strain rate can only be obtained under certain circumstances. Thus, a number of authors have introduced model potentials to facilitate solutions [91, 9, 45, 23, 40]. Notably, a sinusoidal potential has no analytical solution while those comprised of parabolas do [27]. Some common analytical representations of Peierls potentials are shown in Figure 3.

Following the previous work by Seeger et al. [91, 106, 92, 94], ΔH_{kp}^* using Eshelby Peierls

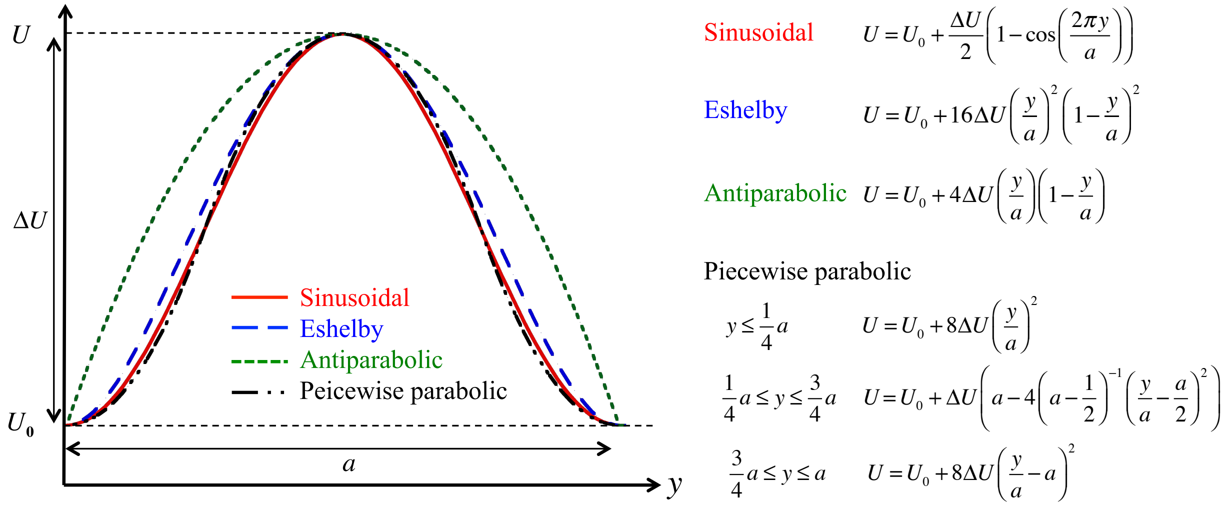

Figure 3. Different representations of Peierls potential: Sinusoidal, Eshelby, antiparabolic and piecewise parabolic funtions.

potential can be approximated as follows:

$$\Delta H^*_{kp} \approx 2H_k - hb\tau^*\sqrt{\frac{\mathcal{S}}{U''(h)}}\left(1 + \ln\frac{\tilde{\tau}}{\tau^*}\right), \tag{6}$$

where $\mathcal{S}$ is the line tension associated with a screw dislocation, $U(h)$ is the Peierls potential and $\tilde{\tau} = 2hU''(h)/b$. For the Eshelby potential, $\tilde{\tau} = 12\sqrt{3}\tau_p$, $U''(h) = \frac{6\sqrt{2}b\tau_p}{h}$ and $hb\sqrt{\frac{\mathcal{S}}{U''(h)}} = \frac{H_k}{\sqrt{3}\tau_p}$ are satisfied [40]. The activation energy for the Eshelby potential in Equation (6) can be alternatively written as follows [91]:

$$\Delta H^*_{kp} = 2H_k\left[1 - \frac{\tau^*}{2\sqrt{3}\tau_p}\left(1 - \ln\frac{\tau^*}{12\sqrt{3}\tau_p}\right) + \mathcal{O}(\tau^*)\right], \tag{7}$$

where $\mathcal{O}(\tau^*)$ is the higher order terms of the expansion. This form is useful in deriving a transition between Regime I and Regime II as well as illuminating when the use of this approximation to the Eshelby potential fails. If we assume ΔH^*_{kp} for EI model and LT model are equal at the transition temperature ($\hat{T}$) and ignore higher order terms in Equation (7), an implicit equation for τ^* is obtained [91]

$$2\sqrt{\frac{\mathcal{T}bh^3}{2}\tau^*} = \frac{2H_k\tau^*}{2\sqrt{3}\tau_p}\left(1 - \ln\frac{\tau^*}{12\sqrt{3}\tau_p}\right). \tag{8}$$

Using the flow stress, $\hat{\tau}$, obtained from single crystal experiments conducted at the transition temperature, Equation (8) provides τ_p. In addition, $2H_k$ can be obtained from fitting $k_{\mathrm{B}}T\ln(\dot{\gamma}_0/\dot{\gamma})$ versus $\tau^*(1+\ln(\tilde{\tau}/\tau^*)$ (Equation (6)) to measured single crystal data. Combining Equation (7) with Equation (2) and ignoring higher order terms, an implicit equation for τ^* is obtained [91]:

$$\frac{T}{T_c} = 1 - \frac{\tau^*}{2\sqrt{3}\tau_p}\left(1 - \ln\frac{\tau^*}{12\sqrt{3}\tau_p}\right). \tag{9}$$

This is the procedure essentially used in refs [91, 106, 20, 53, 52, 94] with minor differences. Note that above derivation for Eshelby potential [91] is valid for low values of τ^* where higher order terms in Equation (7) are ignored. At high stress and low temperature regime, ΔH^*_{kp} and τ^* using Eshelby potential can be approximated as follows [91, 21]:

$$\Delta H^*_{kp} = 2H_k\frac{5}{6}\left[\frac{2}{3}\left(1-\frac{\tau^*}{\tau_p}\right)\right]^{5/4} \quad \text{and} \quad \tau^* = \tau_p\left(1 - \frac{2}{3}\left(\frac{5}{6}\right)^{4/5}\left(\frac{T}{T_c(\dot{\gamma})}\right)^{4/5}\right). \tag{10}$$

An empirical LT model that approximate sinusoidal and two Eshelby models at low and high stress regimes (Equations (9) and (10)) can be represented as follows:

$$\Delta H^*_{kp} = 2H_k\left(1-\left(\frac{\tau^*}{\tau_p}\right)^{4/5}\right)^{5/4} \quad \text{and} \quad \tau^* = \tau_p\left(1-\left(\frac{T}{T_c(\dot{\gamma})}\right)^{4/5}\right)^{5/4}. \tag{11}$$

Alternatively, the LT model with antiparabolic representation of Peierls potential can be represented as follows [9, 23, 38]:

$$\Delta H^*_{kp} = 2H_k\left(1-\frac{\tau^*}{\tau_p}\right)^{2} \quad \text{and} \quad \tau^* = \tau_p\left(1-\left(\frac{T}{T_c(\dot{\gamma})}\right)^{1/2}\right). \tag{12}$$

LT models adopting antiparabolic or sinusoidal representations of the Peierls potentials, Equations (11) and (12), allow more simple and direct representation of the flow stress compared to Eshelby model. More general forms of activation enthalpy and τ^* to estimate temperature and strain rate effects are written as follows [64]:

$$\Delta H^*_{kp} = 2H_k\left(1-\left(\frac{\tau^*}{\tau_p}\right)^{p}\right)^{q} \quad \text{and} \quad \tau^* = \tau_p\left(1-\left(\frac{T}{T_c}\right)^{1/q}\right)^{1/p}. \tag{13}$$

Here, the values of p and q determine the shape of the energy barrier profile such that $0 \leq p < 1$ and $1 \leq q < 2$ are satisfied. Thus, p = 4/5 and q = 5/4 for sinusoidal and p = 1 and q = 2 for antiparabolic LT models, respectively.

In order to understand the difference in calculated τ^* with the choice of Peierls potentials, $\Delta H_{kp}^*/2H_k$ versus τ^*/τ_p is plotted using various representations of Peierls potentials as shown in Figure 4. Here, Eshelby and Eshelby (high τ_p) represent τ^* approximations using Equations (9) and (10), respectively. For the piecewise parabolic function, the potential is parabolic with upward concave parabola at $y \leq a/4$ and $3a/4 \leq y \leq a$, and a downward concave parabola at $a/4 \leq y \leq 3a/4$. As ΔH_{kp}^* approaches zero, the Eshelby potential (Equation (9)) does not converge to the expected value of $\tau^* = \tau_p$, but instead to approximately $\tau^* = 0.82\tau_p$. This deviation at high stress regime for Seeger's approximation using the Eshelby potential is due to the truncation of the higher order terms in Equation (7).

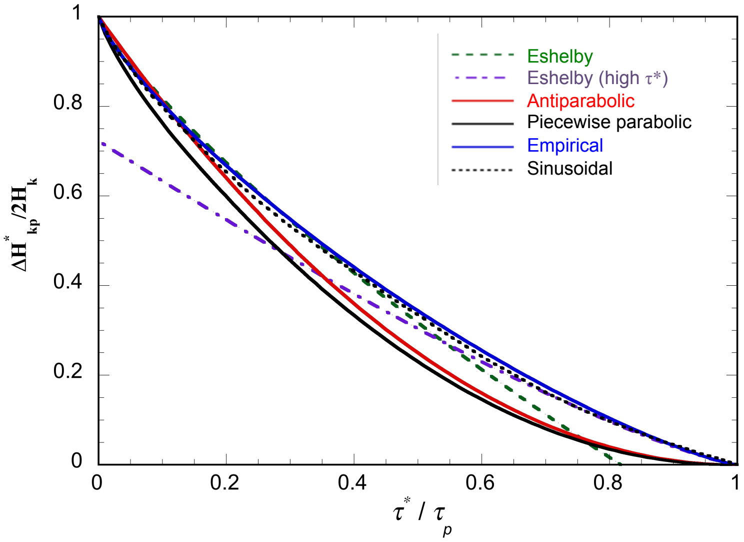

Figure 4. A plot of $\Delta H_{kp}^*/2H_k$ versus τ^*/τ_p using different Peierls potentials. Empirical model approximates sinusoidal and two Eshelby models.

As shown in Figure 3, the shape of the piecewise parabolic function is very close to that of the sinusoidal function which was shown to agree well with DFT results of Peierls potential for various BCC refractory metals including molybdenum, tantalum, tungsten and niobium [105]. Despite the obvious differences between the antiparabolic and piecewise parabolic representations (Figure 3), the functional forms of $\Delta H_{kp}^*/2H_k$ versus τ^*/τ_p using two representations are quite similar at high τ^* where the LT model is applicable. On the other hand, the empirical formulation in Equation (11) agrees very well to the sinusoidal representation of the Peierls potential and agrees with Eshelby approximations at two stress regimes at low and high stress regimes, respectively. Thus, antiparabolic and empirical representation of the temperature and strain rate dependent flow stress also provides a simple model for accurately representing the flow behavior of BCC metals.

2.3 Comparison with Experimental Data

The EI and LT models described in the previous sections are parameterized to tantalum single crystal stress-strain data from the literature [106]. In this experimental work, Werner [106] used ultrapure tantalum single crystals having residual resistance ratio (RRR) $\cong$ 14000 and interstitial concentrations (C + N + O) less than 2 ppm to measure temperature and strain rate dependent flow stresses between T = 80 K and 450 K and $\dot{\varepsilon}$ = 2 $\times 10^{-5}$ s^{-1} and 6 $\times 10^{-3}$ s^{-1}. τ^* values for single crystal tantalum were obtained from the Ackermann-Mughrabi technique which uses pre-deformed specimens that are cyclic-saturated to produce very stable dislocation cell structure and thus, minimize the variance in the observed response [2, 106].

Figures 5 shows the measured [106] and fitted τ^* using the EI and LT models with the antiparabolic Peierls potential for tantalum single crystals as a function of temperature for various strain rates. It is shown that the EI and LT models accurately reproduce the temperature and strain rate dependent flow stresses of tantalum single crystals in two temperature regimes. Note that the transition stresses between two regimes, $\hat{\tau}$, are approximately 93 MPa. Table 1 lists best-fit material constants for the EI model and LT model using the antiparabolic Peierls potential.

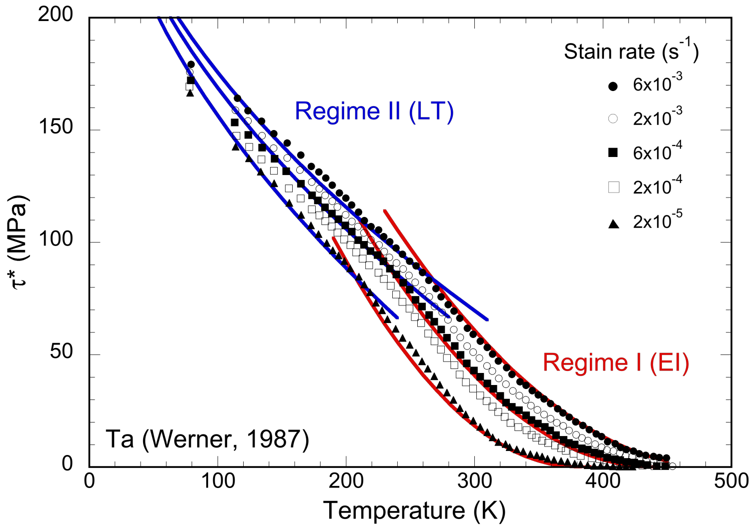

Figure 5. A plot of measured and fitted τ^* at different temperatures and strain rates.

In order to see the effects of different Peierls potential shapes in LT model, Figures 6 compares the best-fit τ^* in Regime II using the antiparabolic, Eshelby and the empirical formulation. The best-fit values of τ_p are 286 MPa, 267 MPa and 320 MPa for Eshelby, empirical and antiparabolic LT models, respectively. Standard deviations between measured and fitted τ^* using three models are 3.3 MPa, 4.1 MPa and 3.6 MPa, respectively. Although τ^* obtained from three LT models exhibit relatively good agreement with measured data in all temperature ranges for tantalum, it

Table 1. Best-fit material parameters used for the EI and LT models.

Parameter	Value	Parameter	Value
τ_p^{EI}	406 MPa	$\dot{\gamma}_0$	2.99×10^6 s^{-1}
τ_p^{LT}	320 MPa	$2H_k^{EI}$	0.85 eV
$\hat{\tau}$	93 MPa		

is shown that high τ^* of tungsten at low temperatures is most accurately reproduced by the antiparabolic LT model [69].

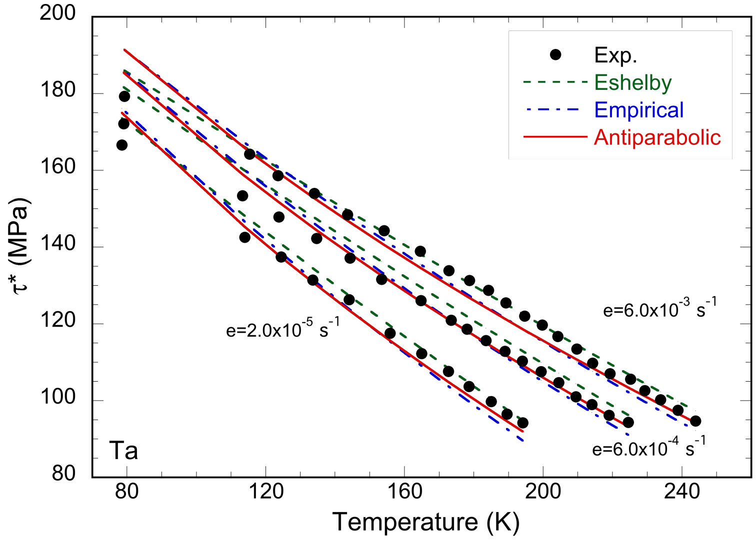

Figure 6. Line tension model predictions using the Eshelby, antiparabolic and empirical representation of the Peierls potential. All three models exhibit relatively good agreement with measured temperature dependence.

2.4 Kink-Height and Preferred Slip System

The planes on which dislocation kinks nucleate, i.e. the slip planes, can be related to the height of the dislocation kinks. Since the kink height, h, is directly related to the formation energy of the kinks, it is hypothetically possible to extract the kink heights from experimentally determined kink formation energies and compare with theoretical kink heights for different slip systems. For example, the theoretical kink height for $\{110\}$, $\{112\}$ and $\{123\}$ slip planes are $\sqrt{2/3}a_0$, $\sqrt{2}a_0$, and $\sqrt{8/3}a_0$, respectively, where a_0 is the lattice parameter. Therefore, kink heights to lattice parameter ratios for three slip systems are $h_{\{110\}}/a_0 = 0.82$, $h_{\{112\}}/a_0 = 1.41$ and $h_{\{123\}}/a_0 = 1.63$. Previous kink-pair studies consistently suggest that tantalum, molybdenum, tungsten and niobium prefer $\{112\}$ slip [106, 53, 52, 20, 94], with the exception of tungsten at low temperature [20].

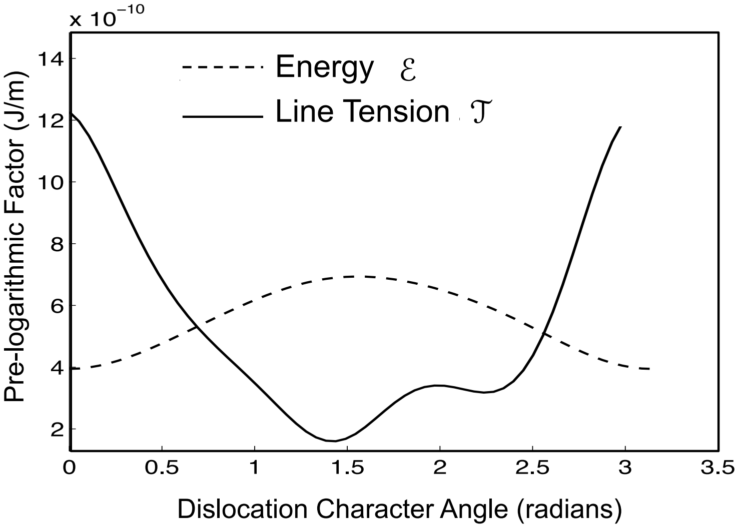

Figure 7. Calculated pre-logarithmic factor of the dislocation line tension and energy for tantalum.

The line energy, E, of a dislocation is related to the pre-logarithmic energy factor $\mathcal{E}$ as $E = \mathcal{E}\ln(R/r_o)$ where R and r_o are outer and inner cutoff radii respectively. The dislocation line tension, $\mathcal{S}$, is related to the dislocation line energy as $\mathcal{S} = E + \frac{\mathrm{d}^2E}{\mathrm{d}\theta^2}$, where θ is the angle between the Burger's vector and the dislocation line direction. The pre-logarithmic line tension factor, $\mathcal{T}$, is then related to the pre-logarithmic line energy as $\mathcal{T} = \mathcal{E} + \frac{\mathrm{d}^2\mathcal{E}}{\mathrm{d}\theta^2}$. Since the pre-logarithmic line tension factor is used throughout kink-pair theory, it must be computed accurately using anisotropic elasticity. To do this, we use the integral formalism of anisotropic elasticity theory as described by Bacon *et al.* [13] with the line tension evaluated using the integrals developed by Barnett *et al.* [15]. The computed pre-logarithmic energy and line tensions values are listed in Table 2 for screw and edge dislocations, while the values computed over all angles are shown in Figure 7.

Kink heights can be obtained independently for Regime I and II using EI and LT models, as follows:

$$h_{(EI)} = \sqrt[3]{\frac{2H_k^2}{\mathcal{T}b\tau_0^{EI}}} \qquad h_{(LT)} = \sqrt[3]{\frac{6H_k^2}{\mathcal{T}b\tau_p}} \tag{14}$$

Table 2. Calculated energy factor $\mathcal{E}$ and pre-logarithmic line tension factors $\mathcal{T}$ for tantalum and calculated kink height. Subscripts s and e represent screw and edge dislocations, respectively.

Parameters	Value	Parameters	Value
$\mathcal{E}_e$	6.94×10^{-10} N	a_0	3.31 Å
$\mathcal{E}_s$	3.94×10^{-10} N	b	2.87 Å
$\mathcal{T}_e$	1.84×10^{-10} N	$h_{(EI)}$	4.01 Å
$\mathcal{T}_s$	1.23×10^{-9} N	$h_{(EI)}/a_0$	1.21
$\mathcal{T}$ used [106]	1.18×10^{-9} N	$h_{(LT)}$	3.96 Å
		$h_{(LT)}/a_0$	1.20

Table 2 lists calculated h and h/a_0 using revised pre-logarithmic line tension factors for molybdenum, tantalum and tungsten. For Regime II, the kink height is calculated using the Eshelby potential to compare with previous analyses [106, 53, 52, 20, 94]. As listed in Table 2, h/a_0 obtained from the fit to the single crystal experiments for both EI and LT models are close to 1.20. These h/a_0 values are in between theoretical values of h/a_0 for $\{110\}$ and $\{112\}$ slip, 0.82 and 1.41, respectively. Therefore, these revised kink height calculations suggest that it is difficult to conclusively support preferred slip system for tantalum. It should be also noted that the kink height calculations depend on τ_0 and τ_p that are obtained by the extrapolations from the fit. Thus, h is sensitive to the fit and any experimental scatter may have a large influence on h calculations. In addition, this procedure assumes temperature and stress independent Peierls potential which may also affect the fit and thus the predicted kink height. Therefore, kink-pair theory may not be the optimum method to obtain accurate kink height estimates for determining the favorable slip planes in BCC structured metals.

3 BCC Crystal Plasticity Finite Element Model

Crystal plasticity is based on the assumption that the plastic deformation is due to dislocation movement through the crystal lattice or slip. The development of constitutive equations that describe elastic-plastic deformation of crystals began with Taylor's analysis of polycrystal deformation [98] and later, comprehensive formulations have appeared [48, 12, 86]. Based on well-established crystal plasticity formulations and adopting single crystal constitutive equations based on dislocation kink-pair theory, BCC crystal plasticity finite element (CP-FE) model for tantalum is developed. Constitutive equations are implemented into finite element code (JAS-3D) developed at Sandia National Laboratories [17, 103, 73]. In this section, some important concepts and frame work of the crystal plasticity model used in this work are presented. The model is then used to simulate grain-scale deformation of single and polycrystalline tantalum.

3.1 Crystal Plasticity Formulations

The kinematics of crystal plasticity model used in this work follows multiplicative decomposition of the deformation gradient [65, 88, 48, 86, 37, 73]. The total deformation gradient **F** is decomposed into elastic and plastic parts.

$$\mathbf{F} = \mathbf{F_e} \cdot \mathbf{F_p} \tag{15}$$

Here, $\mathbf{F_e}$ and $\mathbf{F_p}$ are the elastic and plastic part of the total deformation gradient, respectively. $\mathbf{F_e}$ accounts for elastic distortion of the lattice while $\mathbf{F_p}$ defines the slip by the dislocation motion in the unrotated configuration as shown in Figure 8. Note that Plastic deformation by $\mathbf{F_p}$ is an isochoric and stress-free intermediate configuration in which the crystallographic lattice is unaltered and unrotated with respect to the reference configuration. This stress-free intermediate configuration can be obtained by unloading the deformed body from the current configuration. It is assumed that this part results solely from continuous plastic shearing (dislocation motion) on well-defined slip systems and dislocations pass completely through the material element of interest. Here, other deformation mechanisms such as dislocation cross-slip, climb and twinning are not considered.

In Figure 8, $\mathbf{s}_0^\alpha$ and $\mathbf{n}_0^\alpha$ are the initial unit vectors in the slip direction and the slip plane normal direction on α-th slip system, respectively. These two vectors define the α-th slip system uniquely in each crystal. The slip direction vectors are regarded as embedded in the lattice and slip plane normal is always perpendicular to the slip direction. As the crystal deforms, lattice is stretched and rotated according to $\mathbf{F_e}$. Therefore, rotated slip direction ($\mathbf{s}^\alpha$) and slip plane normal ($\mathbf{n}^\alpha$) of the slip system α is given by,

$$\mathbf{s}^\alpha = \mathbf{F_e} \cdot \mathbf{s}_0^\alpha \qquad \text{and} \qquad \mathbf{n}^\alpha = \mathbf{n}_0^\alpha \cdot \mathbf{F_e}^{-1}. \tag{16}$$

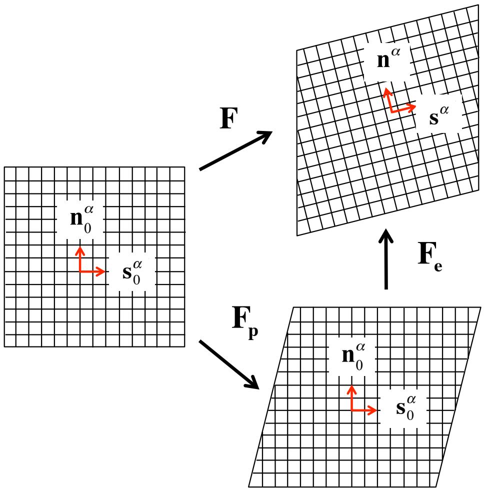

Figure 8. A schematics of multiplicative decomposition of the deformation gradient.

The plastic deformation gradient, $\mathbf{F_p}$, can be calculated by the crystal slip as follows [10]:

$$\mathbf{F_p} = \mathbf{I} + \gamma^\alpha \mathbf{s}_0^\alpha \otimes \mathbf{n}_0^\alpha. \tag{17}$$

Here, γ^α is the amount of slip in α-th slip system. The velocity gradient, $\mathbf{L}$ in the current configuration is written as:

$$\mathbf{L} = \mathbf{L_e} + \mathbf{L_p} = \dot{\mathbf{F}} \cdot \mathbf{F}^{-1}, \tag{18}$$

where, $\mathbf{L_e}$ and $\mathbf{L_p}$ are elastic and plastic parts of the velocity gradient, respectively, and can be represented as follows:

$$\mathbf{L_e} = \dot{\mathbf{F}}_\mathbf{e} \cdot \mathbf{F_e}^{-1} \qquad \text{and} \qquad \mathbf{L_p} = \mathbf{F_e} \cdot \dot{\mathbf{F}}_\mathbf{p} \cdot \mathbf{F_p}^{-1} \cdot \mathbf{F_e}^{-1}. \tag{19}$$

Assuming plastic deformation is caused by the dislocation slip, the plastic part of the velocity gradient can be written as [86]:

$$\mathbf{L_p} = \sum_\alpha \dot{\gamma}^\alpha \mathbf{s}^\alpha \otimes \mathbf{n}^\alpha. \tag{20}$$

The slip rate on α-th slip system, $\dot{\gamma}^\alpha$, is represented as a power-law function of resolved shear stress, τ^α, and slip resistance, g^α, as follows [54]:

$$\dot{\gamma}^\alpha = \dot{\gamma}_0^\alpha \left(\frac{\tau^\alpha}{g^\alpha}\right)^{1/m} \tag{21}$$

Here, $\dot{\gamma}_0^\alpha$ is the reference shear rate and m is the rate sensitivity factor. For tantalum, $\dot{\gamma}_0^\alpha$ = 0.001 s^{-1} and m = 0.012 are adopted [19, 57] and assumed to be identical for all slip systems. In this work, 24 $\{110\}\langle 110\rangle$, as listed in Table 3, are used as supported by many atomistic simulations and digital image correlation (DIC) experiments [104, 26].

Table 3. The twenty-four $\{110\}$ slip systems.

α	Slip System	α	Slip System	α	Slip System	α	Slip System
1	$(01\bar{1})[111]$	7	$(0\bar{1}\bar{1})[\bar{1}\bar{1}1]$	13	$(01\bar{1})[\bar{1}\bar{1}\bar{1}]$	19	$(0\bar{1}\bar{1})[11\bar{1}]$
2	$(\bar{1}01)[111]$	8	$(101)[\bar{1}\bar{1}1]$	14	$(\bar{1}01)[\bar{1}\bar{1}\bar{1}]$	20	$(101)[11\bar{1}]$
3	$(1\bar{1}0)[111]$	9	$(\bar{1}10)[\bar{1}\bar{1}1]$	15	$(1\bar{1}0)[\bar{1}\bar{1}\bar{1}]$	21	$(\bar{1}10)[11\bar{1}]$
4	$(\bar{1}0\bar{1})[\bar{1}11]$	10	$(10\bar{1})[1\bar{1}1]$	16	$(\bar{1}0\bar{1})[1\bar{1}\bar{1}]$	22	$(10\bar{1})[\bar{1}1\bar{1}]$
5	$(0\bar{1}1)[\bar{1}11]$	11	$(011)[1\bar{1}1]$	17	$(0\bar{1}1)[1\bar{1}\bar{1}]$	23	$(011)[\bar{1}1\bar{1}]$
6	$(110)[\bar{1}11]$	12	$(\bar{1}\bar{1}0)[1\bar{1}1]$	18	$(110)[1\bar{1}\bar{1}]$	24	$(\bar{1}\bar{1}0)[\bar{1}1\bar{1}]$

The second Piola-Kirchhoff stress, **S**, in the intermediate configuration can be represented as follows:

$$\mathbf{S} = \mathbf{C} : \mathbf{E} = \det\left(\mathbf{F_e}\right)\mathbf{F_e}^{-1}\mathbf{T}\mathbf{F_e}^{-T}, \tag{22}$$

where, **E** is the Lagrangian strain tensor, **T** is the Cauchy stress, and **C** is the fourth order elastic constant matrix. The Lagrangian strain tensor, **E**, can be expressed using deformation gradients as follows:

$$\mathbf{E} = \frac{1}{2}\left(\mathbf{F_e}^{-T}\mathbf{F_e} - \mathbf{I}\right). \tag{23}$$

The resolved shear stress of slip system α in Equation (21) is approximately,

$$\tau^\alpha = \mathbf{S} : \mathbf{P}_0^\alpha = \mathbf{S} : \left(\mathbf{s}_0^\alpha \otimes \mathbf{n}_0^\alpha\right). \tag{24}$$

For BCC metals, the slip resistance on α-th slip system, g^α, can be decomposed into thermal and athermal parts as follows [69]:

$$g^\alpha = \min\left(\tau_{EI}^*, \tau_{LT}^*\right) + \tau_{\text{obs}}^\alpha. \tag{25}$$

Here, the first term represents temperature and strain rate dependent lattice resistance based on the kink-pair theory as described in the previous section [91, 93, 9, 22]. At high temperature and low stress regime (Regime I), EI model is used to represent τ^*:

$$\tau_{EI}^* = \tau_0^{EI}\left(1 - \frac{T}{T_c}\right)^2 = \tau_0^{EI}\left(1 - \frac{k_\mathrm{B}T\ln(\dot{\gamma}_0/\dot{\gamma})}{2H_k}\right)^2. \tag{26}$$

Here, T_c is the critical temperature, H_k is the enthalpy of an isolated kink and $\dot{\gamma}_0$ is the reference strain rate. For low temperature and high stress regime (Regime II), LT model using the antiparabolic representation of Peierls potential [9] is used as follows:

$$\tau^*_{LT} = \tau^{LT}_0 \left(1 - \left(\frac{T}{T_c}\right)^{1/2}\right) = \tau^{LT}_0 \left(1 - \sqrt{\frac{k_B T \ln(\dot{\gamma}_0/\dot{\gamma})}{2H_k}}\right). \tag{27}$$

Note that in most CP-FE models for FCC metals, a thermal part of the flow stress is ignored. On the other hand, $\tau^{\alpha}_{\text{obs}}$ represents obstacle stress and regarded as an athermal part of the resolved shear stress for slip system α. Note that non-Schmid effect is ignored in this work which was shown to have negligible effect at room temperature deformation [73]. In comparing Equation (25) to Equation (1), g^{α} corresponds to $\tau(T,\dot{\gamma})$, $\min(\tau^*_{\text{EI}}, \tau^*_{\text{LT}})$ to $\tau^*(T,\dot{\gamma})$, and $\tau^{\alpha}_{\text{obs}}$ to $\bar{\tau}$.

The obstacle strength,$\tau^{\alpha}_{\text{obs}}$, is formulated with forest dislocation densities as follows [97]:

$$\tau^{\alpha}_{\text{obs}} = A\mu \text{b} \sqrt{\sum_{\beta=1}^{\text{NS}} \rho^{\beta}}. \tag{28}$$

Here, A is a material constant usually in the range of 0.3 - 0.6, μ is the shear modulus, b is the Burger's vector, NS is the total number of slip systems, and ρ^{β} is the dislocation density in slip system β. It is assumed that initial dislocation densities are identical for all 24 slip systems and are obtained from Equation (28) and $\tau^{\alpha}_{\text{obs}}(t=0)=\bar{\tau}$. Then, the total dislocation density for α-th slip system is obtained by using a standard phenomenological equation as follows [62]:

$$\dot{\rho}^{\alpha} = \left(\kappa_1 \sqrt{\sum_{\beta=1}^{\text{NS}} \rho^{\beta}} - \kappa_2 \rho^{\alpha}\right) \cdot |\dot{\gamma}^{\alpha}|, \tag{29}$$

where, κ_1 and κ_2 are material parameters representing generation and annihilation of dislocations, respectively. Thus, $\tau^{\alpha}_{\text{obs}}$ evolves as the slip of dislocations on the slip system occurs and governs the strain hardening of the model. The elastic constants and material constants used in the simulations are listed in Table 4.

Table 4. Elastic constants and material constants used in crystal plasticity model of tantalum.

C_{11} (GPa)	C_{12} (GPa)	C_{44} (GPa)	b (Å)	$\tau_{\text{obs},0}$ (MPa)
267	161	82.5	2.87	27

3.2 Yield Stress Predictions

The kink-pair-derived flow rules for tantalum described in the previous section were implemented into a crystal plasticity code to simulate uniaxial tension of single and polycrystals. Single crystal CP-FEM simulations were conducted using a single hexahedral finite element with a crystal orientation of $[\bar{1}49]$ along the tensile axis; this particular orientation was chosen because it is the softest orientation, with the highest degree of resolved shear on the slip plane. Thus, the resolved shear stresses from existing experimental data are converted to a uniaxial tensile stress by adding in $\tau_{\text{obs},0}$ and using a Schmid factor of 0.5. These temperature and strain rate dependent tensile stresses for tantalum single crystals were compared with predicted yield stresses from CP-FEM simulations using a 0.2% offset criterion. Note that flow stresses obtained from Ackermann-Muchrabi cyclic tests are compared with yield stress from tensile simulations. Given that the rate of hardening in tantalum is very low, flow stress obtained from the Ackermann-Mughrabi technique can be assumed to be comparable to the yield stress. In addition, temperature and strain rate dependent τ^* would have no significant effect on pre-deformation. As shown in Figures 9, the flow rules calibrated to single crystal data in the two temperature regimes provide accurate CP-FEM predictions of temperature and strain rate dependent yield stresses of single crystal tantalum.

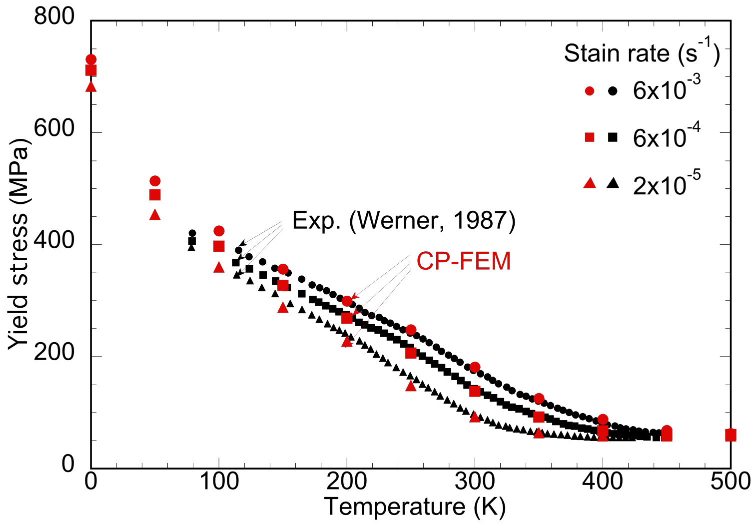

Figure 9. Measured and predicted yield stresses versus temperature and strain rates for tantalum single crystals in $[\bar{1}49]$ direction.

To simulate polycrystal deformation, we used a three-dimensional cubic specimen having 125 grains (5×5×5) with 64 elements per grain (total of 8,000 elements) as shown in Figure 10 (a). Each grain was assigned a random initial crystal orientation from a uniform distribution. Uniaxial tension was simulated with (i) varying temperature at constant strain rates of 10^{-4} s^{-1}, and (ii) varying strain rate at room temperature. Predicted yield stresses are compared with various experimental data from both the literature and our own tensile tests.

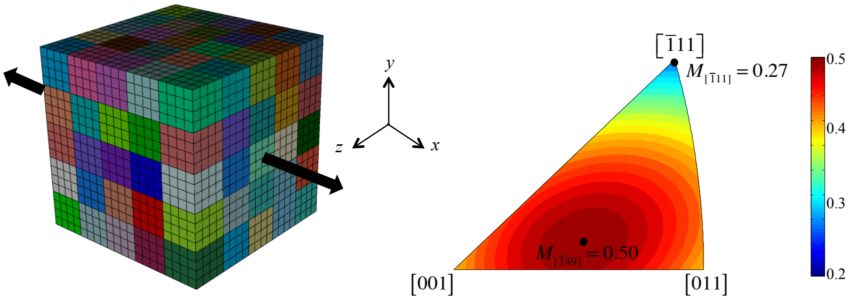

(a) (b)

Figure 10. (a) Schematic of an idealized 3D grain assembly used for polycrystal simulations, and (b) the maximum Schmid factors within the stereographic triangle. Single crystals oriented for $[\bar{1}11]$ and $[\bar{1}49]$ loading directions have the maximum and minimum values of 0.50 and 0.27.

Figures 11 (a) and (b) show measured and predicted yield stresses versus temperature and strain rate, respectively, in polycrystalline tantalum. CP-FEM simulations of yield stresses (red circles) exhibit the same trends observed in the experimental data from various sources [51, 85, 100, 3, 29]. This agreement suggests that the thermal part of the flow stresses in polycrystals is accurately predicted using the CP-FEM simulation informed by the single crystal data. Figure 10 (b) shows the maximum Schmid factors of slip system within the stereographic triangle for $\{110\}\langle 111\rangle$. Single crystals oriented for $[\bar{1}11]$ and $[\bar{1}49]$ tension have minimum and maximum Schmid factors of 0.27 and 0.50, respectively. Thus, $[\bar{1}11]$ and $[\bar{1}49]$ single crystals provide yield stresses of the hardest and softest orientations, respectively. Therefore, these cases (dashed lines in Figures 11 (a) and (b)) provide an estimate of the upper and lower limits of strength in polycrystals (neglecting other microstructural effects such as hardening due to grain boundaries and non-Schmid effects). As shown in Figures 11 (a) and (b), various experimental data from the literature fall within this simple depiction of upper and lower limits. This is especially encouraging since the model calibration was performed using data from only single crystal tests.

3.3 Strain Hardening Predictions

In order to assess the strain hardening predictions of the model, hardening parameters were fit to reproduce the measured stress-strain response of polycrystal tantalum at 298 K and $\dot{\varepsilon} = 10^{-4}\ s^{-1}$ [51]. A three-dimensional polycrystal mesh described in the previous section was used to parameterize the hardening parameters. The model was then used to predict the stress-strain responses at 78 K and 144 K. For all three temperatures, the best-fit hardening parameters obtained from 298 K simulations, k_1 = $1.4\times10^6\ m^{-1}$ and k_2 = 20. Although we assume that τ_{obs} is independent of temperature and strain rate in the model, $\tau_{\text{obs},0}$ is parameterized for each temperature to accurately reproduce the yield and to fit the hardening behavior. $\tau_{\text{obs},0}$ = 66 MPa, 27 MPa, and 19 MPa were used for 78 K, 144 K and 298 K simulations, respectively.

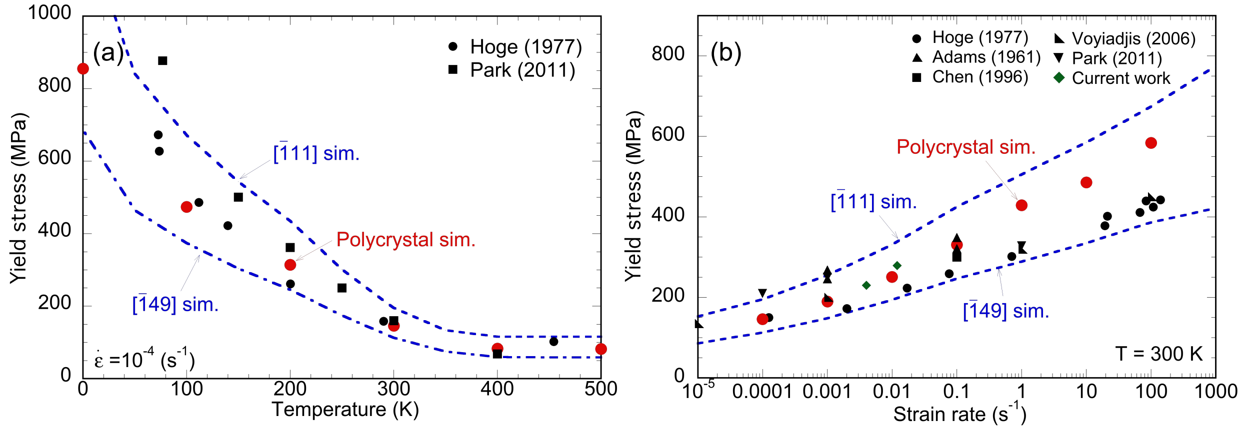

Figure 11. A plot of measured and predicted yield stresses of polycrystals at (a) different temperatures and (b) different strain rates at 300 K. Dashed lines represent yield stress predictions using $[\bar{1}11]$ and $[\bar{1}49]$ single crystals.

As shown in Figure 12 (a), the model accurately reproduces stress-strain response at 298 K and predicts hardening behavior at two other temperatures up to the strain before necking or strain softening occurs. It should be noted, however, that the current model does not capture the upper yield point observed at small strains that attributed to interaction between dislocations and impurities such as hard precipitations. On the other hand, the model using dislocation density based hardening rule predicts lower strain hardening rate for lower temperature and larger strains as shown in Figure 12 (b).

Note that the current model does not directly consider possible temperature dependent mechanisms that affect strain hardening (e.g. temperature dependent dislocation evolution or mean free path of mobile dislocations). The predicted temperature dependent strain hardening in Figure 12 (b) is attributed to different yield stress arising from τ_{obs} which in turn changes initial dislocation density for different temperatures. Thus, temperature dependent strain hardening would not be observed in conventional slip-based or isotropic hardening formulations.

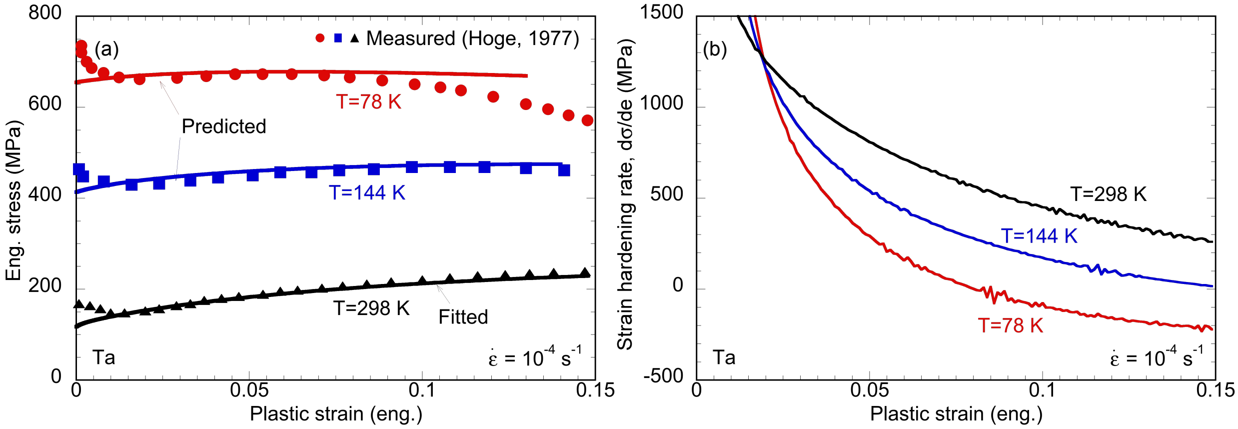

Figure 12. A plot of (a) measured [51] and predicted stress-strain curves and (b) strain hardening rates of tantalum polycrystal at different temperatures.

4 Polycrystalline Models Incorporating Effects of Temperature and Strain Rate

Several continuum-scale constitutive models exist for describing the flow behavior of polycrystalline BCC metals at high temperatures and strain rates [56, 5, 55, 110, 41, 59]. These models are generally fit to experimental data of polycrystals to obtain material constants and reproduce measured flow behavior. Using an analogous approach, we fit some of these constitutive models to CP-FEM polycrystal simulation results in an attempt not only to investigate how well these models reproduce temperature and strain rate dependent yield behavior of polycrystalline tantalum, but also to construct a simple polycrystal constitutive model that can be efficiently used in other applications, e.g. large scale metal forming analysis or shock applications, without requiring extremely large and expensive CP-FEM calculations.

4.1 Continuum Scale Polycrystalline Models

Three most widely used constitutive models that incorporate the effects of temperature and strain rate are Johnson-Cook (JC) model [56, 55], Zerilli-Armstrong (ZA) model [110] and Mechanical Threshold Stress (MTS) model [41]. The JC, ZA and MTS models have the following forms to represent the flow stress:

$$\sigma^{JC} = (A + B \cdot \varepsilon_p^n)(1 + C \cdot \ln\dot{\varepsilon})(1 - T^{*m}), \tag{30}$$

$$\sigma^{ZA} = C_0 + C_1 \exp(-C_3 T + C_4 T \ln\dot{\varepsilon}) + C_5 \varepsilon_p^n, \tag{31}$$

$$\sigma^{MTS} = \sigma_0 + \sigma_1 \varepsilon_p^n + \hat{\sigma}\left(1 - \left(-\frac{k_B}{G_0} T \ln\frac{\dot{\varepsilon}}{\dot{\varepsilon}_0}\right)^{1/q}\right)^{1/p}, \tag{32}$$

where, ε_p is the plastic strain, $\dot{\varepsilon}$ is the strain rate, T^* is the homologous temperature ($T^* = (T - T_{room})/(T_m - T_{room})$), G_0 is the activation energy per atom to overcome obstacles, $\dot{\varepsilon}_0$ is the reference strain rate, and the p and q in Equation (32) represent parameters that determine the shape of the energy barrier profile such that $0 \leq p < 1$ and $1 \leq q \leq 2$ [64]. Note that these models adopt power-law Ludwik hardening [74]. If we assume that the yield stress is obtained at $\varepsilon_p = 0$, Equations (30)-(32) can be rewritten as follows:

$$\sigma_y^{JC} = A(1 + C \cdot \ln\dot{\varepsilon})(1 - T^{*m}), \tag{33}$$

$$\sigma_y^{ZA} = C_0 + C_1 \exp(-C_3 T + C_4 T \ln \dot{\varepsilon}), \tag{34}$$

$$\sigma_y^{MTS} = \sigma_0 + \hat{\sigma} \left(1 - \left(-\frac{k_\mathrm{B}}{G_0} T \ln \frac{\dot{\varepsilon}}{\dot{\varepsilon}_0} \right)^{1/q} \right)^{1/p} . \tag{35}$$

Note that $\dot{\varepsilon}$ in Equations (33) - (35) represent the macroscopic strain rates of polycrystalline while $\dot{\gamma}$ used in the EI and LT models denote resolved shear strain rates of single crystals. The EI and LT models adopting antiparabolic Peierls potential have the same form as that of the MTS model with $p = 0.5$, $q = 1$ and $p = 1$, $q = 2$ in two different temperature/ stress regimes, respectively. In contrast, most MTS models are generally fit with arbitrary chosen values of p and q for all temperature and strain rates [81, 30, 85, 82, 83, 80]. Despite the similar functional forms of the EI/ LT models with the MTS model, the EI and LT models are derived from physics of dislocation motion via kink-pair nucleation while the MTS model is a generic phenomenological model of thermally activated flow.

4.2 Comparisons with CP-FEM Data

The JC, ZA, and MTS models in Equations (33) - (35) require three, four and six material constants to represent the yield stress, respectively. In order to parameterize these material constants, yield stresses obtained from polycrystal CP-FEM simulations (red circles in Figures 11) are fit to each constitutive equation using a least-squares fitting procedure. For the JC model, we use $T^* = T/T_{melt}$ to capture yield stresses below the room temperature and avoid T^* becoming a negative value. For the ZA and MTS models, C_0 and σ_0 representing an athermal part of the yield stress are determined from the yield stresses at high temperature/ low strain rate, 82 MPa. Previous studies adopting the MTS model usually assume constant values of p and q in the range of $0 < p \leq 1$ and $1 \leq q \leq 2$ [64] while $\dot{\varepsilon}_0$ is estimated from $\varepsilon_0 = b\rho_m w_0 d$ where ρ_m is the mobile dislocation density, w_0 is the attempt frequency and d is the lattice spacing. Table 5 lists material parameters used in MTS models in previous studies [82, 81, 80, 83, 30, 85]. Note that in most cases, $\hat{\sigma}$ is the only fitting parameter that is obtained from experimental data. In this work, all six parameters in the MTS model, p, q, $\dot{\varepsilon}_0$, σ_0, $\hat{\sigma}$ and G_0, are determined directly from the fit to the polycrystal CP-FEM simulations. The MTS model in Equation (35) is only applicable when $\dot{\varepsilon} \leq \dot{\varepsilon}_0$ and $-\frac{k_\mathrm{B}}{G_0} T \ln \frac{\dot{\varepsilon}}{\dot{\varepsilon}_0} \leq 1$ are satisfied. However, at very high temperature/ low strain rate regime, it is numerically possible to have $-\frac{k_\mathrm{B}}{G_0} T \ln \frac{\dot{\varepsilon}}{\dot{\varepsilon}_0}$ larger than 1. In such case, we assume that there is no thermal/ strain rate dependent stress contributions and use σ_0 to represent the yield stress.

Figures 13 (a) and (b) compare yield stresses fit to CP-FEM simulations using three constitutive formulations. It is shown that yield stresses are accurately reproduced by the MTS and ZA models, while the JC model produced a relatively poor-quality fit, consistent with the earlier work on tantalum and tantalum-tungsten alloys [29]. Note that the JC model has a linear relationship between the yield stress and the logarithm of strain rate, and thus is not easily able to reproduce

Table 5. Material parameters used in MTS models in previous studies [82, 81, 80, 83, 30, 85].

References	$\hat{\sigma}$ (MPa)	G_0 (eV)	ε_0 (s^{-1})	p	q
Nemat-Nasser [82]	1100	1	1×10^8	2/3	2
Nemat-Nasser [83]	1140	1	5×10^8	2/3	2
Park [85]	1100	1	5×10^8	0.3	1

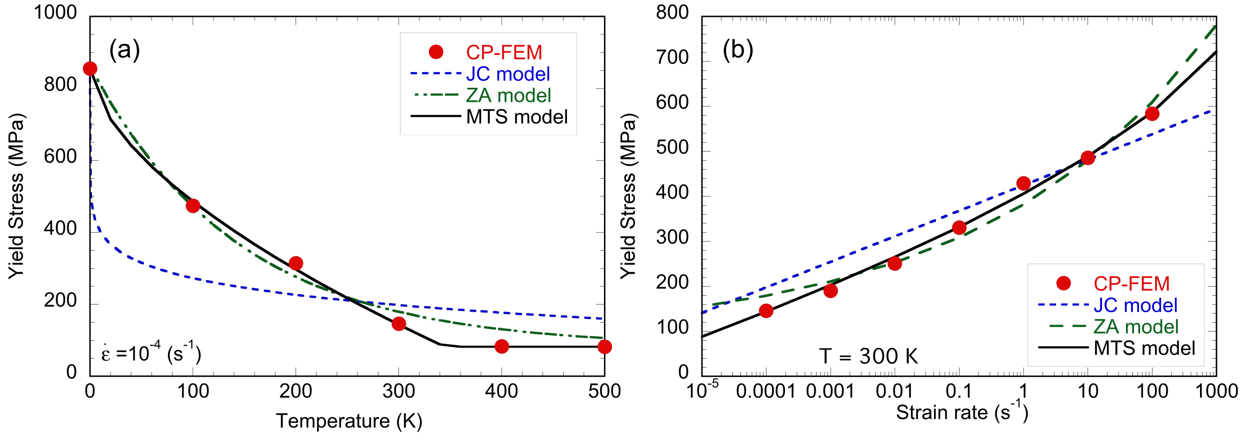

Figure 13. A plot of yield stresses fit to CP-FEM simulations using the JC, ZA and MTS model for (a) different temperature and (b) different strain rates at 300 K.

temperature and strain rate dependent flow stresses simultaneously. Note that the predicted yield stresses saturate at high temperature/ low strain rate regimes for the MTS model where $-\frac{k_B}{G_0}T\ln\frac{\dot{\varepsilon}}{\dot{\varepsilon}_0}$ becomes larger than 1 and the yield stress is equal to $\hat{\sigma}$, consistent with CP-FEM predictions. Table 6 lists the standard deviations of yield stresses between CP-FEM simulations and three continuum models. It is clearly shown that the temperature and strain rate dependent yield behavior is most accurately reproduced using the MTS model. Table 7 lists best-fit material parameters for the three models. For the MTS model, the best-fit p and q obey $0 < p \leq 1$ and $1 \leq q \leq 2$ [64] and the best-fit G_0 is 1.96 eV, the same order of magnitude as $2H_k$ obtained from the kink-pair analysis. Also, C_1 and $\hat{\sigma}$ representing the thermal part of the flow stress at 0 K in the ZA and MTS models show good agreement.

In comparing the kink-pair model and the MTS model, $\dot{\gamma}_0$ corresponds to $\dot{\varepsilon}_0$, $2H_k$ to G_0 and τ_p to $\hat{\sigma}$. For BCC polycrystals, it can be estimated that $G_0 = 2H_k$, $\dot{\varepsilon}_0 = M\dot{\gamma}_0$ and $\hat{\sigma} = M\tau_p$ where M is the average Taylor factor [98]. Thus, the MTS model can be fit to CP-FEM polycrystal predictions with material parameterss informed from the kink-pair analysis. Values in parentheses in Tables 6 and 7 represent values obtained using $G_0 = 2H_k$ and $\varepsilon_0 = M\dot{\gamma}_0$, obtained from from the kink-pair analyses while $\hat{\sigma}$, p and q values are fit to CP-FEM predictions.

Table 6. Standard deviations of yield stresses between CP-FEM predictions and continuum fits using the JC, ZA and MTS models (unit: MPa).Values in parentheses in MTS model represent fitting results using $G_0 = 2H_k$ and $\dot{\varepsilon}_0 = M\dot{\gamma}_0$, obtained from the kink-pair analysis.

Models	Std. dev (MPa)
JC model	78.3
ZA model	28.2
MTS model	10.2(48.0)

Table 7. Best-fit constants used for the JC, ZA and MTS models. Values in parentheses in MTS model represent fitting results using $G_0 = 2H_k$ and $\dot{\varepsilon}_0 = M\dot{\gamma}_0$, obtained from the kink-pair analysis.

Models	Parameters	Values
JC	A (MPa)	1848
	C	0.058
	m	0.109
ZA	C_1 (MPa)	779
	C_3 (K^{-1})	3.18×10^{-3}
	C_4 ($K^{-1}\cdot s^{-1}$)	4.08×10^{-4}
MTS	G_0 (eV)	1.96 (0.85)
	$\dot{\varepsilon}_0$ (s^{-1})	2.8×10^3 (9.1×10^{10})
	$\hat{\sigma}$ (MPa)	772 (767)
	p	1.00 (0.69)
	q	1.67 (1.00)

It is shown in Table 6 that the MTS model using material parameters informed from the kink-pair model reproduces yield behaviors relatively well, but not as accurate as the MTS model with all parameters fit to the data. Using material parameters informed from kink-pair theory still provides better predictions than the JC model; furthermore, this approach has the advantage of being more physically based. As listed in Table 7, the best-fit $\hat{\sigma}$ obtained from two MTS fits agrees well while the other material parameters, G_0, $\dot{\varepsilon}_0$, p and q, do not show obvious correlations. This implies that the continuum-scale model is able to reproduce the observed macroscopic polycrystalline behavior but it is unable to predict the single crystal, and hence dislocation-scale, properties. Thus, the multi-scale formulation provided here allows one to propagate lower-scale information up to the continuum, but demonstrates that larger length scale models cannot provide insight into the physics at lower length scales, which is perhaps not surprising.

4.3 Simulation of Taylor Impact Test

In this section, the constitutive model described in the previous section is used in high-rate solid dynamics simulations of a common benchmark application: Taylor cylinder impact tests of a projectile specimen impinging on a hard target [95]. This method is often used to validate solid dynamics simulation codes and models; and it provides a simple, convenient, and robust approach for subjecting a single specimen to a wide range of strain rates across its length.

The simulation was conducted using ALEGRA, Lagrangian-Eulerian multi-physics code developed at Sandia National Laboratories. Figure 14 shows a schematic of a Taylor impact test. The simulated projectile is a tantalum cylinder with dimensions of 38.1 mm in length and 7.62 mm in diameter, and impinges on a hard surface of 4340 steel at a velocity of 175 m/s. Simulations were conducted at standard atmospheric conditions described by a temperature of 298 K and pressure of 1 bar.

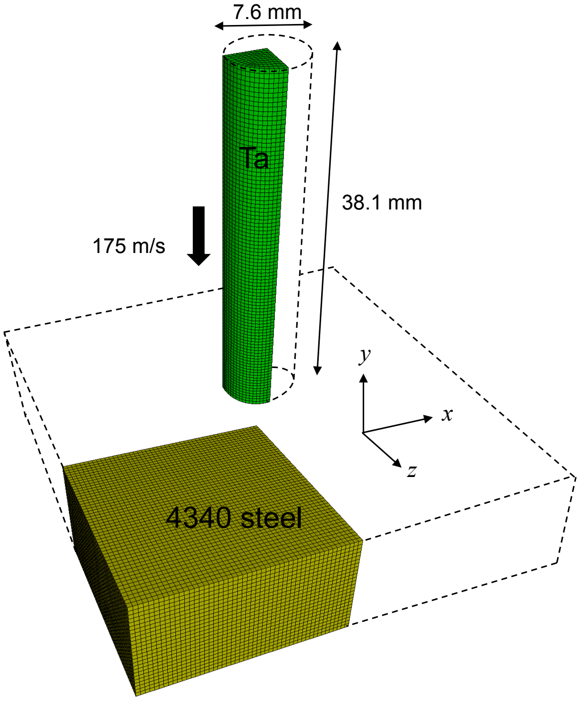

Figure 14. A schematic of a Taylor cylinder impact test. Tantalum cylinder impinges on 4340 steel block at a velocity of 175 m/s.

The three-dimensional Lagrangian simulations were conducted with 9,120 hexahedral finite elements in the tantalum projectile, and a target surface consisting of a block of 4340 steel described by 62,500 hexahedral finite elements. A three-dimensional quarter-symmetry condition was used. The MESQUITE remeshing algorithm was imposed at every time step in the ALEGRA simulations to avoid numerical artifacts associated with ill-conditioned finite elements evolving during deformation. The contact between the projectile and target was assumed to be frictionless.

In ALEGRA, each material requires models for equation of state (EOS) and elastic-plastic deformation (yield model). For tantalum projectile and steel plate, Mie-Grüneisen EOS model and Sesame tabular EOS data were used, respectively [58]. For the yield model in tantalum, LT model in dislocation kink-pair model suitable for high rate regime in Equation (12) is adopted. The strain hardening rate is represented by an empirical law using tanh function as follows [44]:

$$\frac{\partial \sigma}{\partial \varepsilon_p} = \theta_0 \left(1 - \frac{\tanh\left(\alpha\sigma/\sigma_s\right)}{\tanh(\alpha)}\right). \tag{36}$$

Here, ε_p is the equivalent plastic strain, θ_0 and α are the material parameters and σ_s represent temperature and strain rate dependent saturation stress that can be represented as follows [62]:

$$\sigma_s = \sigma_s^0 \left(\frac{\dot{\gamma}}{\dot{\gamma}_0^s}\right)^{\frac{k_B T}{\mu b^3 A}}. \tag{37}$$

Here, A, α and $\dot{\gamma}_0^s$ are the material constants.

For 4340 steel, Zerilli-Armstrong yield model having the following form was used [110].

$$\sigma_Z = C_1 + C_2 \exp\left(-C_3 T + C_4 T \ln \dot{\varepsilon}_p\right) + C_5 \varepsilon_p^N. \tag{38}$$

where C_1 - C_5 and N are the material parameters. Table 8 lists material parameters used in yield models for tantalum and 4340 steel.

Figure 15 (a) compares measured [75] and simulated tantalum projectile after the impact. Taylor impact experiment was conducted under the same condition as the simulation. The simulated image was captured after the projectile reflected off the steel plate such that the centerpoint of the bottom of the (deformed) specimen reached its initial position of approximately 0.1 mm above the target surface. It is shown that the simulated specimen shape shows relatively good agreement with experimental data.

The profiles of the projectile's shapes after impact are shown in Figure 15 (b), which contains *x*-*y* coordinates along the outer surface from the ALEGRA simulation and previously published experiments on tantalum Taylor impact tests [75]. The model predictions agree well with the experiments. The total lengths of the deformed projectile was 28.4 mm from the simulation and 27.8 mm from the experiment, deviating approximately 2%. Deviations from the simulations may attribute to lack of incorporating the texture, plastic anisotropy and accurate friction between the surface and the projectile. Furthermore, consideration of deformation twinning observed at high strain rate regimes [77, 28] may be required for more accurate prediction.

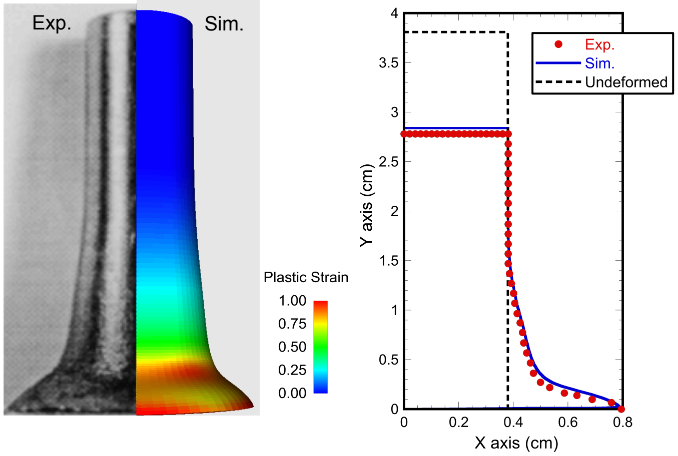

(a)
(b)

Figure 15. (a) Specimen shapes and equivalent plastic strain maps predicted by ALEGRA simulations of impact of a three-dimensional, quarter-symmetric tantalum specimen into a 4340 steel plate and (b) Projectile shape profiles (not to scale) predicted by all four ALEGRA simulations, with results reported from earlier Taylor cylinder impact experiments [75] (using the measurements from the minor axis).

Table 8. Material parameters used in ALEGRA yield model for tantalum and 4340 steel.

Materials	Parameters	Values
Tantalum	σ_s^0	575 GPa
	$\dot{\gamma}_0^s$	10^7 s^{-1}
	θ_0	2 GPa
	b	2.86 Å
	α	2.75
	A	1.6
4340 steel	C_1	89.8 MPa
	C_2	2.07 GPa
	C_3	17.4 K^{-1}
	C_4	0.56 K^{-1}
	C_5	1.03 GPa
	N	0.531

5 Validation of Crystal Plasticity Model with Experiments

In order to validate the proposed BCC CP-FEM model, plastic deformations of coarse-grained tantalum specimens were simulated and compared with experimental measurements of intragranular strain and crystal rotation fields. To mitigate the effects of unknown subsurface microstructure, tantalum tensile specimens with millimeter-sized grains provided nearly constant microstructure through the thickness of the tensile bar. Experimental validation was performed using (1) electron backscatter diffraction (EBSD) to map intragranular rotation, (2) high-resolution digital image correlation (HR-DIC) to map the surface strain field, and (3) surface profilometry to map the out-of-plane topographic distortion. Furthermore, measured surface strain fields were projected onto the finite element mesh to compare measured and simulated data on a point-wise basis.

5.1 Experimental Procedures

Flat tensile specimens were machined from a 1 mm thick rolled sheet of 99.9 % pure tantalum (Goodfellow Corporation), using electro-discharge machining (EDM). The gage section had a slight hourglass radius of curvature of 51 mm with nominal specimen dimensions shown in Figure 16. Heat treating specimens at 2000°C for 10 hours and 10^{-6} Torr in a vacuum furnace created specimens with millimeter-sized grains in pseudo-two-dimensional grain structures [26]. Specimens were then polished to a surface finish suitable for EBSD measurements [18]. A region of interest was defined on each specimen, measuring approximately 5.3 mm × 1.5 mm (specimen width), using scribe marks near the region boundaries; these fiducial markers were used for spatially aligning the multiple data sets (e.g. EBSD and DIC data).

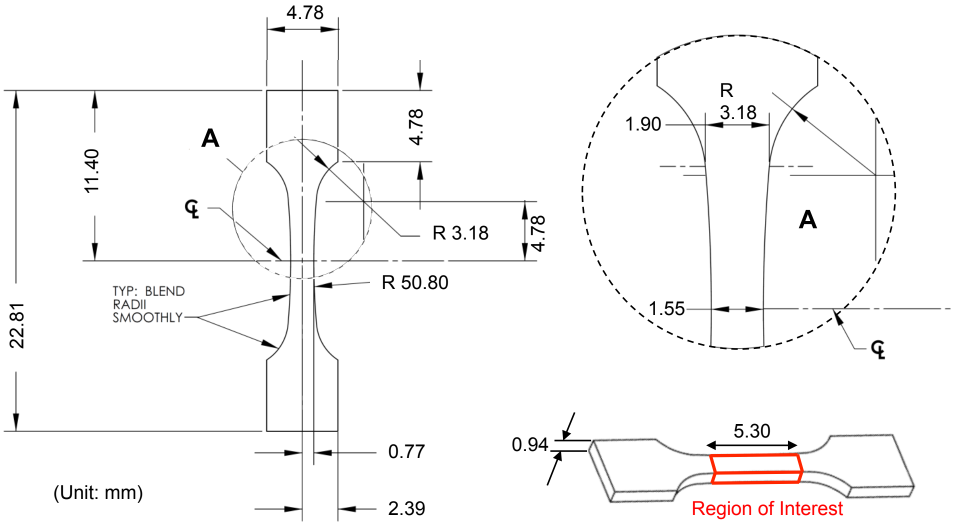

Figure 16. Nominal dimensions of the tantalum tensile specimens used in this work (unit:mm).

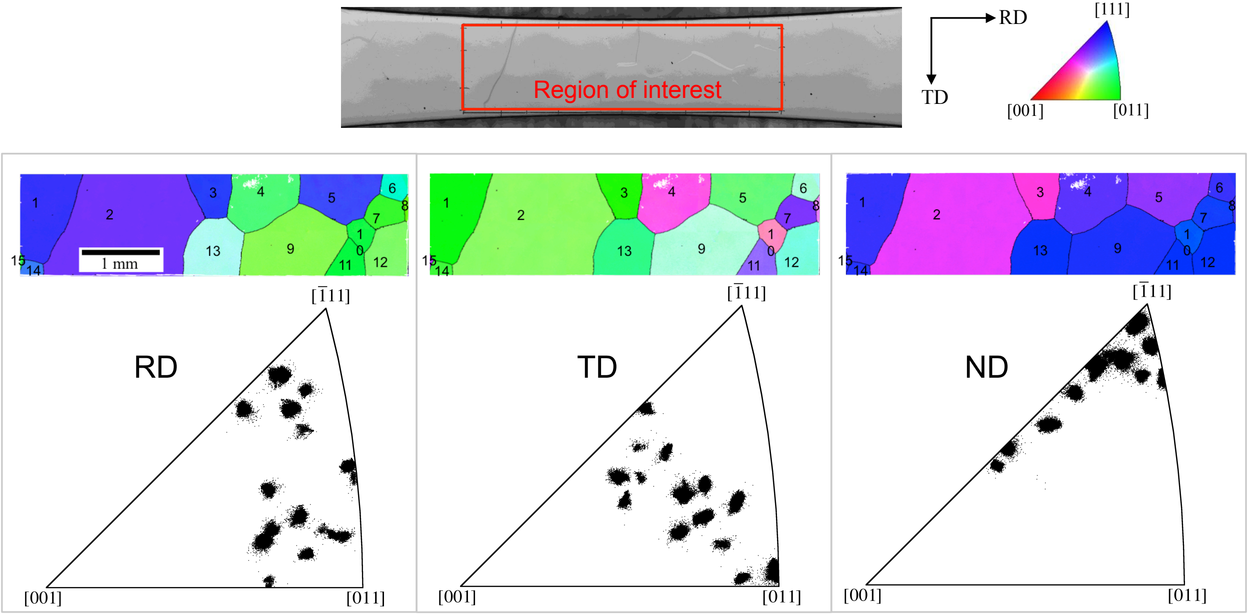

Figure 17. A plot of the initial crystal orientations of tantalum oligocrystal spencimen 1 within the region of interest obtained from the EBSD measurements. Lower figures show initial crystal orientations in inverse pole figures for RD, TD and ND.

The initial crystal orientations within the region of interest of each specimen were measured using Channel 5 software (Oxford Instruments) inside a Zeiss Supra 55VP field emission scanning electron microscope (SEM). Figures 17 - 19 show the initial crystal orientations with respect to RD, TD and ND of three tantalum oligocrystal specimens. Multiple EBSD scans were stitched together to cover the whole region of interest. Grain boundaries were defined as a 5° misorientation across the 5 μm (specimen 1) or 4 μm (specimens 2 and 3) EBSD step sizes. Totals of 15, 17 and 12 grains were identified within the regions of interest for specimens 1, 2 and 3, respectively. The average initial grain orientations in Bunge Euler angles relative to the globally defined axis are listed in Table 9. It was observed that all three specimens had no significant initial texture, i.e. initial grain orientations were spread out in the inverse pole figure.

To confirm the two dimensional nature of the microstructure in the gage section of the samples, Figure 20 shows the grain boundaries on the front and back sides of the specimens identified with EBSD measurements and etching. The dashed line in Figure 20 (b) represents a presumed grain boundary that was not revealed by etching. Although the grains were not perfectly columnar, most of the grain boundaries appeared to be within a few degrees of perpendicularity of the surface. In the associated crystal plasticity models, the grains were assumed to be perfectly columnar with subsurface crystal orientations identical to the corresponding surface measurements on an element-wise basis.

Tensile tests were conducted in a custom-built *in situ* load frame, Figure 21 (a), inside a Zeiss

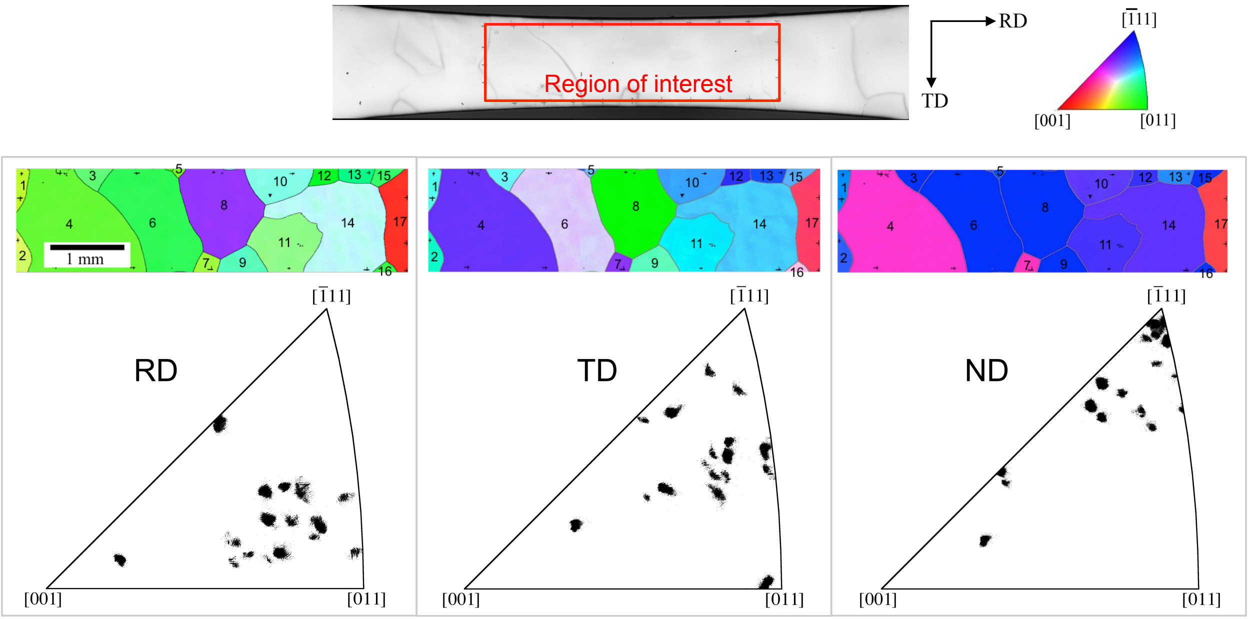

Figure 18. A plot of the initial crystal orientations of tantalum oligocrystal spencimen 2 within the region of interest obtained from the EBSD measurements. Lower figures show initial crystal orientations in inverse pole figures for RD, TD and ND.

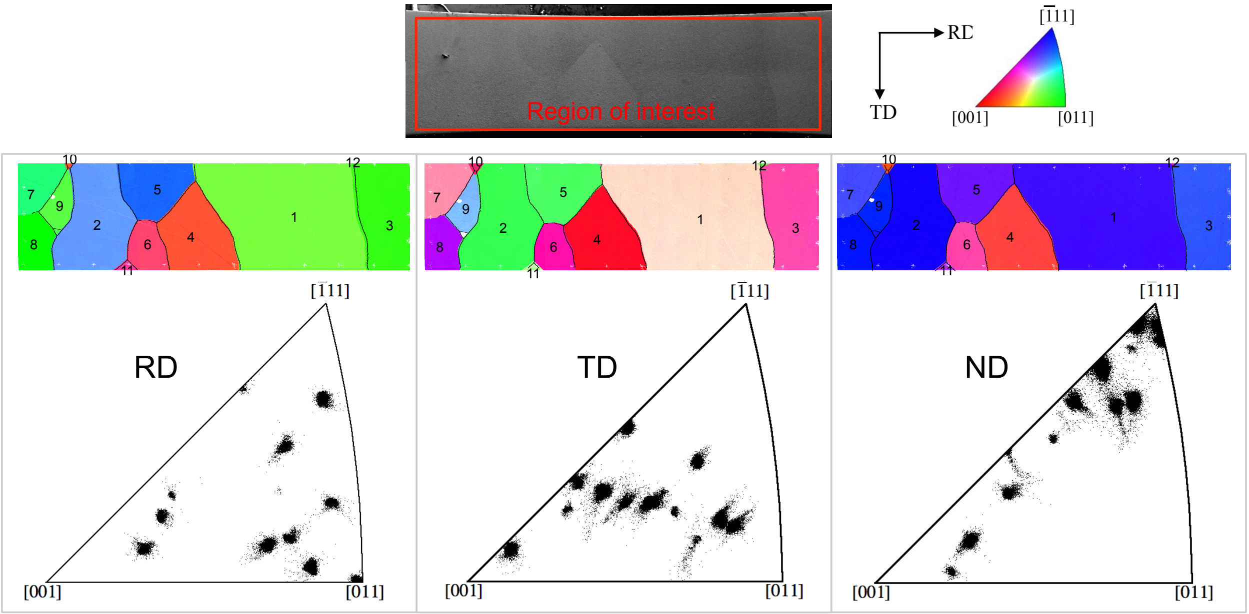

Figure 19. A plot of the initial crystal orientations of tantalum oligocrystal spencimen 3 within the region of interest obtained from the EBSD measurements. Lower figures show initial crystal orientations in inverse pole figures for RD, TD and ND.

Table 9. The initial crystal orientations of three tantalum oligocrystal specimens (Bunge Euler angles in degrees).

Specimen 1

Grain	ϕ_1	Φ	ϕ_2	Grain	ϕ_1	Φ	ϕ_2	Grain	ϕ_1	Φ	ϕ_2
1	136.7	45.0	86.8	6	135.9	45.0	71.9	11	135.9	52.8	66.2
2	135.8	28.6	74.4	7	142.8	48.6	54.6	12	140.0	51.6	43.6
3	132.4	25.9	87.5	8	132.6	43.8	129.1	13	136.3	51.8	17.2
4	132.5	40.6	65.9	9	131.3	47.8	135.0	14	132.9	47.3	82.3
5	131.1	35.2	106.5	10	124.6	50.7	74.1	15	136.9	45.9	62.3

Specimen 2

Grain	ϕ_1	Φ	ϕ_2	Grain	ϕ_1	Φ	ϕ_2	Grain	ϕ_1	Φ	ϕ_2
1	148.9	49.2	38.3	7	138.8	24.0	12.4	13	149.5	44.8	162.9
2	145.0	44.7	9.9	8	134.1	52.9	30.6	14	131.3	39.9	21.4
3	136.7	52.0	12.4	9	136.5	53.8	73.9	15	136.7	51.0	168.1
4	134.4	24.9	168.4	10	142.6	40.2	158.0	16	140.9	50.1	125.6
5	125.9	50.7	136.2	11	137.2	43.0	13.8	17	115.4	16.9	164.5
6	130.5	52.7	72.4	12	140.5	44.3	173.4				

Specimen 3

Grain	ϕ_1	Φ	ϕ_2	Grain	ϕ_1	Φ	ϕ_2	Grain	ϕ_1	Φ	ϕ_2
1	130.1	44.4	46.5	5	76.6	38.7	47.7	9	46.7	52.4	49.6
2	99.6	51.3	45.1	6	46.3	23.9	56.3	10	22.6	11.6	82.0
3	61.1	44.8	35.2	7	73.2	42.8	36.2	11	23.7	33.4	51.0
4	72.1	15.4	23.7	8	119.0	53.0	47.5	12	79.7	27.2	42.3

Supra 55VP field emission SEM. The tensile stage was specifically designed and built at Sandia National Laboratories to be used for *in situ* EBSD experiments [16, 25]. The load frame uses a linear variable differential transformer (LVDT) to measure displacement, and a custom-built, strain-gage-based transducer to measure applied load. The tensile tests were performed in displacement control in a stepwise fashion with $\dot{\varepsilon} = 10^{-4}$ s^{-1} up to the final strain levels of 6.8 % and 19.2 % for specimens 1 and 2, and $\dot{\varepsilon} = 10^{-3}$ s^{-1} up to the 10.0 % final strain for specimen 3, respectively. Figure 21 (b) shows the stress-strain response of three tantalum oligocrystals. Note that for specimen 1, EBSD and DIC data was collected at four applied strain levels, ε_{app} = 0, 0.8, 4.2 and 6.8 %. For specimen 2, EBSD data was collected at the initial, $\varepsilon_{app} = 0\%$ and final strain level, $\varepsilon_{app} = 19.2\%$, while the DIC images were captured at $\varepsilon_{app} = 4.0, 7.5$ and 11.0%. For specimen 3, both EBSD and DIC data was collected at five strain levels, ε_{app} = 0, 2, 4, 6, 8 and 10 %. Figures 22 (a) -(c) show the surface images of initial and deformed specimens.

To obtain the local strain fields throughout the region of interest, a recently developed HR-DIC technique was employed [24, 26]. After the initial EBSD scan, specimens were speckled with 300 nm copper powder. DIC results were obtained using Vic2d software (Correlated Solutions, Inc.). The first specimen was loaded while imaging it with an optical microscope at an image scale of 460 nm/pixel so that each image measures 640 by 478 μm. A mosaic array of 48 overlapping images (12 × 4) were stitched together to cover the region of interest, effectively resulting in a 41 megapixel image with 3.8 million DIC correlation points. The stitching of multiple images to

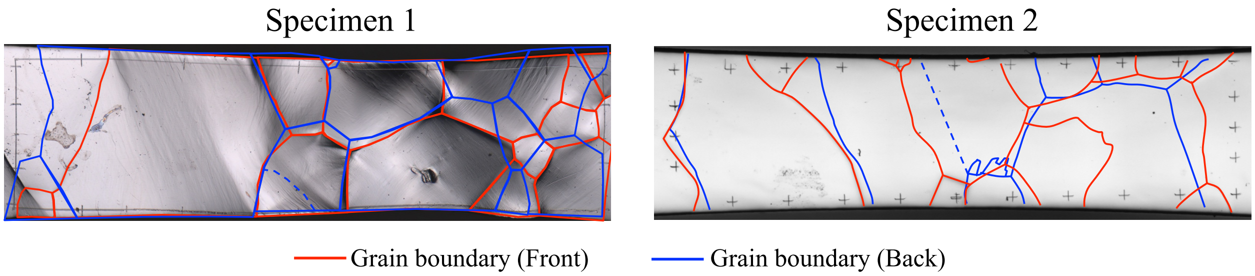

Figure 20. A plot of grain boundaries identified on front and back sides of tantalum oligocrystal specimens. Backside grain boundaries were determined by EBSD for specimen 1 and by etching for specimen 2. The dashed line on specimen 2 indicates the likely location of a backside grain boundary. The indentation mark in the center of a grain in (a) was due to an experimental mishap: the tip of a forcep damaged this spot on the polished specimen surface.

form a higher fidelity map differentiates high resolution DIC from traditional single-image DIC. The subset size and spacing for DIC measurements was 9.7 × 9.7 μm (21 × 21 pix) and 1.4 μm (3 pix), respectively. Crystal orientation measurements by EBSD were obscured when the copper speckles were on the specimen surface. To obtain both HR-DIC and EBSD measurements at each strain increment, the speckle pattern was repeatedly removed and reapplied to specimen 1. Consequently, only incremental strain measurements were available for specimen 1 (i.e. the strain accumulated during each loading step, not the total strain).

Loading of the second specimen took place inside the scanning electron microscope at roughly twice the magnification of the first specimen resulting in an image scale of 247 nm/pixel. The physical size of each image measured 759 by 570 μm. An array of 48 overlapping images (12 × 4) were used to cover the region of interest, effectively resulting in a 144 megapixel image with 15.1 million DIC correlation points. The subset size and spacing for DIC measurements was 20 × 20 μm (81 × 81 pix) and 0.74 μm (3 pix), respectively. For oligocrystal specimen 3, strain field results were obtained by stitching DIC results from 12 image locations (2 × 6) at each strain level. The image scale for these measurements was 439 nm/pix with individual images having a resolution of 3,072 × 2,304. DIC results were obtained with a subset size of 36× 36 μm (81 × 81 pix), a step size of 8 pixels (3.5 μm), and a strain window of 5 ×5 data points.

For surface strain field analysis, agrangian strain fields, ε_{xx}, ε_{yy}, and ε_{xy}, suitable for a large deformation, were used. Lagrangian finite strain tensor is defined as follows:

$$\varepsilon_{ij} = \frac{1}{2}\left(u_{i,j} + u_{j,i} + u_{k,i}u_{k,i}\right), \tag{39}$$

where u is the displacement field. After loading the first specimen, the topography of the front surface was measured using a a Wyco NT1100 optical profiling system with a 50× objective lens.

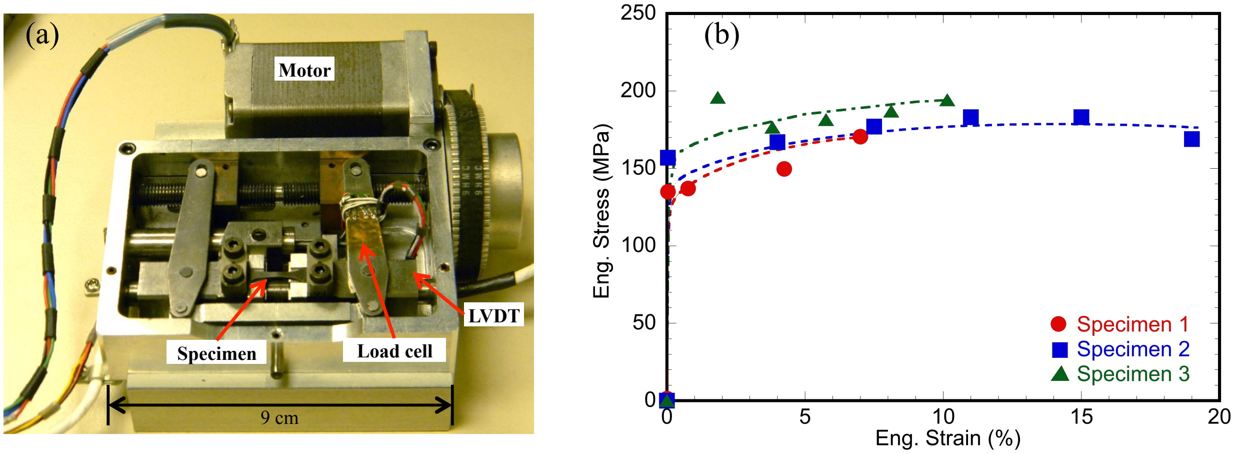

Figure 21. (a) An *in situ* tensile stage allowed loading to be performed inside a scanning electron microscope or an optical microscope. (b) Stress-strain data of three tantalum oligocrystal specimens. Dashed lines represent fitted stress-strain curves using the CP-FEM model.

The specimens were laid flat with negligible amounts of residual bending and torsion. The out-of-plane displacements w, on the front surface were spatially differentiated to calculate the displacement gradients $\partial w/\partial x$ and $\partial w/\partial y$ using the observation that the specimen surface was flat before loading (i.e. $z_{deformed} = w$). As will be shown in the results section, the measured deformation gradients provide a useful metric for 3D model validation (more useful than the raw out-of-plane surface profile, w). Measurements of the out-of-plane strains ε_{xz}, ε_{yz}, and ε_{zz} were unavailable since the complementary quantities $\partial u/\partial z$, $\partial v/\partial z$, and $\partial w/\partial z$ (where u and v represent the in-plane displacements in the x and y directions, respectively) could not be measured.

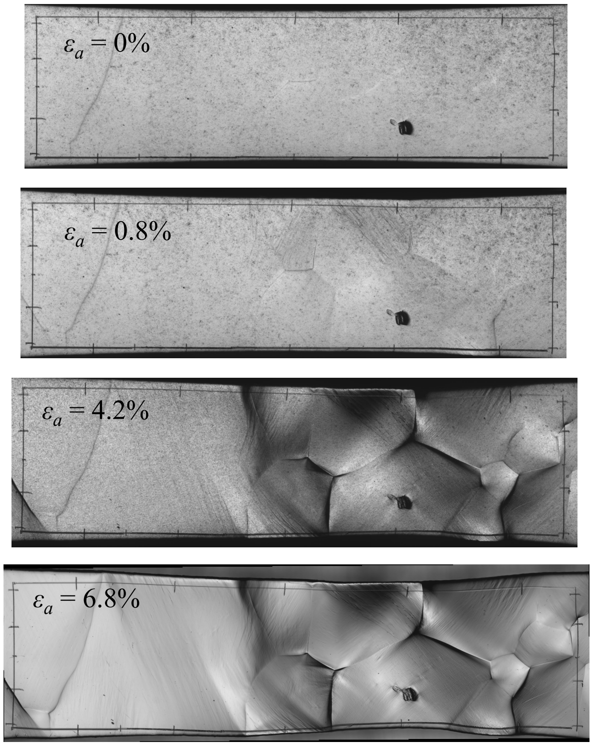

(a) Specimen 1

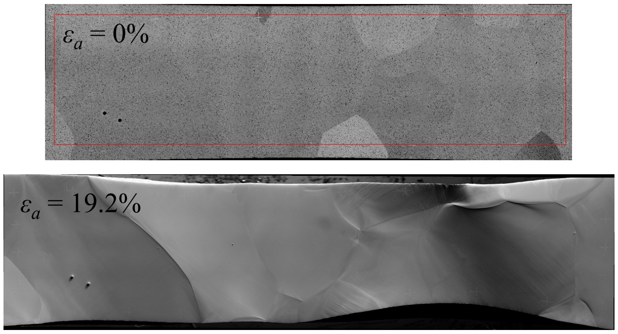

(b) Specimen 2

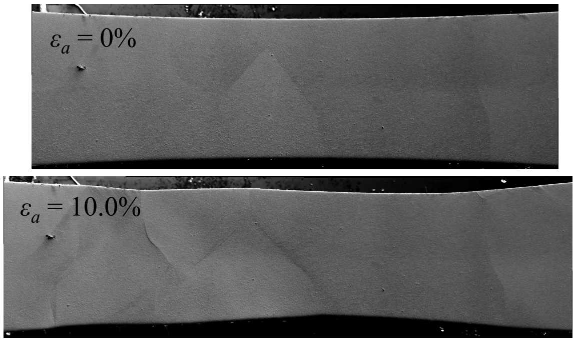

(c) Specimen 3

Figure 22. Surface images of specimens 1 - 3 at different applied strains.

5.2 Simulation Procedures

The entire gage sections of tensile specimens were meshed using a total of 1,426,650, 1,664,150 and 2,140,020 eight-noded hexahedral finite elements for specimens 1, 2 and 3, respectively. As shown in Figure 23, it is assumed that grains are perfectly columnar. A splined mesh was used to create smooth grain boundaries with finer elements placed near grain boundaries as more heterogeneous deformation near the grain boundary was expected. To capture the through-thickness stress and strain distributions and to maintain good aspect ratios of finite elements, 50 (specimens 1 and 2) and 60 (specimen 3) through-thickness elements were used. Thus, the total numbers of surface elements are 28,533, 33,283 and 35,667 for specimens 1, 2 and 3, respectively. Note that the total number of EBSD data points (or pixels) on the surface, are around 319,000, 485,000 and 782,000, respectively, are about an order of magnitude larger than the total numbers of surface elements used in the simulations.

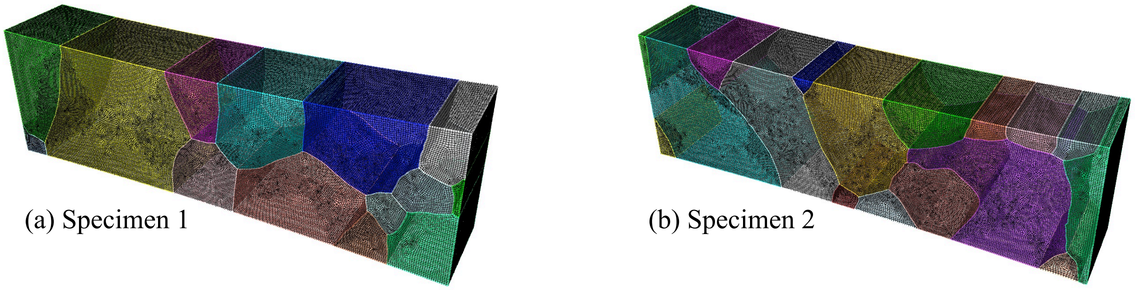

(a) Specimen 1

(b) Specimen 2

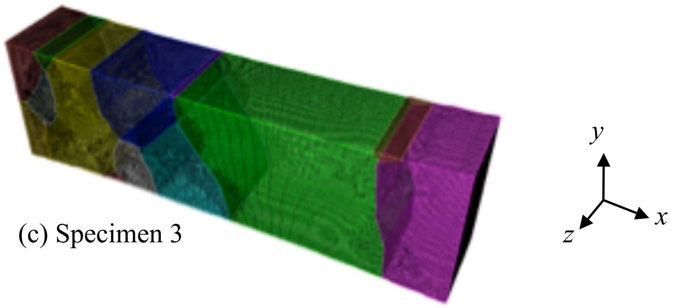

(c) Specimen 3

Figure 23. Finite element meshes of three oligocrystal specimens. The gage sections were meshed using the total numbers of 1,426,650, 1,664,150 and 2,140,020 hexahedral finite elements for oligocrystal specimens 1, 2 and 3, respectively.

The crystallographic orientation of each finite element in the simulation was determined by superimposing the mesh onto the EBSD map; each element was assigned the grain orientation corresponding to the nearest EBSD pixel. Note that crystal orientations were assigned on a element-wise (not grain-wise) basis, and that the crystal orientations were initially identical through the thickness (i.e. initial surface orientations are extruded through the specimen thickness). Figures 24 (a) - (c) show initial crystal orientations of three oligocrystals in RD, TD and ND. It is shown that initial crystal orientations used in the simulations accurately reproduces measured crystal orientations in

Figures 17 - 19.

Material constants used in the simulations are listed in Tables 1 and 4. Note that τ_0^{LT}, τ_0^{EI}, $\dot{\varepsilon}_0$ and $2H_k$ were obtained by fitting the EI and LT models (Equations (26) and (27)) to tantalum single crystal experiments [106, 69] while elastic constants and the Burgers vector for tantaltum were obtained from the literature [49]. κ_1, κ_2 and the initial obstacle strength, $\tau_{\mathrm{obs},0}$, that determine the shape of the strain hardening and the yield stress were parameterized from the measured stress-strain data, Figure 21 (b). Hardening curves of all three specimens were parameterized using $\kappa_1 = 1.4 \times 10^6\ \mathrm{m}^{-1}$ and $\kappa_2 = 15$. On the other hand, $\tau_{\mathrm{obs},0}$ that determines the initial yield strength was 27 MPa, 37 MPa and 27 MPa for specimens 1, 2 and 3 respectively. This deviation in $\tau_{\mathrm{obs},0}$ between specimens may be attributed to different initial dislocation densities, possibly because the samples were harvested from different locations in the rolled plate. This difference is relatively insignificant for this work since $\tau_{\mathrm{obs},0}$ has little influence on strain field and texture predictions at large deformation.

Figures 25 (a) - (c) compare observed and simulated deformed specimens 1 - 3 after 6.8 %, 19.2 % and 10.0 % applied strains, respectively. Deformed shapes from CP-FEM simulations agree relatively well to the actual deformed shape from the uniaxial tension tests, especially for specimens 1 and 3. However, the model prediction does not agree well for specimen 2 where specimen is deformed more severely. Also note that the deformed surface images show arrays of slip lines and larger deformation near the grain boundaries.

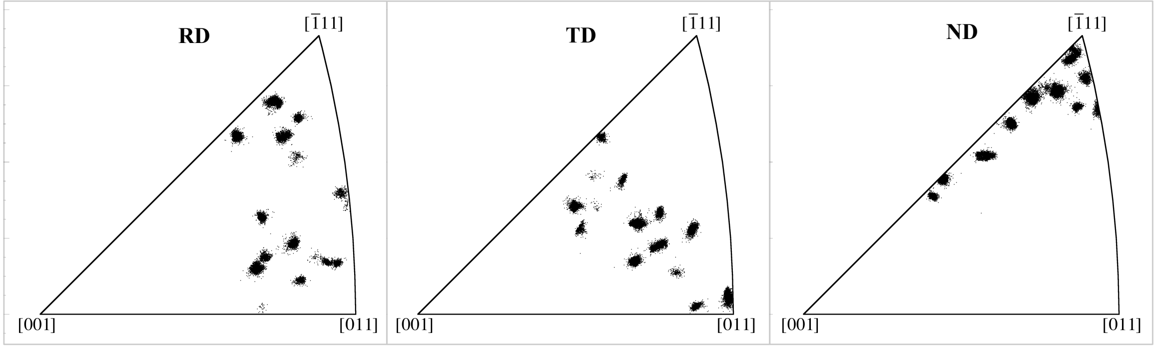

(a) Specimen 1

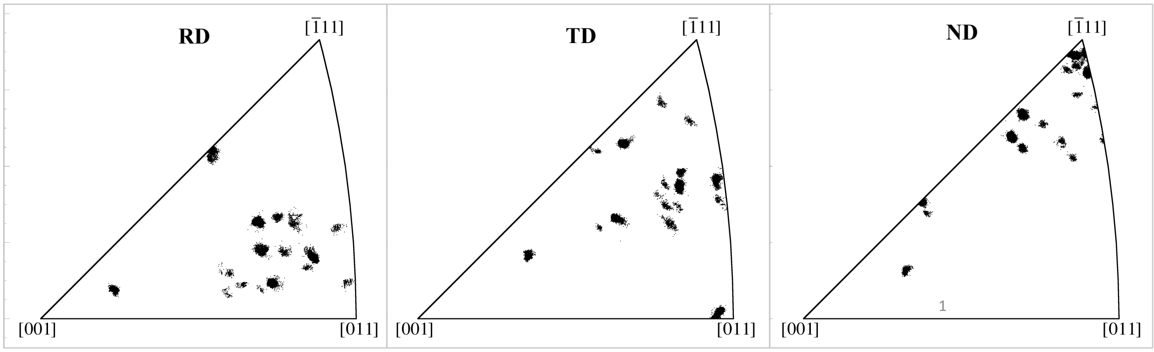

(b) Specimen 2

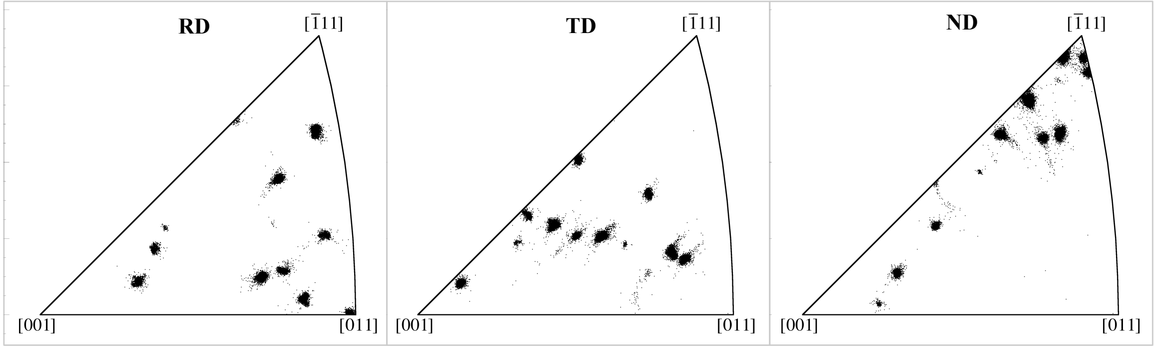

(c) Specimen 3

Figure 24. Initial crystal orientations used in CP-FEM simulations in RD, TD and ND of oligocrystal specimens 1, 2 and 3, respectively.

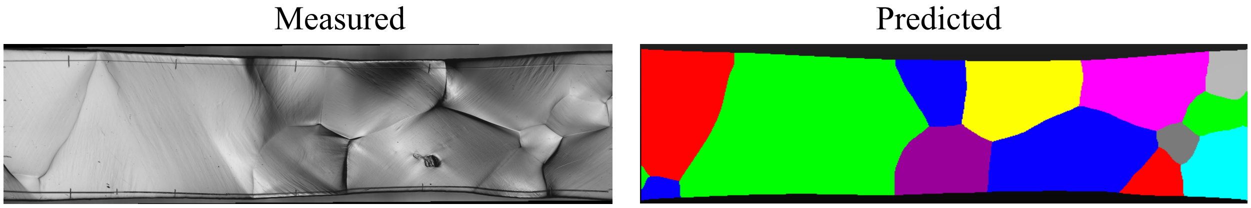

(a) Specimen 1 (6.8%)

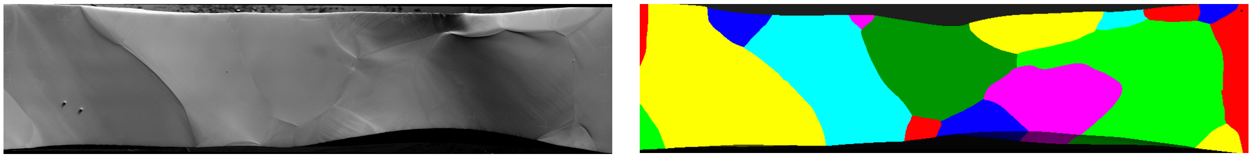

(b) Specimen 2 (19.2%)

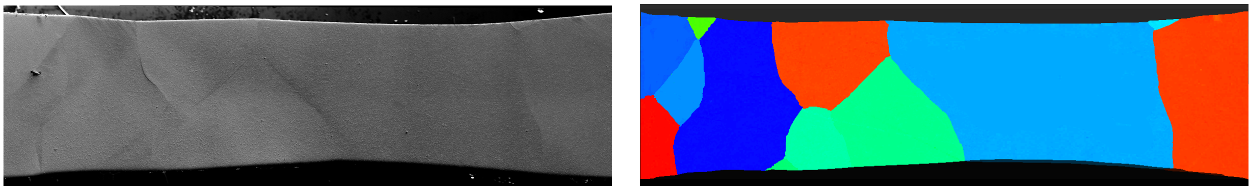

(c) Specimen 3 (10.0%)

Figure 25. Measured and predicted deformed specimens. A surface image obtained from the optical microscope. (a) Specimen 1 at the applied strain of 6.8%, (b) specimen 2 at the applied strain of 19.2%, and (c) specimen 3 at the applied strain of 10.0%.

5.3 Strain Field Analysis: HR-DIC vs. CP-FEM

The displacement fields throughout the gage section of specimen 1 were obtained from the HR-DIC measurements at var- ious applied strains of 0 %, 0.8 %, 4.2 % and 6.8 %. The surface strain fields, ε_{xx}, ε_{yy} and ε_{xy}, were obtained from HR-DIC measurements at three incremental strains: Points A to B ($\Delta\varepsilon_{AB}$=0.8%), B to C ($\Delta\varepsilon_{BC}$ = 3.4 %) and C to D ($\Delta\varepsilon_{CD}$ = 2.6 %). Note that at each strain increment, strain fields relative to the last step are obtained.

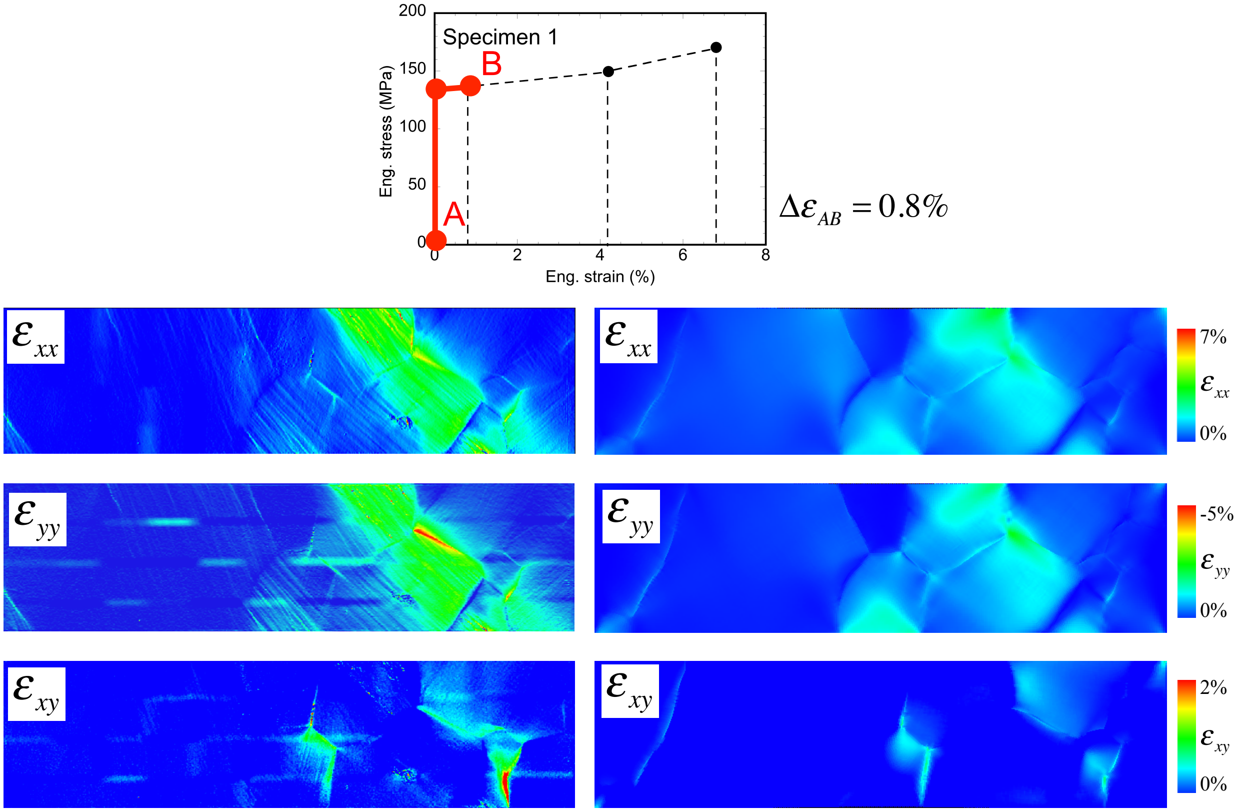

(a) HR-DIC measurements

(b) CP-FEM predictions

Figure 26. A comparison of measured and predicted ε_{xx}, ε_{yy} and ε_{xy} maps for specimen 1 at $\Delta\varepsilon_{AB}$=0.8% (Point A to B).

Figures 26 - 28 compare measured and predicted surface strain fields, ε_{xx}, ε_{yy} and ε_{xy}, of specimen 1 at different strain increments. A comparison of measured and predicted strain field distributions show good quantitative agreements for all strain increments. The model accurately captures locations where the maximum and minimum strain fields are observed. Predicted strain fields agree very well especially at lower applied strain, $\Delta\varepsilon_{AB}$ and $\Delta\varepsilon_{CD}$, as shown in Figures 26 and 27. However, the model fails to capture observed slip lines and detailed strain localizations. Some of these deviations may contribute to defects or microstructure that exist in subsurface that cannot be captured with the surface EBSD measurements. In addition, grain boundary effects such as grain

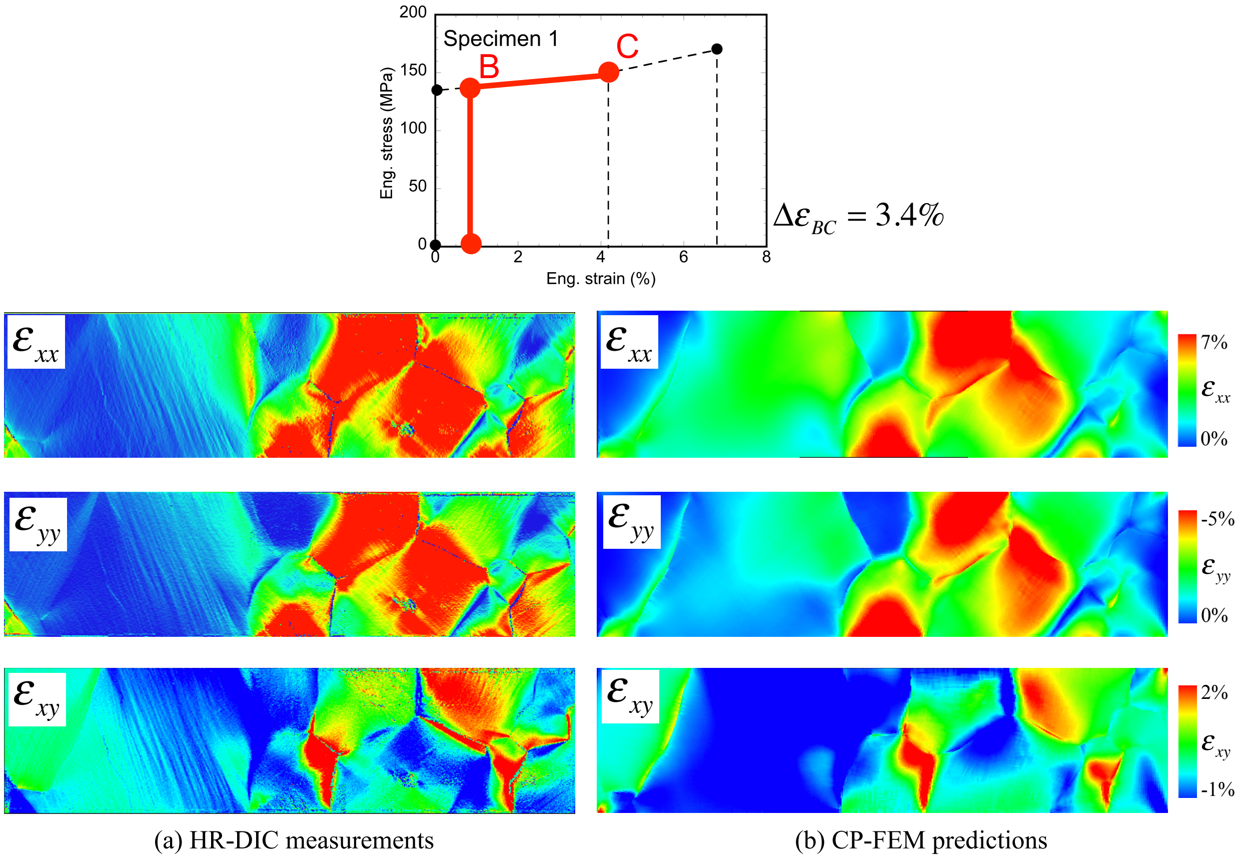

(a) HR-DIC measurements

(b) CP-FEM predictions

Figure 27. A comparison of measured and predicted ε_{xx}, ε_{yy} and ε_{xy} maps for specimen 1 at $\Delta\varepsilon_{BC}$=3.4% (Point B to C).

boundary strengthening/ weakening due to dislocation pile up or accumulation of impurities, are ignored in this model.

Because the CP-FEM model is three-dimensional, it should be able to accurately predict out-of-plane deformations in addition to in-plane strains. Optical profilometry provided measures of displacement gradients (similar, but not equal to out-of-plane shear strains) on the front surface of specimen 1 at 6.8 % applied strain. Model predictions of displacement gradients are compared to these experimental measurements in Figures 29 (a) and (b). The measured and predicted $\partial w/\partial x$ and $\partial w/\partial y$ maps show reasonably good agreement. Thus, the model not only captures in-plane strain fields well but out-of-plane deformations are also correctly predicted.

Figures 30 and 31 show measured and predicted surface strain fields of oligocrystal specimen 2. Here, strain fields at the strain increments from B' to C' ($\Delta\varepsilon_{B'C'}$ = 3.5 %) and B' to D' ($\Delta\varepsilon_{B'D'}$ = 7.0 %) are compared. Similar to specimen 1, CP-FEM predictions of surface strain fields agrees relatively well with the measurement. However, the model failed to capture strain localizations near the grain boundaries.

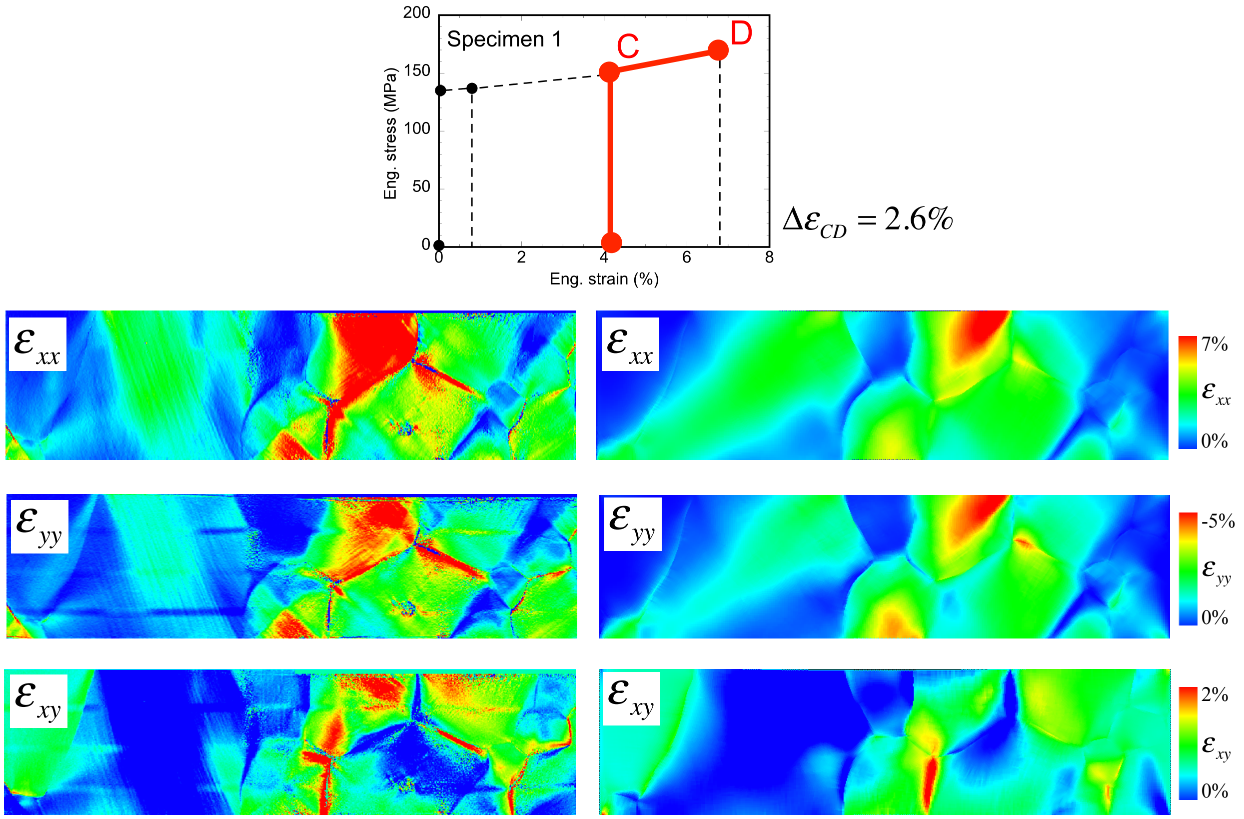

(a) HR-DIC measurements

(b) CP-FEM predictions

Figure 28. A comparison of measured and predicted ε_{xx}, ε_{yy} and ε_{xy} maps for specimen 1 at $\Delta\varepsilon_{CD}$=2.6% (Point C to D).

Figures 32 – 34 compare measured and simulated surface Lagrangian strain fields, ε_{xx}, ε_{yy} and ε_{xy}, respectively, at five applied strains (ε_a =2, 4, 6, 8 and 10 %). The CP-FEM model qualitatively captures the heterogeneous intergranular surface strain fields observed in HR-DIC measurements including the locations of localized strain fields at different applied strains. As shown in Figures 32 and 33, large tensile ε_{xx} and compressive ε_{yy} strains were observed in grains 1 and 4 while grain 5 showed less deformation, Furthermore, the model accurately predicted large shear strains, ε_{xy}, in grains 5 and 6 and near the grain boundaries associated with grains 2-6, 2-8, and 2-9. However, some detailed features observed in DIC measurements, i.e. slip lines (at $epsilon_a = 2\%$) and localized strain fields between grains 1 and 4 (at $\varepsilon_a = 10\%$), were not captured with the model.

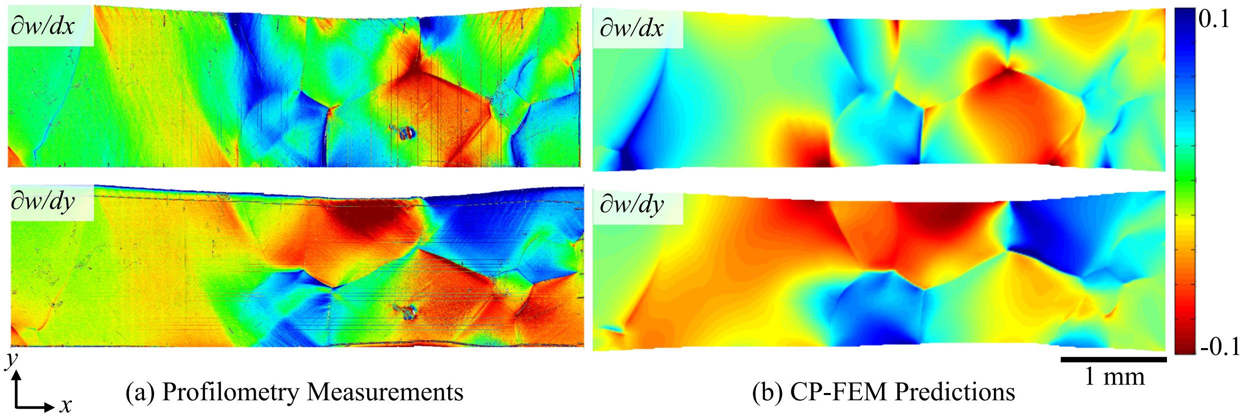

(a) Profilometry Measurements (b) CP-FEM Predictions

Figure 29. A comparison of measured and predicted ε_{xz} and ε_{yz} maps for specimen 1 at 6.8 % uniaxial tensile strain. (a) profilometry measurement and (b) CP-FEM prediction.

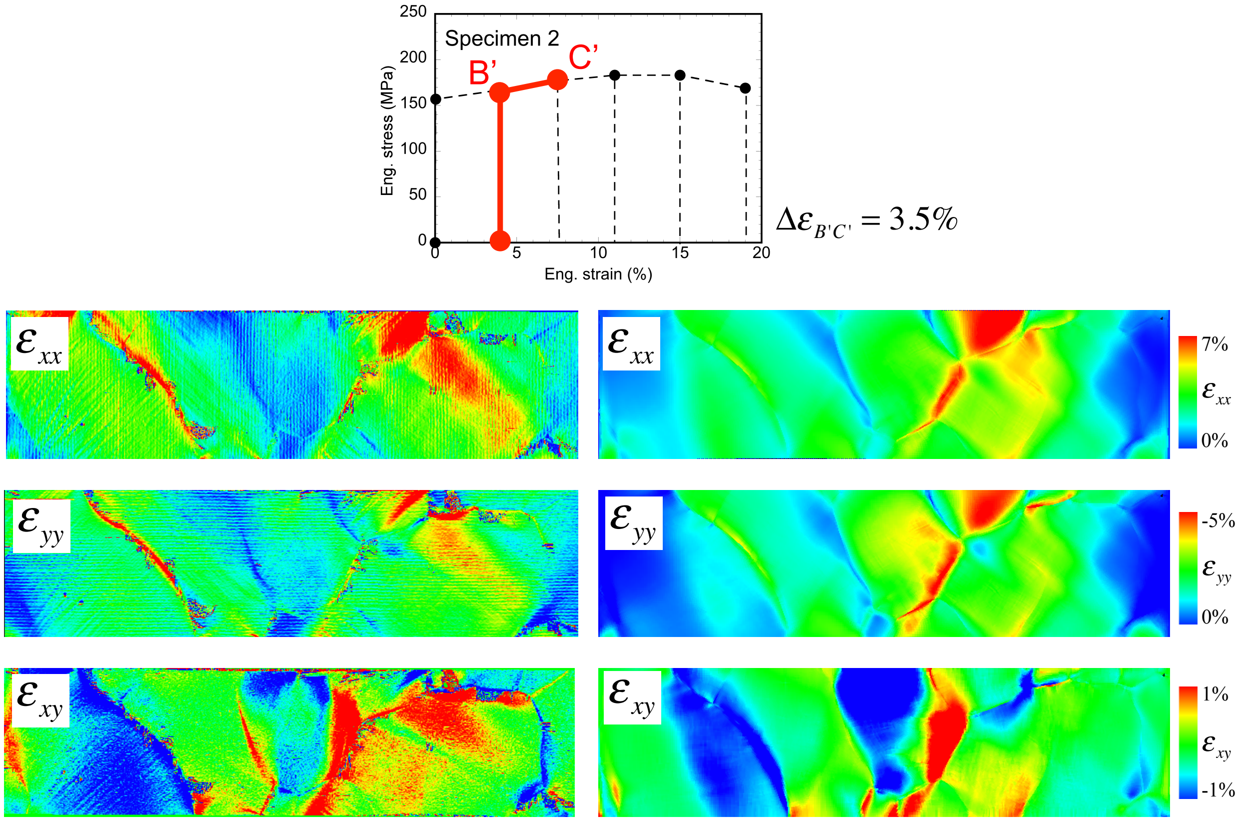

(a) HR-DIC measurements (b) CP-FEM predictions

Figure 30. A comparison of measured and predicted ε_{xx}, ε_{yy} and ε_{xy} maps for specimen 2 at $\Delta\varepsilon_{B'C'}$=3.5% (4.0 to 7.5%).

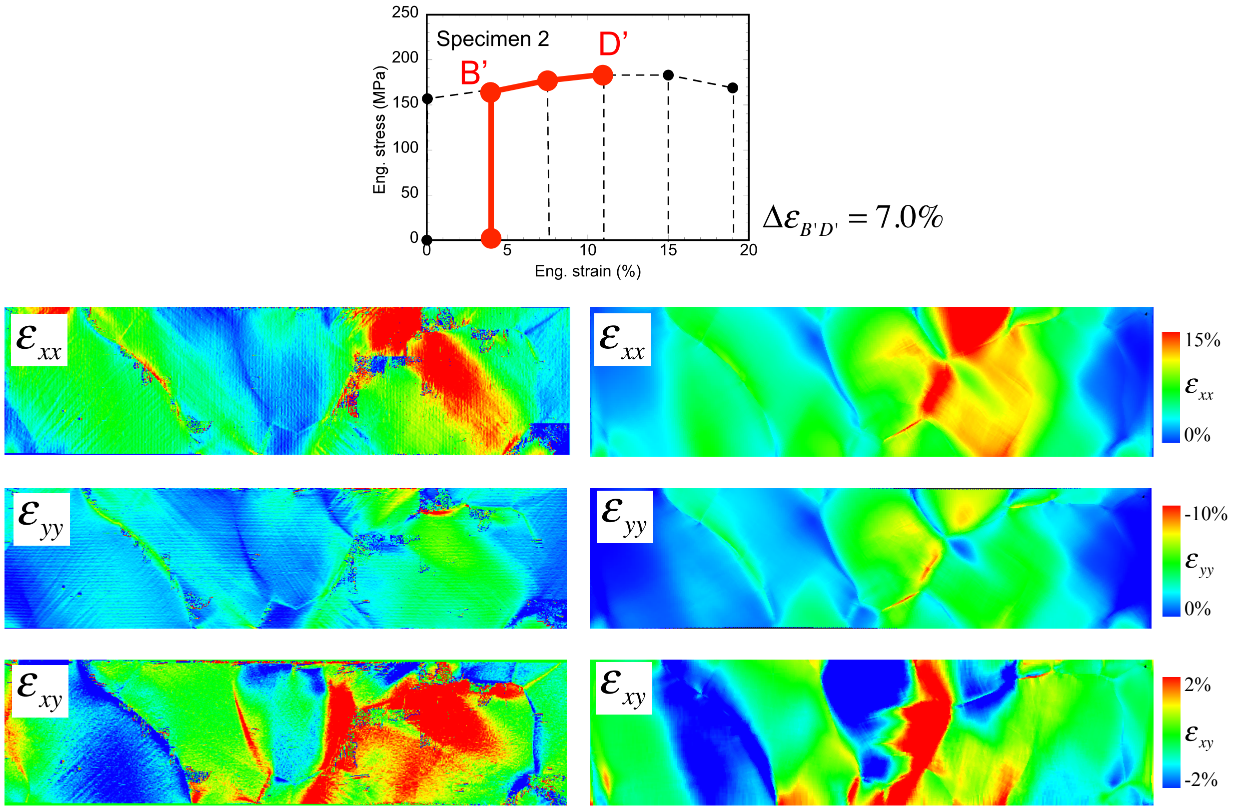

(a) HR-DIC measurements

(b) CP-FEM predictions

Figure 31. A comparison of measured and predicted ε_{xx}, ε_{yy} and ε_{xy} maps for specimen 2 at $\Delta\varepsilon_{B'D'}$=7.0% (4.0 to 11.0%).

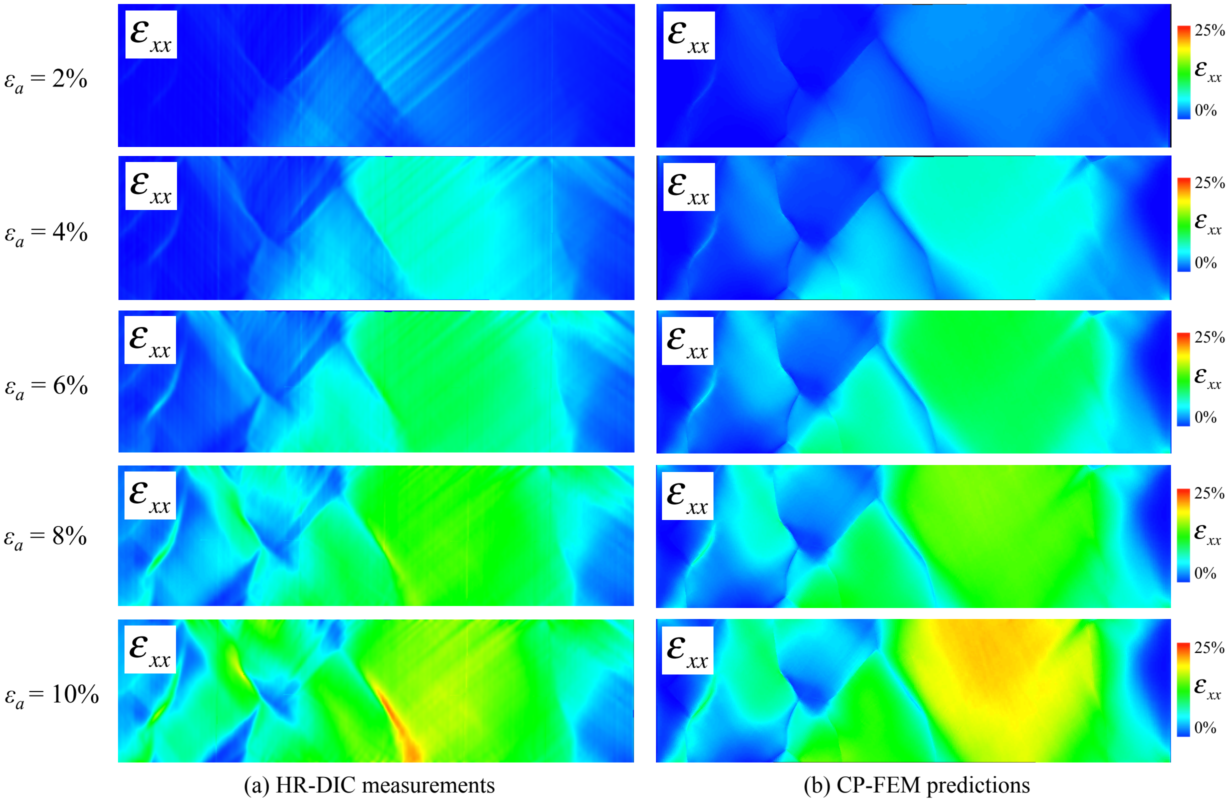

(a) HR-DIC measurements

(b) CP-FEM predictions

Figure 32. A comparison of measured (HR-DIC) and predicted (CP-FEM) ε_{xx} at applied strains (ε_a) of 2 %, 4 %, 6 %, 8 % and 10 % for specimen 3.

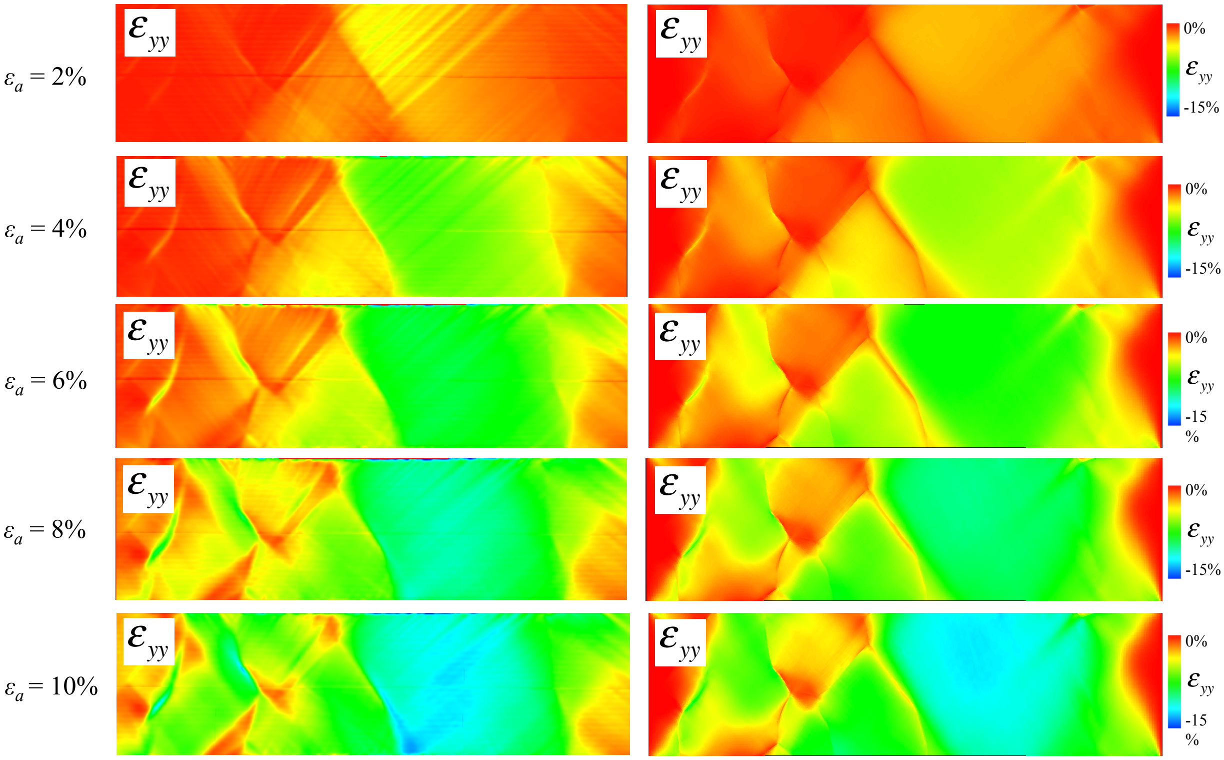

(a) HR-DIC measurements (b) CP-FEM predictions

Figure 33. A comparison of measured (HR-DIC) and predicted (CP-FEM) ε_{yy} at applied strains (ε_a) of 2 %, 4 %, 6 %, 8 % and 10 % for specimen 3.

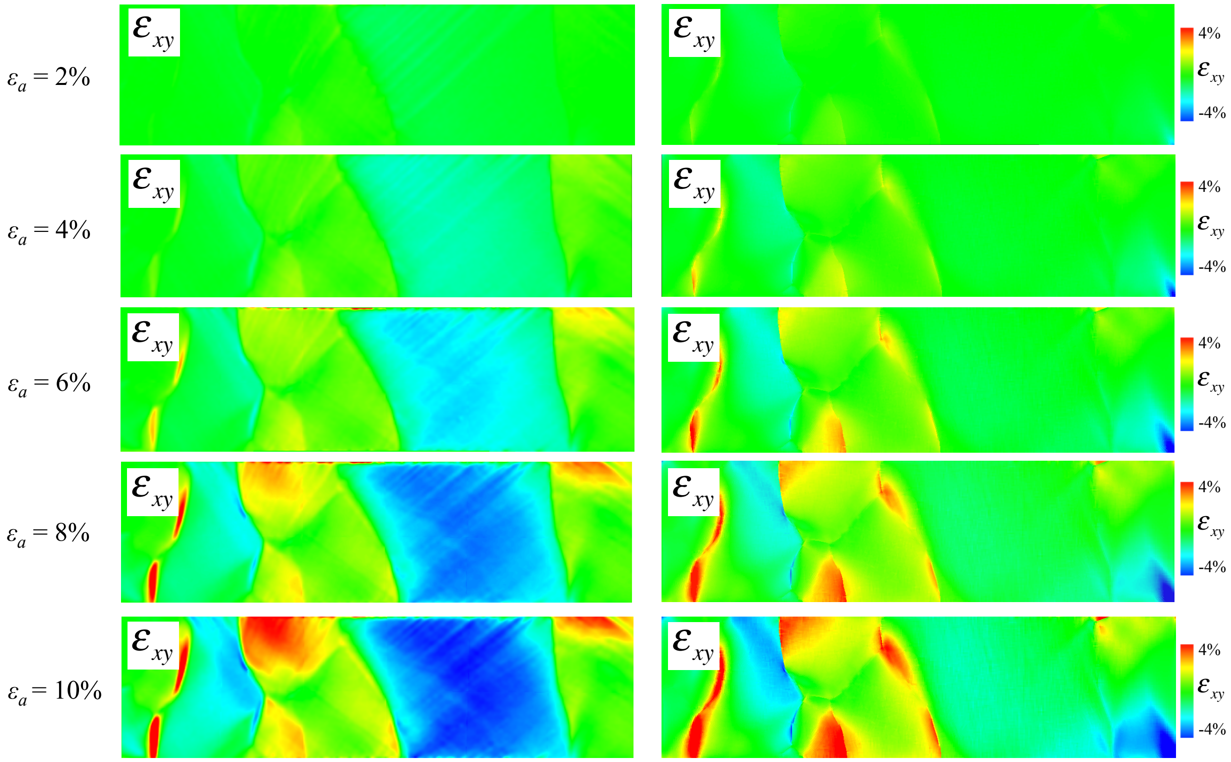

Figure 34. A comparison of measured (HR-DIC) and predicted (CP-FEM) ε_{xy} at applied strains (ε_a) of 2 %, 4 %, 6 %, 8 % and 10 % for specimen 3.

To quantitatively compare measured and predicted surface strain fields, the DIC data (781,015 data points) was imposed on to the finite element mesh (35,667 surface elements), similar to the procedure used to assign the initial EBSD data to the model. By assigning DIC data on surface finite elements used in the simulation, the experimental measurement and model predictions can be objectively compared on a point-wise basis. In this procedure, the size of the DIC data was reduced by a factor of 22. Figures 35 (a) and (b) show ε_{xx} at 10 % applied strain from the full HR-DIC data and reduced data, respectively. As shown in Figure 35, this reduction appears to have relatively small effect on the resolution of the strain field. This may indicate that DIC resolution was more than sufficient to resolve the observed strain localizations and that a lower resolution would have been adequate, especially for comparisons with continuum-scale model predictions.

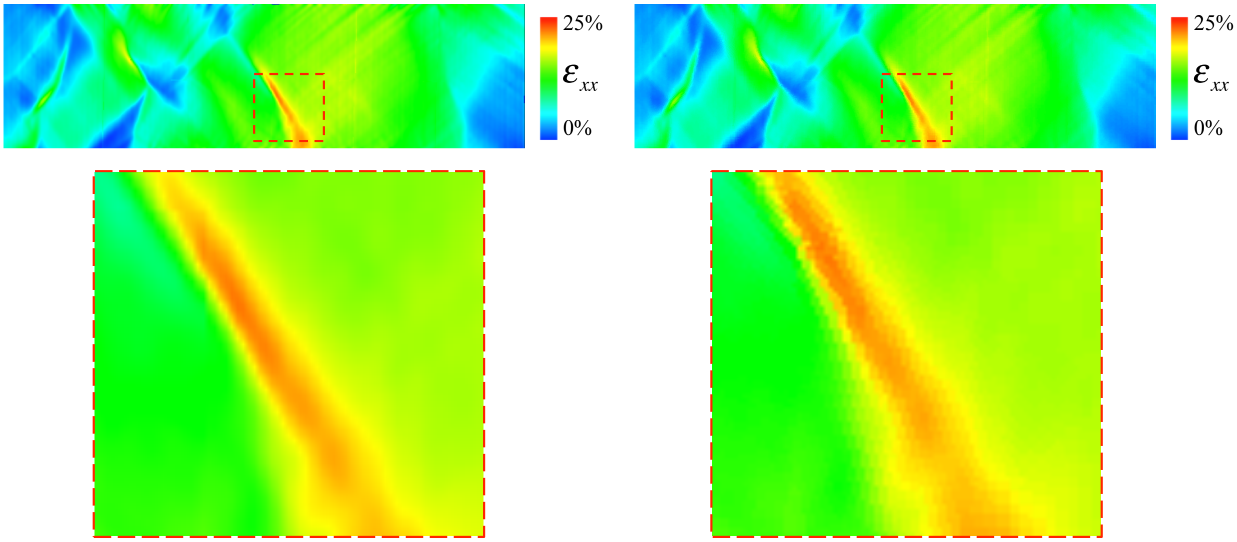

(a) Full DIC data

(b) Reduced DIC data

Figure 35. Plots of ε_{xx} at 10 % applied strain using (a) full HR-DIC data (781,015 data points) and (b) reduced DIC data, imposed on to finite element mesh (35,667 data points).

Using HR-DIC measurements and CP-FEM predictions of strain fields with the same data resolution, deviations between two data sets were obtained as follows:

$$\Delta\varepsilon = \varepsilon^{\mathrm{DIC}} - \varepsilon^{\mathrm{sim}}, \tag{40}$$

where. $\varepsilon^{\mathrm{DIC}}$ and $\varepsilon^{\mathrm{sim}}$ represent surface strain fields obtained from DIC and CP-FEM simulations, respectively, for each element. Figure 36 shows calculated $\Delta\varepsilon_{xx}$ maps at different applied strain levels. Positive values (red) represent regions where simulation under-predicts strain fields while negative values (blue) show over-predicted regions. It is shown that large $\Delta\varepsilon_{xx}$ values were observed near the grain boundaries and locations where slip lines developed in the experiment, especially near grain boundary 1-4.

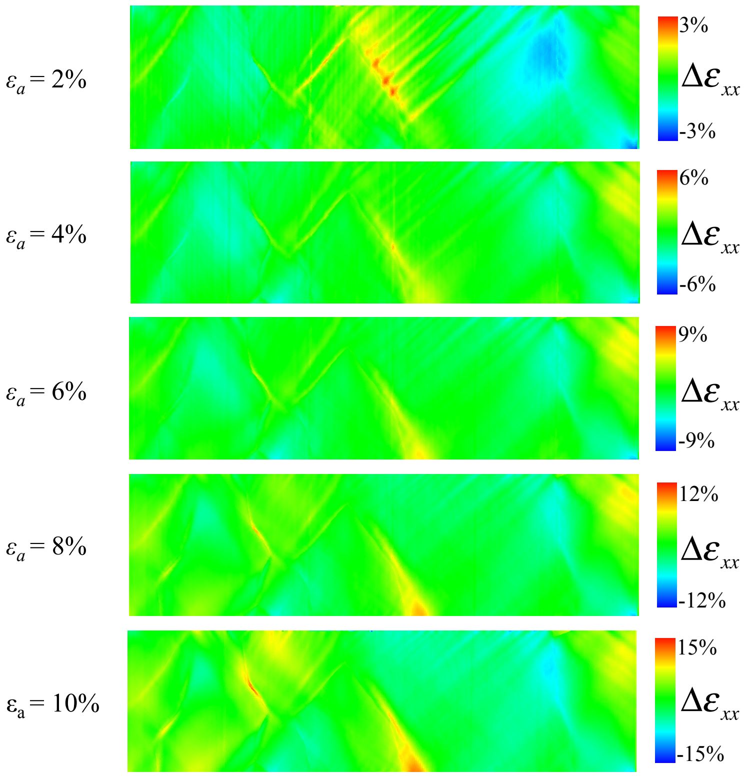

Figure 36. Deviations between measured and simulated surface strain fields, ε_{xx}, at different applied strains. Here, deviations of strain fields are calculated as $\Delta\varepsilon_{xx} = \varepsilon_{xx}^{\mathrm{DIC}} - \varepsilon_{xx}^{\mathrm{sim}}$.

Table 10. Average deviation between measured and simulated strain fields ($\Delta\varepsilon^{avg}$) and relative errors ($\Delta\varepsilon^{avg}/\varepsilon_a$) at various applied strains within the whole specimen.

	Applied strain (ε_a)				
	2 %	4%	6%	8%	10%
$\Delta\varepsilon_{xx}^{avg}$	0.0073	0.0102	0.0143	0.0215	0.0344
$\Delta\varepsilon_{yy}^{avg}$	0.0059	0.0097	0.0116	0.0142	0.0180
$\Delta\varepsilon_{xy}^{avg}$	0.0031	0.0071	0.0104	0.0136	0.0159
$\Delta\varepsilon_{xx}^{avg}/\varepsilon_a$	0.36	0.26	0.24	0.27	0.34
$\Delta\varepsilon_{yy}^{avg}/\varepsilon_a$	0.30	0.24	0.19	0.18	0.18
$\Delta\varepsilon_{xy}^{avg}/\varepsilon_a$	0.16	0.18	0.17	0.17	0.16

To further quantify the deviation between the measured and predicted strain fields, the quantity $\Delta\varepsilon_{avg}$, defined as follows, was calculated for each strain component within the entire region.

$$\Delta\varepsilon^{avg} = \sqrt{\frac{1}{N}\sum_{i=1}^{N}\left(\varepsilon_i^{\mathrm{DIC}} - \varepsilon_i^{\mathrm{sim}}\right)^2}. \tag{41}$$

Here, N is the total number of data points (N=35,667). Table 10 lists the average deviation between measured and simulated strain fields at various applied strains. The model agreed relatively well with HR-DIC measurement, i.e. average deviation between the model and experiment at 10% deformation for ε_{xx} was around 3% strain.

Table 10 lists the relative error, $\Delta\varepsilon^{avg}/\varepsilon_a$ at all five applied strain levels within the entire specimen. Here, we chose to normalize $\Delta\varepsilon^{avg}$ with ε_a instead of $\varepsilon^{\mathrm{DIC}}$ or $\varepsilon^{\mathrm{sim}}$ per data point to objectively compare deviations at different applied strains and because many $\varepsilon^{\mathrm{DIC}}$ and $\varepsilon^{\mathrm{sim}}$ values were very close to zero. An average value of $\Delta\varepsilon_{xx}^{avg}/\varepsilon_a$ for the whole specimen over five applied strains were 0.29. That is, the difference between model predictions and experimental measurements of ε_{xx} is around 30% of the applied strain. This value could be used as an objective criterion for comparing different models or for investigating effects of model parameters. Note that $\Delta\varepsilon_{xx}^{avg}/\varepsilon_a$ is fairly consistent across the applied strain measurements except for increased values in applied strains of 2 and 10 % compared to 4 – 8 %. As indicated by Figures 32 and 36, increased $\Delta\varepsilon_{xx}^{avg}/\varepsilon_a$ at small strains in grain 1 can likely be attributed to experimentally observed slip lines. At larger strains, large deviation was observed near the grain boundary between grains 1 and 4. This discrepancy indicates a possible deficiency in the model's handling of grain boundaries. Large $\Delta\varepsilon_{xx}^{avg}/\varepsilon_a$ at large strains could also be a result of the model not accounting for damage.

To assess the fidelity of the model prediction per grain basis, averaged $\Delta\bar{\varepsilon}_{xx} = \left(\varepsilon_{xx}^{\mathrm{DIC}} - \varepsilon_{xx}^{\mathrm{sim}}\right)/\varepsilon_a$ within each grain were obtained. Figures 37 (a) and (b) show calculated $\Delta\bar{\varepsilon}_{xx}$ versus the maximum Schmid factor and volume fraction, respectively. As shown in Figure 37 (a), CP-FEM model under-predicted ε_{xx} ($\Delta\bar{\varepsilon}_{xx} > 0$) for grains having low maximum Schmid factors. In particular, grains 12, 5 and 8 having lowest Schmid factors (0.385, 0.392 and 0.414, respectively) and thus representing hardest grains were under-predicted by the model. In addition, the model over-predicted ε_{xx}

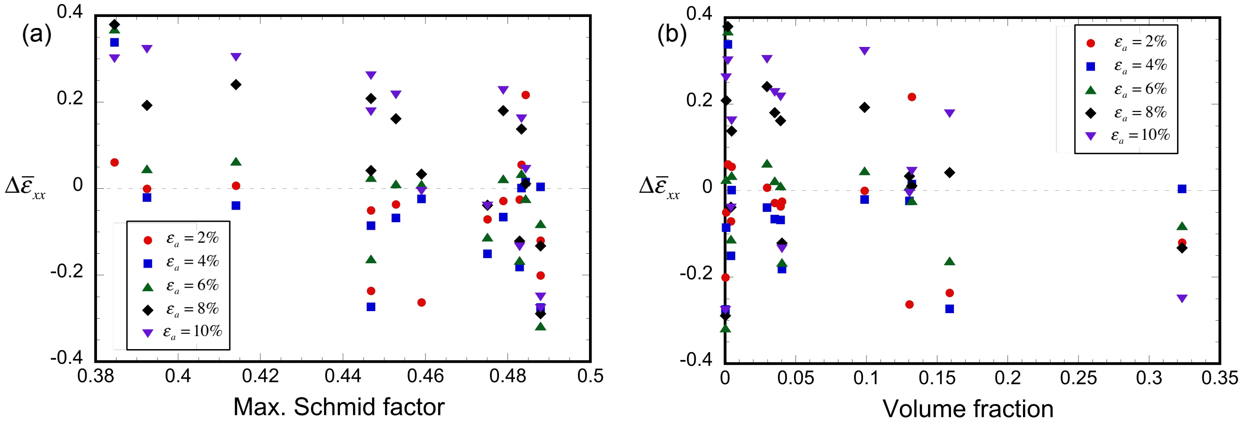

Figure 37. Calculated $\left(\varepsilon_{xx}^{\mathrm{DIC}} - \varepsilon_{xx}^{\mathrm{sim}}\right)/\varepsilon_a$ versus (a) the maximum Schmid factor and (b) volume fraction for each grain.

($\Delta\bar{\varepsilon}_{xx} < 0$) for two softest grains (grains 1 and 14). This result suggests that the CP-FEM model predictions of strain fields are less accurate in grains having extreme orientations, i.e. softest and hardest grains within the specimen. On the other hand, there was no noticeable correlation between $\Delta\bar{\varepsilon}_{xx}$ and the volume fraction (or the size) of each grain within the gage section as shown in Figure 37 (b).

Although we strive to reproduce the microstructural features of the specimen and test procedures accurately using high resolution experimental techniques and a simple-structured specimen, there still exist various limitations of the current approach. The main possible source of error between the model and simulation is an assumption on columnarity of the specimen. The oligocrystal specimen used in this work does not have a perfectly columnar grain structure and it is likely that initial crystal orientations varied through the thickness direction. While macroscopic mechanical responses of coarse-grained oligocrystals are likely to have small effects from local grain boundary properties, it is clear that a more sophisticated treatment of grain boundaries and grain boundary-dislocation interaction would improve model predictions. This is clearly shown in Figure 36 where the model underpredicted ε_{xx} near grain boundaries as compared to HR-DIC measurements. Furthermore, many material parameters used in the model are assumed to be constant and homogeneous throughout the specimen, i.e. the model does not incorporate any initial heterogeneous distribution of defects.

5.4 Texture Analysis: EBSD vs. CP-FEM

In addition to strain field analysis, crystal orientations and their rotations upon uniaxial tensions are measured and compared with CP-FEM simulations. Figures 38 - 40 show crystal orientation maps of deformed tensile specimens at various applied strains for oligocrystal specimens 1 - 3, respectively. Here, the colors represent the crystal orientations in RD, TD and ND and in specimen, EBSD data were not fully collected in severely deformed regions (in black). It is shown that relatively large crystal rotations were observed near the grain boundaries.

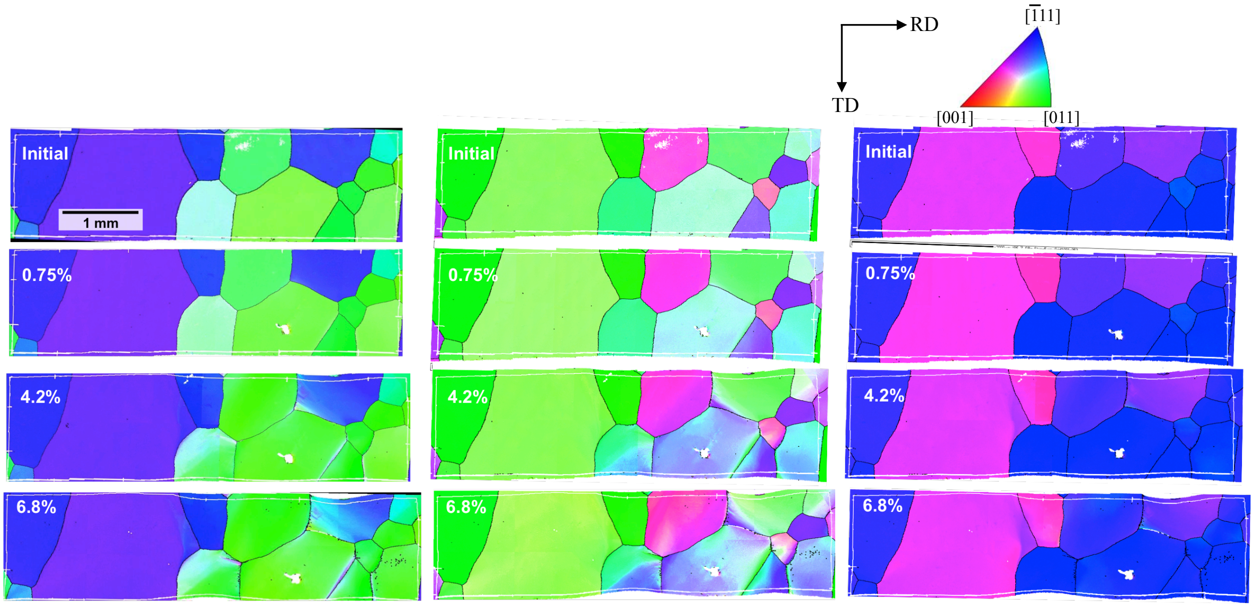

(a) RD (b) TD (c) ND

Figure 38. Crystal orientations obtained from the EBSD measurements at different applied strains for specimen 1 RD, TD and ND.

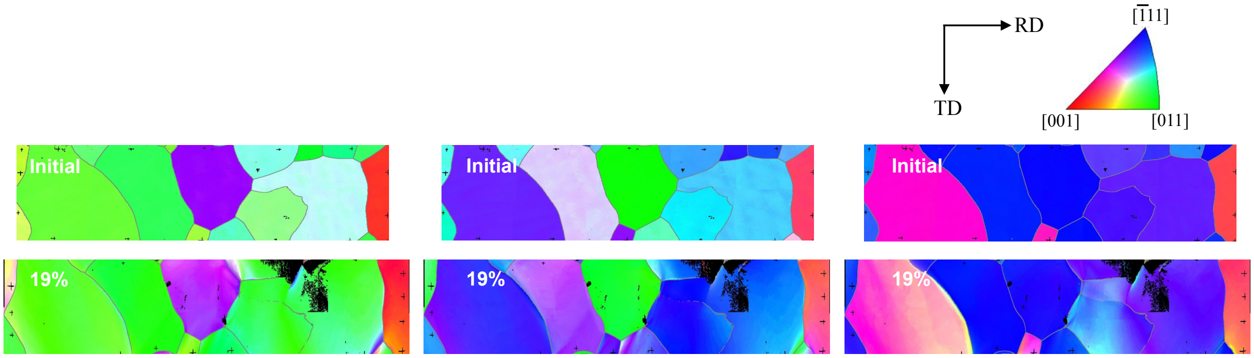

(a) RD (b) TD (c) ND

Figure 39. Initial and deformed (19.0 %) crystal orientations obtained from the EBSD measurements for specimen 2 in RD, TD and ND.

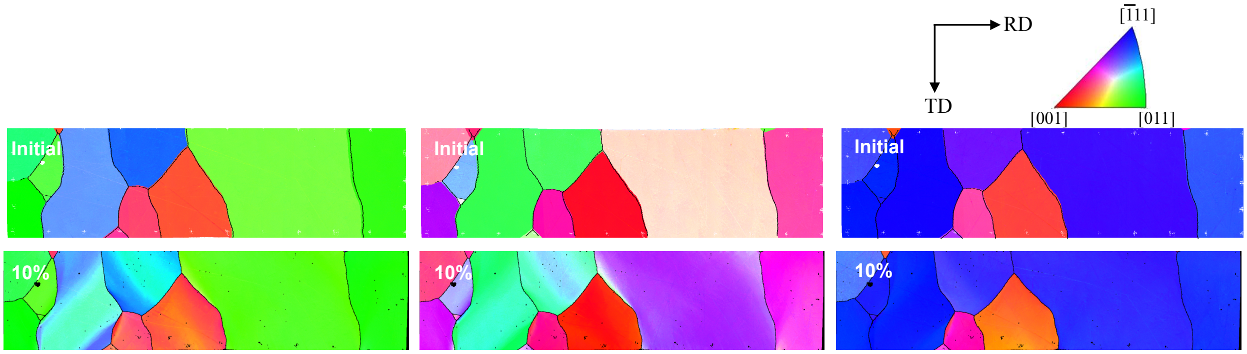

(a) RD (b) TD (c) ND

Figure 40. Initial and deformed (10.0 %) crystal orientations obtained from the EBSD measurements for specimen 3 in RD, TD and ND.

Figures 41 - 43 show the measured and predicted textures of specimen 1-3 in RD, ND and TD. For all three cases, initial crystal orientations obtained from the EBSD are accurately reproduced by the model and the predicted deformed textures show qualitatively good agreement with EBSD measurements. There were scattered initial crystal orientations within the same grain that may attribute to both actual variations of the crystal orientation within the grain and the experimental scatter or the noise in EBSD data. Although there are some studies exploring the orientation noise in EBSD data [43], it is very difficult to separate these two effects.

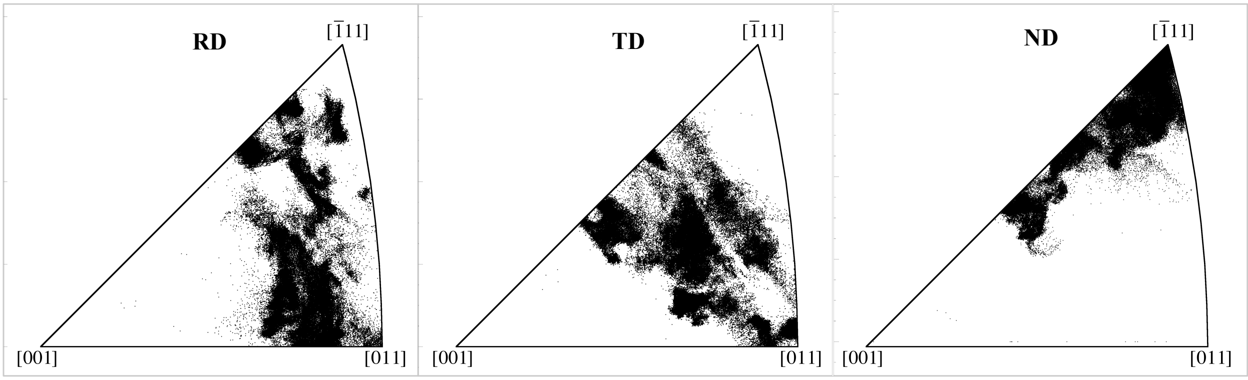

(a) Measured (EBSD)

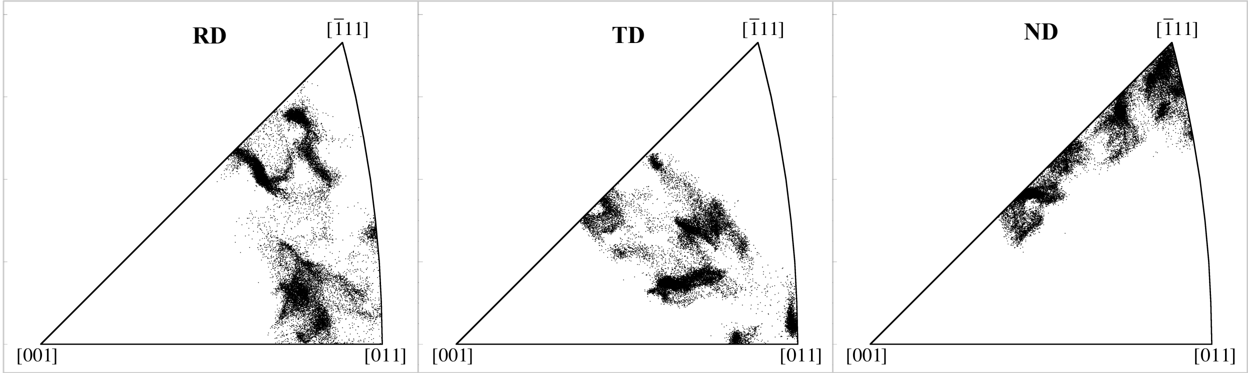

(b) Predicted (CP-FEM)

Figure 41. Deformed texture within the unit stereographic triangle of specimen 1 at the applied strain of 6.8 % in RD, TD and ND. (a) EBSD measurement and (b) CP-FEM prediction.

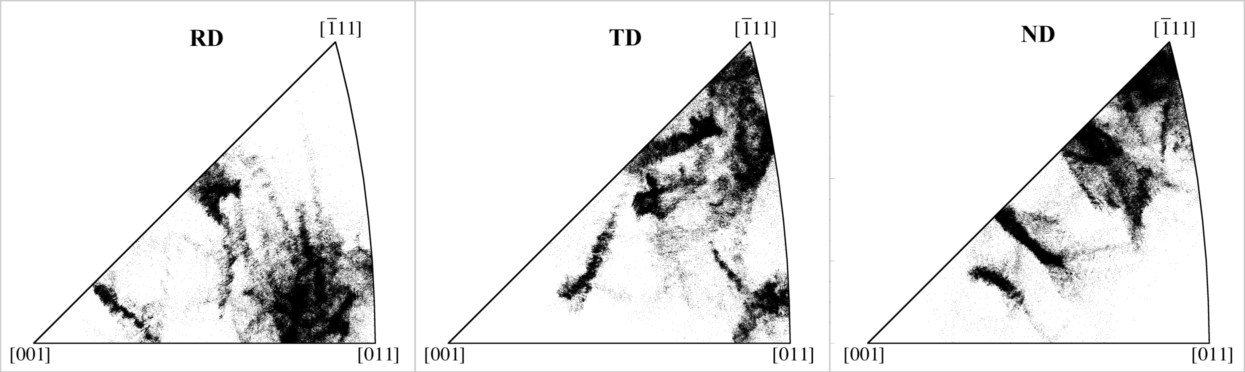

(a) Measured (EBSD)

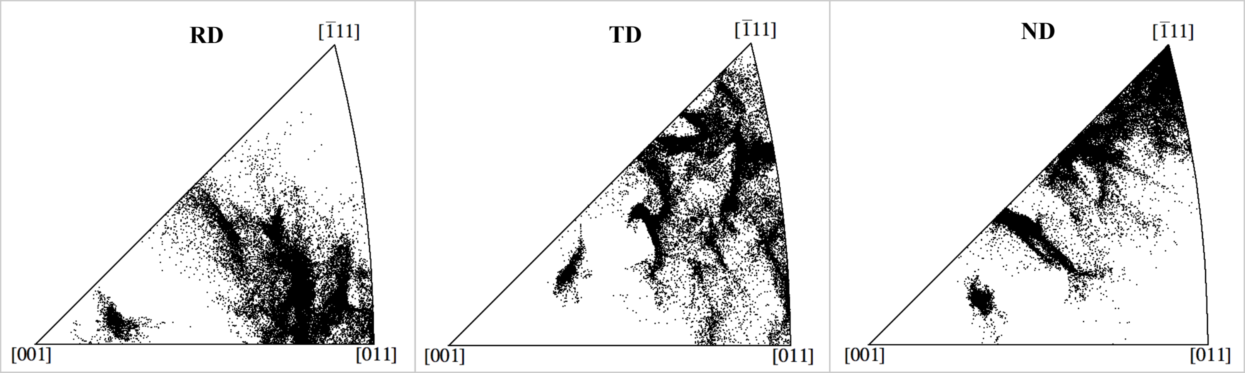

(b) Predicted (CP-FEM)

Figure 42. Deformed texture within the unit stereographic triangle of specimen 2 at the applied strain of 19.2 % in RD, TD and ND. (a) EBSD measurement and (b) CP-FEM prediction.

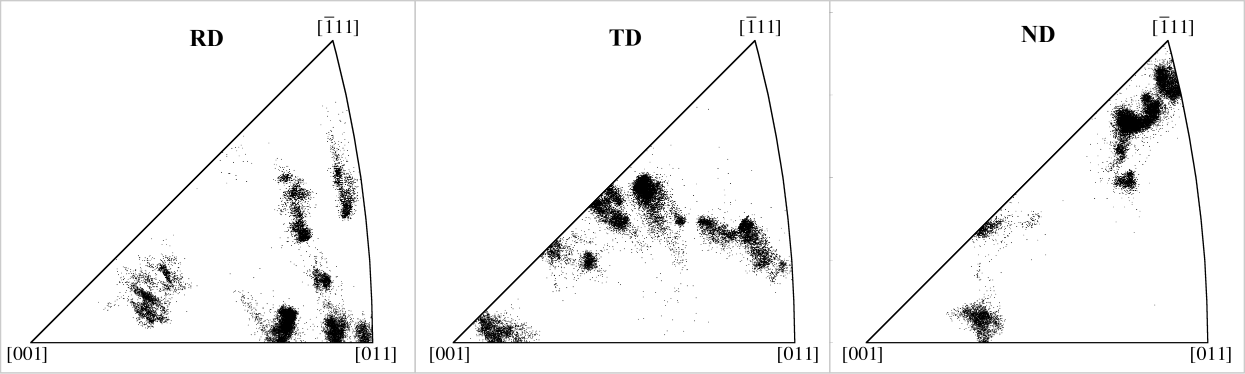

(a) Measured (EBSD)

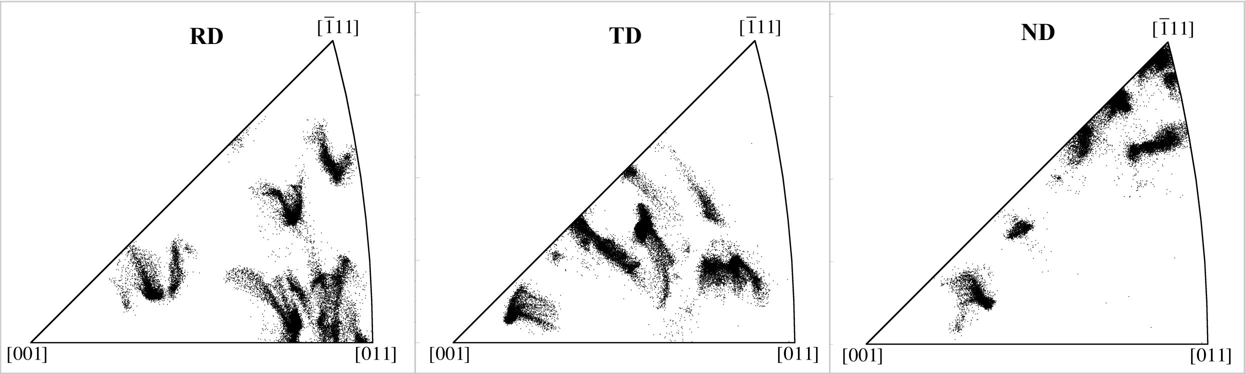

(b) Predicted (CP-FEM)

Figure 43. Deformed texture within the unit stereographic triangle of specimen 3 at the applied strain of 10.0 % in RD, TD and ND. (a) EBSD measurement and (b) CP-FEM prediction.

Figures 44 - 46 shows the intensity plot of crystal orientations obtained from EBSD and CP-FEM simulation of deformed specimen. Here, the number of data points within the unit area of stereographic triangle are normalized by the total number of data points. Figures 44 - 46 show that the simulated texture agrees well quantitatively.

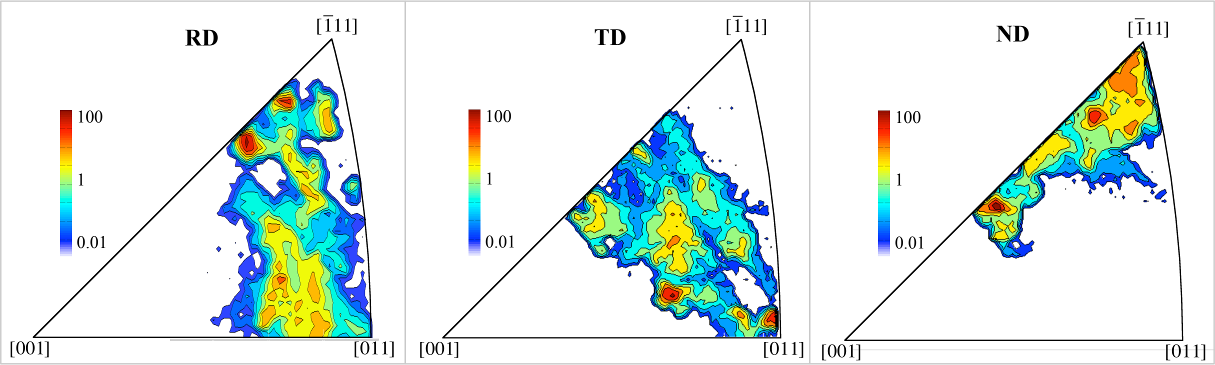

(a) Measured (EBSD)

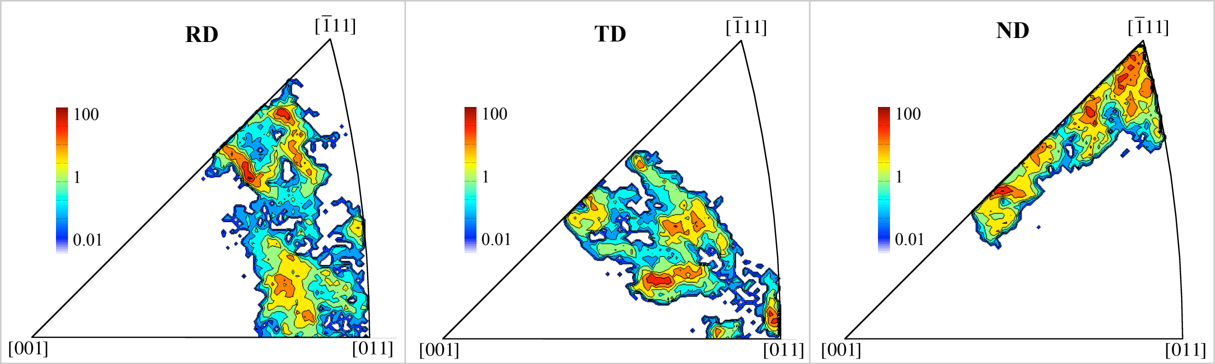

(b) Predicted (CP-FEM)

Figure 44. Intensity plots of crystal orientations within the unit stereographic triangle of specimen 1 at the applied strain of 6.8 % in RD, TD and ND. (a) EBSD measurement and (b) CP-FEM prediction.

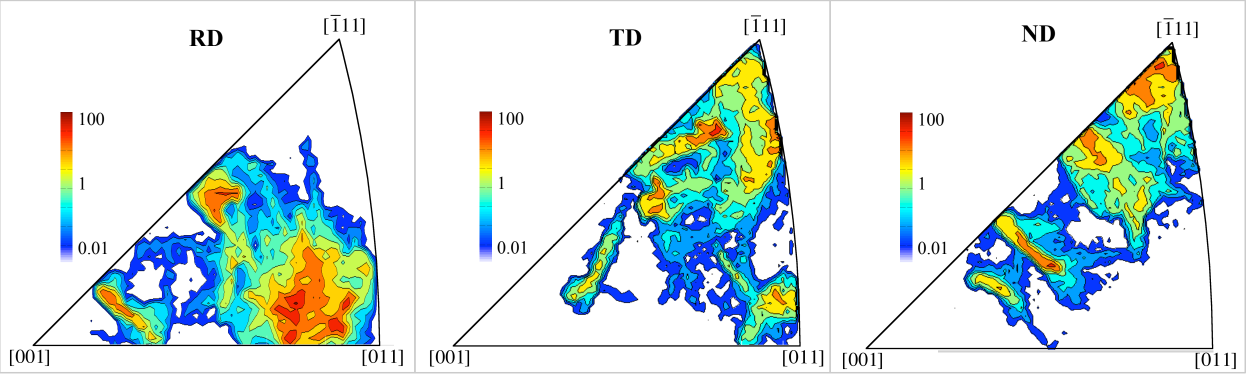

(a) Measured (EBSD)

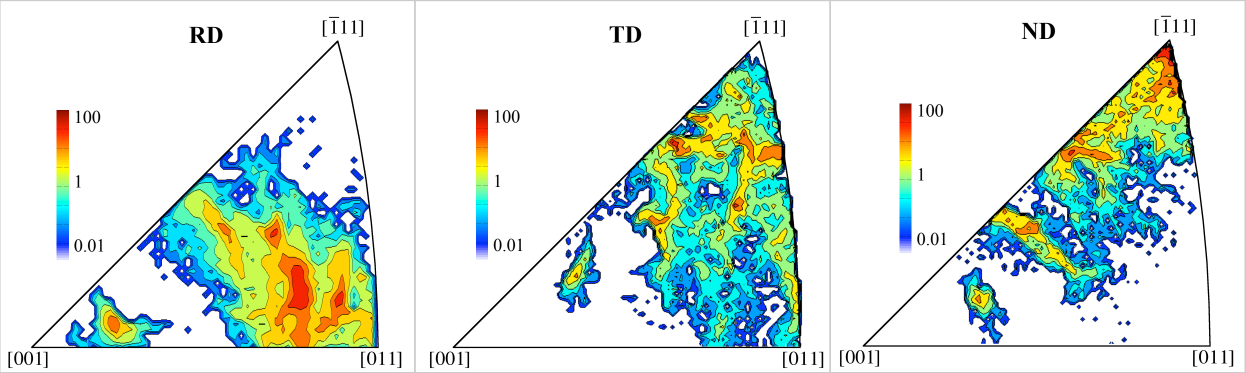

(b) Predicted (CP-FEM)

Figure 45. Intensity plots of crystal orientations within the unit stereographic triangle of specimen 2 at the applied strain of 19.2 % in RD, TD and ND.(a) EBSD measurement and (b) CP-FEM prediction.

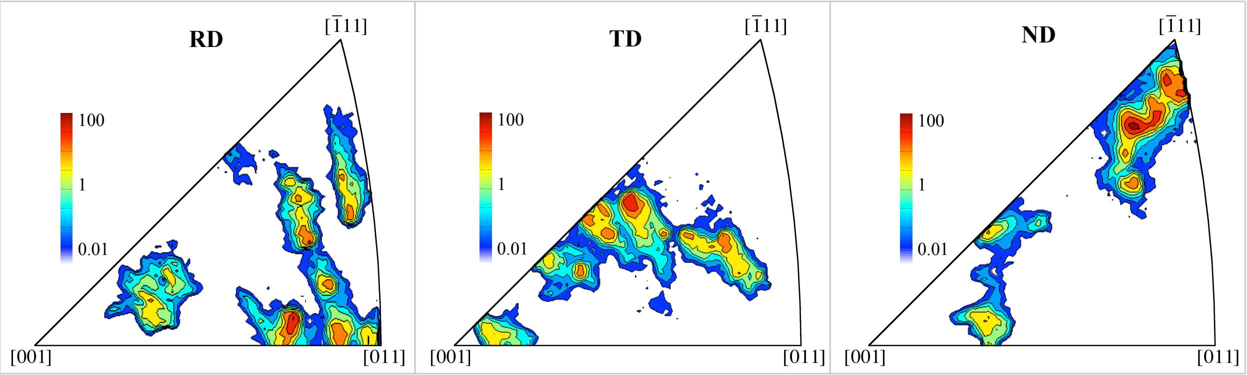

(a) Measured (EBSD)

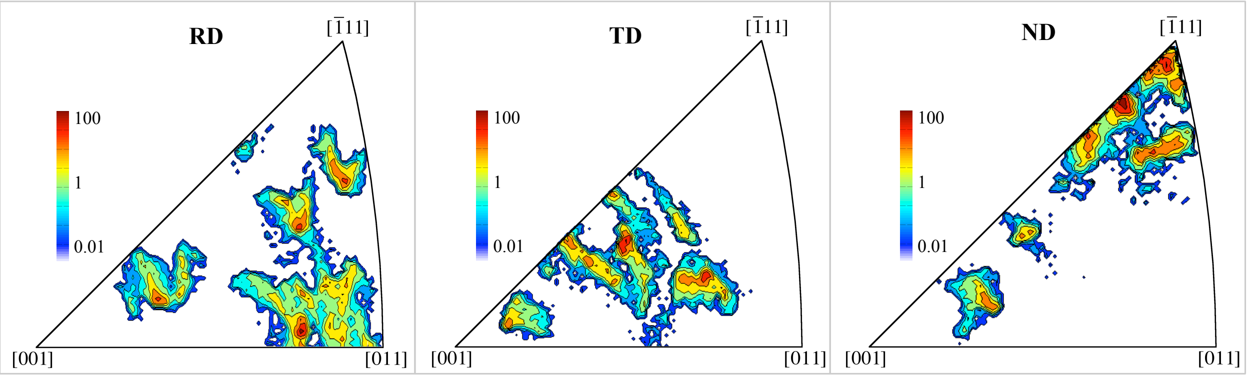

(b) Predicted (CP-FEM)

Figure 46. Intensity plots of crystal orientations within the unit stereographic triangle of specimen 3 at the applied strain of 10.0 % in RD, TD and ND. (a) EBSD measurement and (b) CP-FEM prediction.

Although measured and predicted texture show relatively good agreement, noticeable deviation was observed in the region shown in red points in Figure 47. Red data points in the unit stereographic triangle is analyzed to locate the positions on the deformed surface image. It is shown that the data points that were not correctly captured using the CP-FEM model corresponds to grain boundaries. Thus, it shows that the model does not properly capture the plastic incompatibilities near the grain boundaries at high strains.

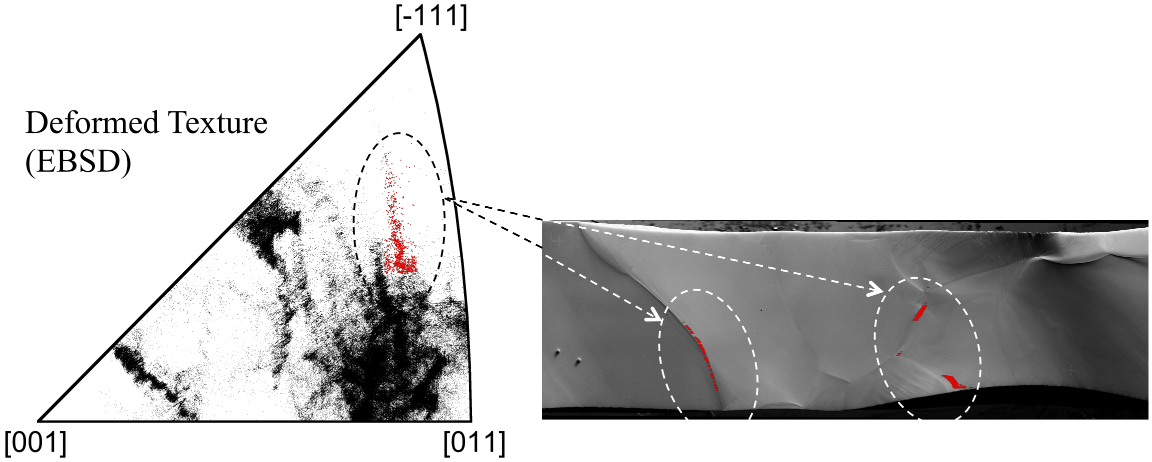

Figure 47. Deformed texture at 19.2% straining where it deviates from the simulation in Specimen 2. It shows that the deviation in red points in inverse pole figure is the crystal orientations at the grain boundaries.

In order to understand the magnitude of the crystal rotation upon deformation, a distribution of crystal misorientation angle can be calculated. Given two crystal orientations, g_A and g_B, the misorientation between two crystal orientation, Δg, can be defined as follows [63]:

$$\Delta g_{AB} = g_B g_A^{-1} \tag{42}$$

The misorientation angle, Δg, can be represented in terms of a rotation axis, **n**, and an angle, θ, and the following relation holds:

$$\cos\theta = \frac{1}{2}\left(\Delta g_{11} + \Delta g_{22} + \Delta g_{33} - 1\right) \tag{43}$$

Using Equations (42) and (43), distributions of the misorientation angle, θ, are plotted for specimen 1 using EBSD data and CP-FEM predictions as shown in Figure 48 (a). Here, the misorientation angle is obtained at 4.2 % strain relative to the initial crystal orientation (Points A to C in Figure 21 (b)). It is shown that the model captures a general trend of misorientation angle distributions upon deformation. Similar to strain field and texture analyses, sub-surface microstructure and grain boundary effects would be the possible reasons for deviations in measured and predicted misorienation angles. Figure 48 (b) shows a comparison of the deformed surface image and simulated misorientation angles relative to neighboring elements at 4.2 % applied strain. Note that θ in Figure 48 (b) represents misorientation angle between neighboring elements and is shown that misorientation angles exceeding 0.5 degrees are mostly near the grain boundaries.

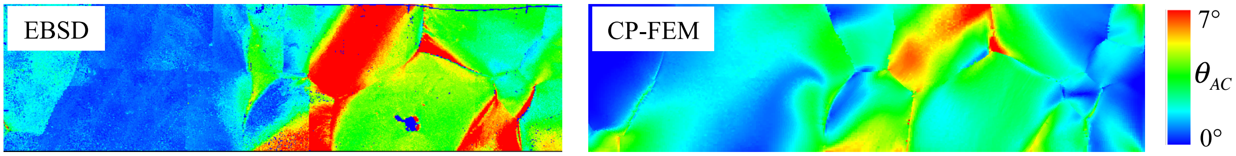

(a) Misorientation angles relative to the initial crystal orientation

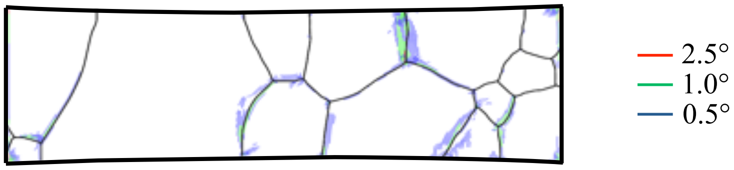

(b) Misorientation angles relative to neighboring elements

Figure 48. A comparison of misorientation angles. (a) Misorientation angles obtained from EBSD measurement and CP-FEM simulations at 4.2% strain (Point C) relative to the initial crystal orientation (Point A) and (b) misorientation angles relative to neighboring elements at 4.2% applied strain (Point C).

5.5 Failure Analysis

In uniaxial tension tests, specimen 2 is more severely deformed compared to specimen 1 and 3, up to 19.2% applied strain. At such strain, a necking occurred near the center of the gauge section as shown in front and top views of the deformed specimen 2 in Figure 49.

Figure 50 compare the surface image and simulated ε_{xx} of the specimen 2 at 19.2 % applied strain (Point E in Figure 21). At such large applied strain, a small notch and an irregular surface are developed at the top of the tensile specimen 2, as shown in Figures 50 (a) and (b). The location of the notch matches very well with the predicted locations with the highest ε_{xx}, from the side and the top views. On the other hand, the model do not accurately predicts observed deformed shape, especially as seen from the side view. This may due to stress relaxation at surface notch which cannot be captured using the FE model. On the other hand, displacements through the thickness is captured relatively well with the model (Figure 50 (b)).

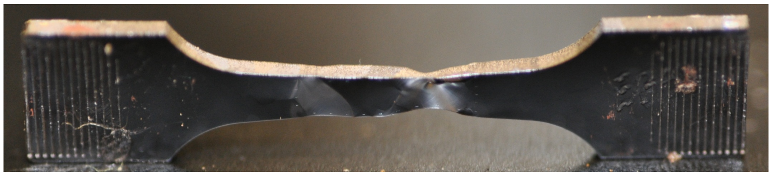

(a) Front view

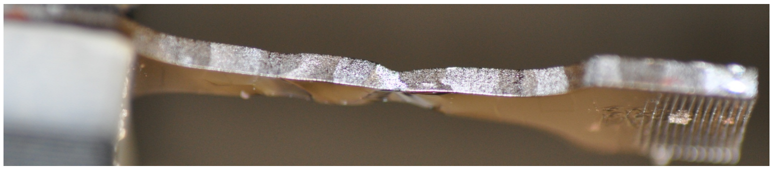

(b) Top view

Figure 49. Deformed specimen 2 at applied strain of 19.2%. (a) The front view and (b) the side view.

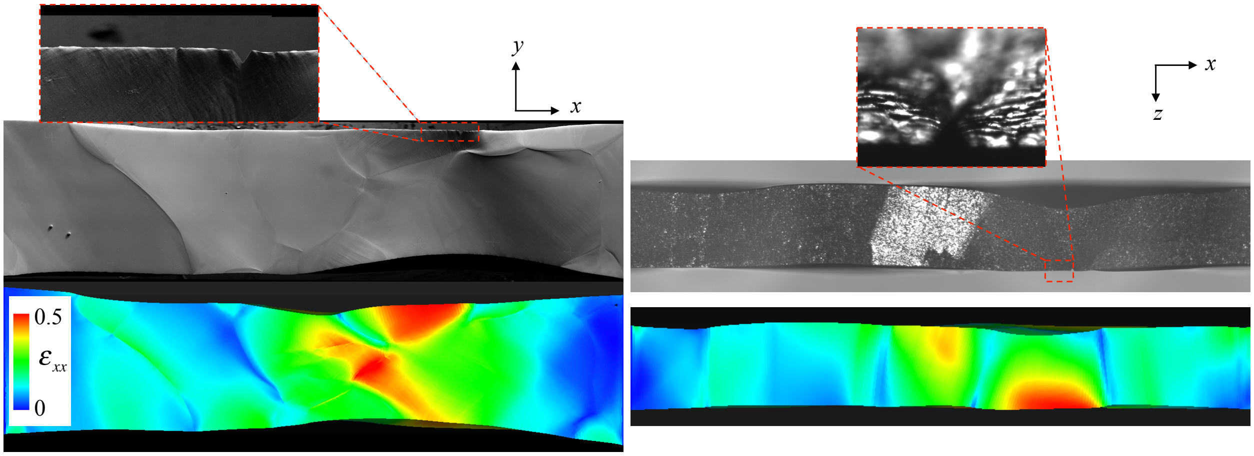

(a) Side view

(b) Top view

Figure 50. The surface image and simulated ε_{xx} of specimen 2 at 19.2 % applied strain (a) side view and (b) top view.

6 Discussion

In this section, we investigate various constitutive effects that would affect the model predictions, e.g. effects of the mesh, the choice of slip systems and the initial crystal orientations.

6.1 Mesh dependence

In FE-based simulations, different types and sizes of meshes may have a significant effect on the model predictions. Figure 51 shows the effect of mesh size on the prediction of deformed texture for specimen 2. Here, CP-FEM simulations using a coarse mesh having the total number of 207,000 elements are compared with the results in the previous section. The coarse mesh has approximately eight times smaller mesh, two times smaller in all three directions. As shown in Figures 51, predicted deformed texture show the same trend but having more elements in the simulation produced larger dispersion of crystal orientations, more similar to the EBSD measurement. Note that the total number of EBSD scans for specimen 2 is 754,236 while the total number of surface elements in the mesh is 33,283, about 20 times smaller.

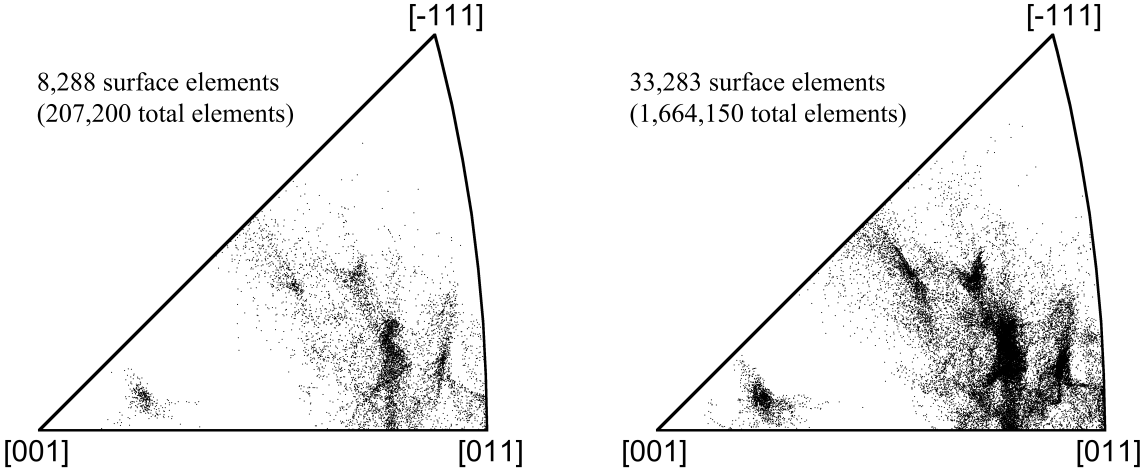

(a) Coarse mesh

(b) Fine mesh

Figure 51. Prediction of deformed texture of specimen 2 at the applied strain of 19.2 % using (a) a coarse mesh and (b) fine mesh.

In addition to in-plane mesh sizes, the number of elements through the thickness also affect CP-FEM predictions. In the simulations of materials in sheet form, 2D shell elements or a single 3D elements through the thickness are often adopted [14]. However it has been reported that multiple integration points through the thickness are required, e.g. 25 to 51 integration points are suggested to assure 1% numerical accuracy for in a large sheet metal forming simulations [68, 101]. In order to see how the through thickness elements affect the results in columnar oligocrystal simulations, previous results (50 elements through the thickness) are compared with predictions using a same surface mesh but having a single element through the thickness.

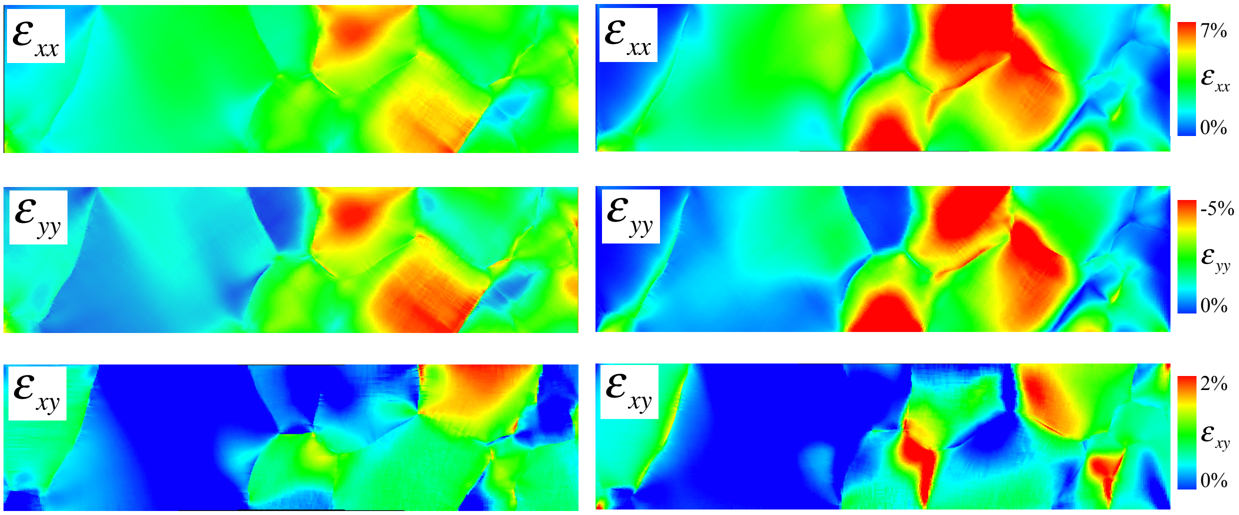

(a) Predicted strain map (2D)

(b) Predicted strain map (3D)

Figure 52. A comparison of predicted ε_{xx}, ε_{yy} and ε_{xy} distributions for specimen 1 at $\Delta\varepsilon_{CD}$=3.4 % deformation using (a) a single element through the thickness and (b) 50 elements through the thickness.

Figures 52 (a) and (b) compare predicted strain distributions of specimen 1 at $\Delta\varepsilon_{CD}$=3.4% using a single and 50 elements through the thickness. Although adopting a single element through the thickness captures the regions where large and small strain fields are observe, much better agreement with the DIC data is obtained when many elements through the thickness is adopted.

Figures 53 compares simulated texture of specimen 2 at the applied strain of 19.2 % using a single and 50 elements through the thickness. 2D and 3D simulations predict different deformed textures, and texture is more accurately captured with many elements through the thickness. This different attribute to stress variation through the thickness that cannot be accurately captured using a single element through thickness. This effect is clearly shown strain map distribution in Figure 50 (b). Note that these oligocrystals have relatively low height to thickness ratios and thus cannot ignore significant through thickness strain and stress distributions.

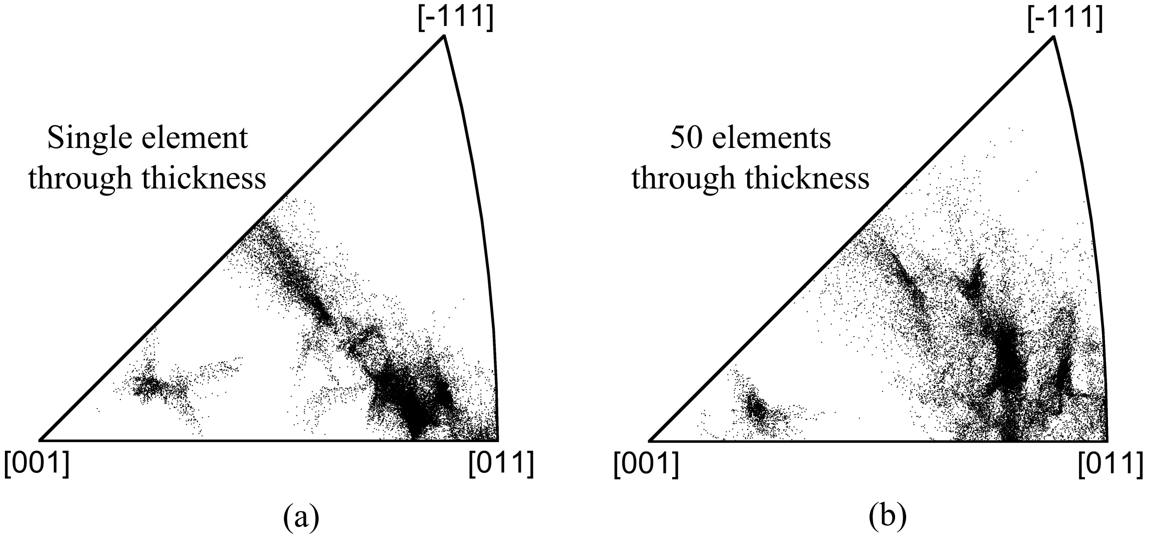

Figure 53. Deformed texture using (a) a single element through the thickness and (b) 50 elements through the thickness.

6.2 Effects of Initial Crystal Orientations

EBSD data of the undeformed specimen is usually used to inform the crystal orientations of each grain and used as an input in the simulation. Each grain is defined by some arbitrary grain boundary criteria, e.g. 3 degrees between scan points, and the average crystal orientation is obtained for each grain. In typical poly- and oligo-crystal FE simulations, many elements represent a single grain and elements representing the same grain are typically assigned with a single averaged crystal orientation. Thus, a small variation of crystal orientations within a grain are ignored. Alternatively, we can assign each element with crystal orientations without an averaged scheme, e.g. crystal orientations per element. Although the latter model has a advantage that a small variation within a grain may be captured and reproduces realistic initial microstructure, it is difficult to separate effects of experimental scatter and the actual orientation deviation within a grain.

In order to investigate the effect of initial crystal orientations, Figures 54 - 56 compare deformed textures of specimens 1 and 2 using two schemes: (a) a crystal orientation per grain and (b) a crystal orientation per element. For a crystal orientation per grain, the total number of initial crystal orientations used in the simulation equal to the total number of grains, 15 for specimen 1 and 17 for specimen 2, while the case (b), the total number of the initial crystal orientations equal to the total number of surface elements. As shown in Figures 54 and 55, a wave-like pattern is observed in the case of having a single crystal orientation per grain. On the other hand, having a scattered initial orientations showed more dispersed deformed texture and did not show wave lines. However, the difference in treating the initial texture did not changes the trend of deformed texture as shown in the intensity plots (Figures 56). It is very difficult to separate the effect of the measurement error or the actual distribution of the crystal orientation. It is likely that both affect the scattered initial distributions.

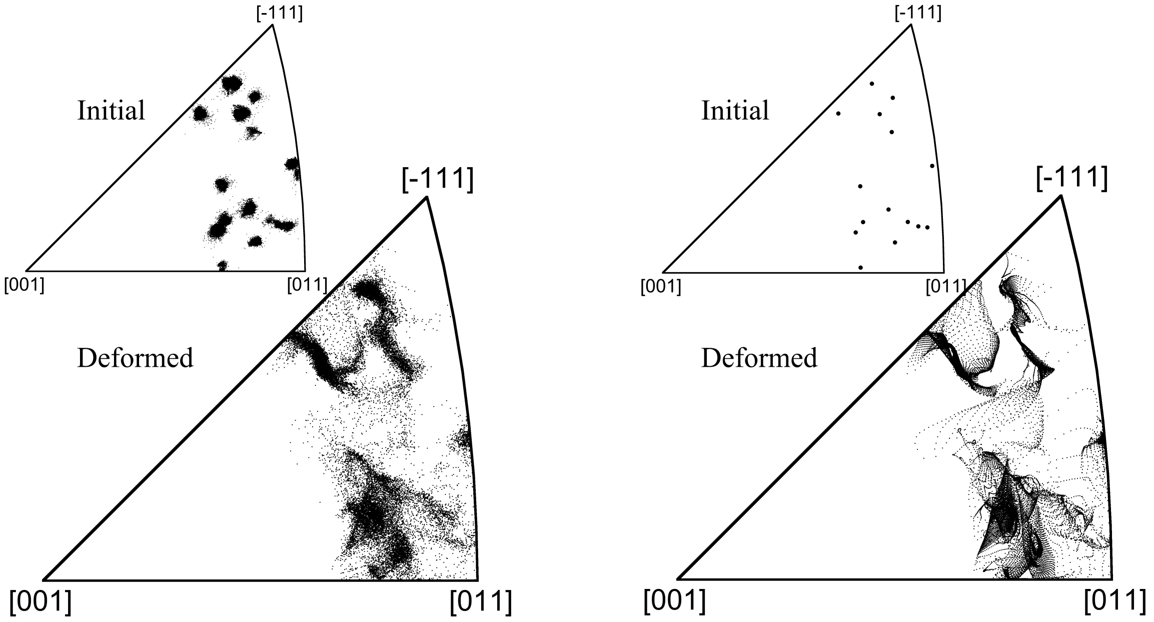

(a) Orientation per element

(b) Orientation per grain

Figure 54. Effects of initial crystal orientations on texture evolution for specimen 1 at 6.8% applied strain.. (a) One initial orientation per grain and (b) one initial orientation per element.

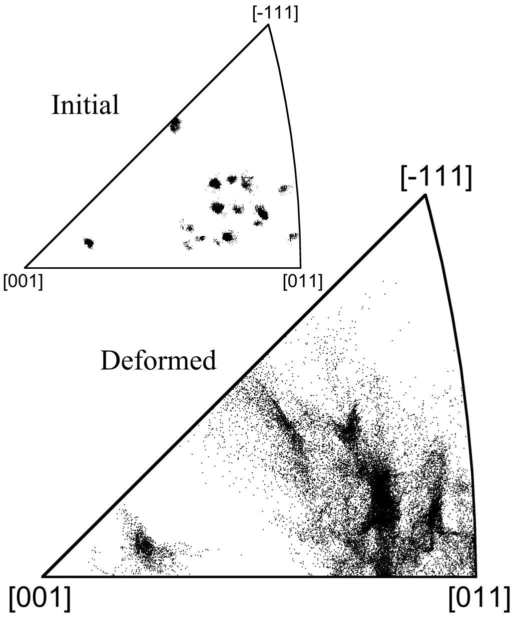

(a) Orientation per element

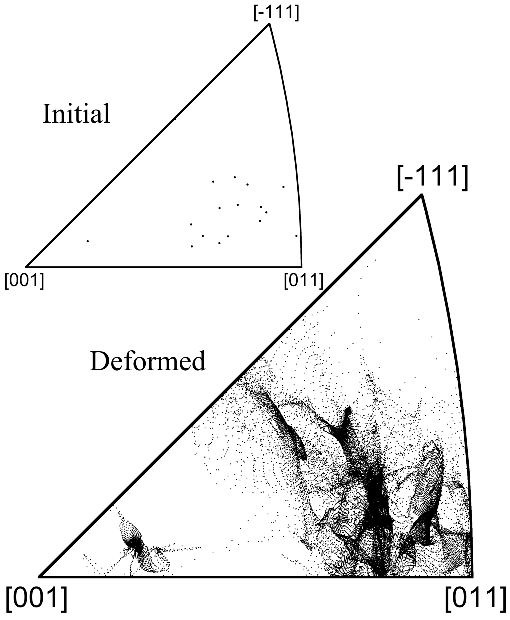

(b) Orientation per grain

Figure 55. Effects of initial crystal orientations on texture evolution for specimen 2 at 19.2% applied strain. (a) One initial orientation per grain and (b) one initial orientation per element.

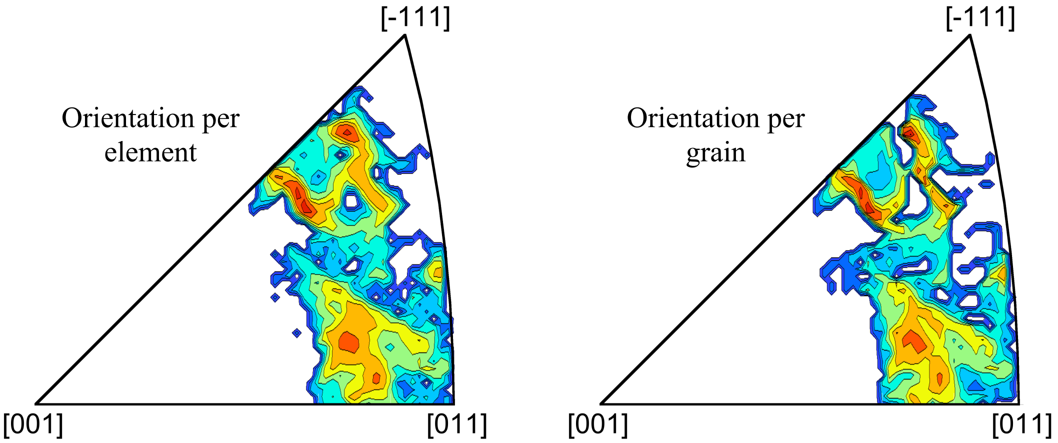

(a) Specimen 1 (6.8% deformation)

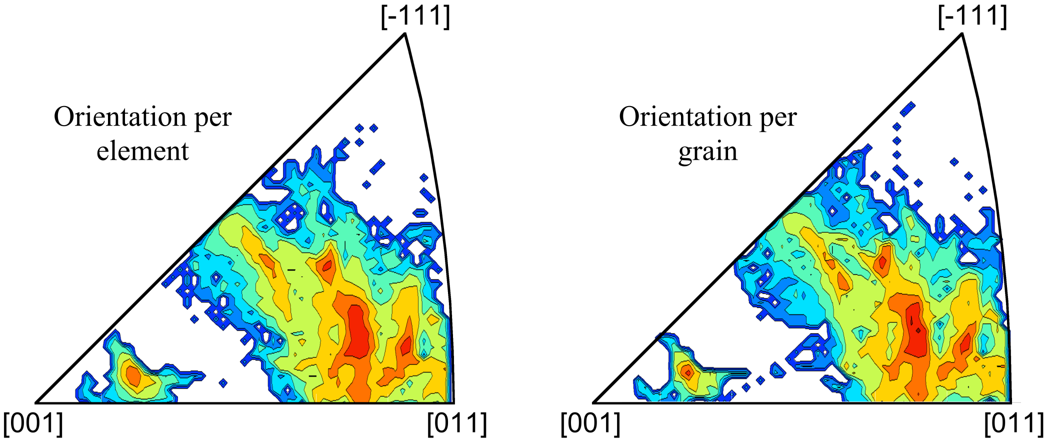

(a) Specimen 2 (19.2 % deformation)

Figure 56. Effects of initial crystal orientations on texture evolution for specimens 1 and 2. Contours represent measured intensity of crystal orientations.

Figure 57 compares misorientation angles using two schemes. Similar to texture predictions, two schemes in the initial crystal orientations make little difference and more continuous misorientations are observed where each element was assigned with different initial crystal orientations.

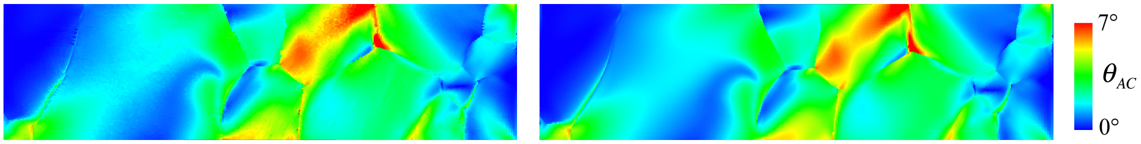

(a) CP-FEM, orientation per element (b) CP-FEM, orientation per grain

Figure 57. Predicted misorientation angles using different initial crystal orientations. (a) Crystal orientation per element and (b) crystal orientation per grain.

Also note that the initial treatment do not significant effect on predicting strain field predictions as shown in Figure 58. Thus, these results illustrate that small deviations in crystal orientations within the grain do not significantly affect texture and strain distributions.

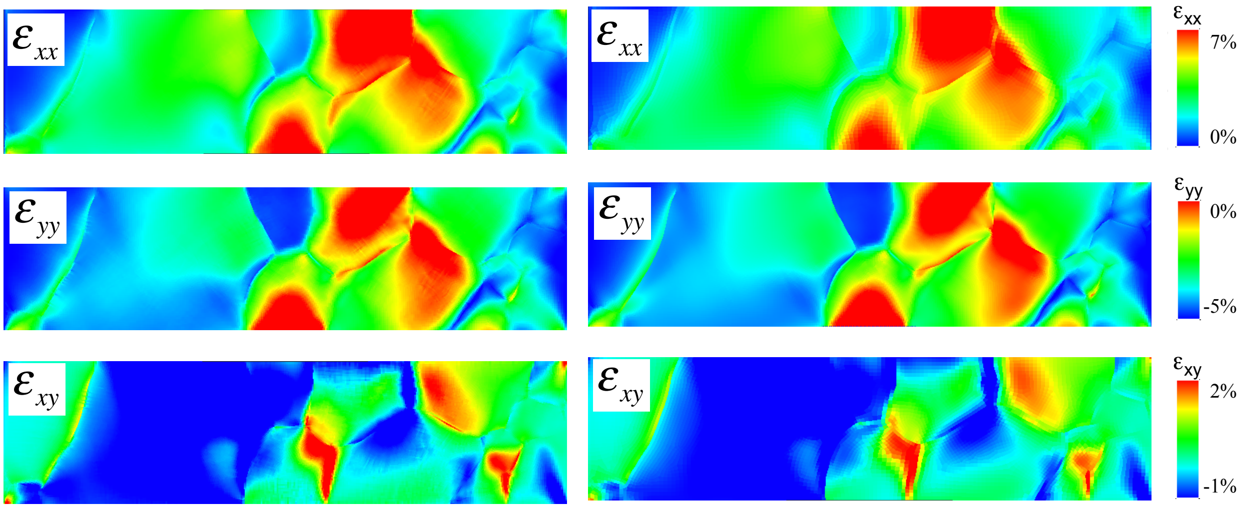

(a) Crystal orientation per element (b) Crystal orientation per grain

Figure 58. A plot of ε_{xx}, ε_{yy} and ε_{xy} obtained from CP-FEM simulations of specimen 1 at $\Delta\varepsilon_{CD} = 3.4\%$ using (a) crystal orientation per element and (b) crystal orientation per grain.

6.3 $\{110\}$ versus $\{112\}$ slip

In FCC metals, slip generally occurs in $\langle 110\rangle$ directions in $\{111\}$planes. In BCC metals, slip occurs along $\langle 111\rangle$directions but the slip planes that dislocations move are not well-defined. Although many atomistic simulations and experiments support $\{110\}$ slip for tantalum at room temperature [104, 26], $\{112\}$ slip is observed or predicted in various BCC metals as well. Figure 59 shows surface images of deformed specimen 1 and 2 and corresponding slip traces. Here, black lines represent the observed slip lines while the red and blue lines denote the projected $\{110\}$ and $\{112\}$ slip traces. In agreement with previous conclusion with specimen 1 [26], observed slip lines agree well with projected slip traces for $\{110\}$ slip systems for specimen 2 as well.

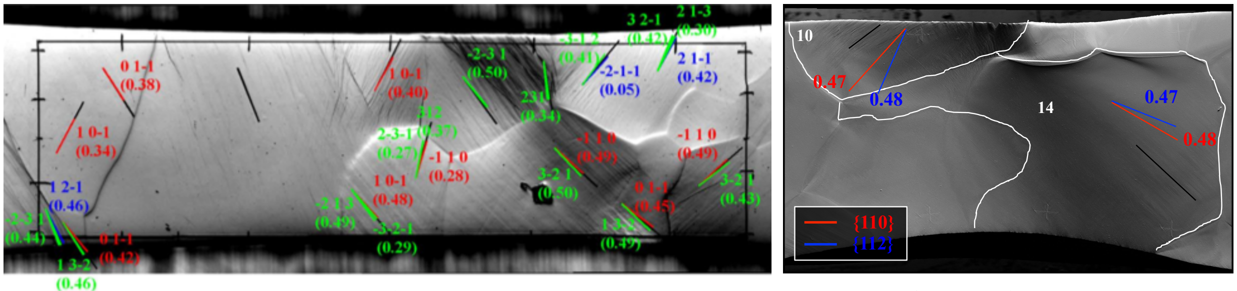

(a) Specimen 1

(b) Specimen 2

Figure 59. Surface images showing the slip lines and projected $\{110\}$ and $\{112\}$ slip traces for (a) specimen 1 at 0.8% applied strain [26] and (b) specimen 2 at 19.2% applied strain.

Figure 60 (a) illustrates the maximum Schmid factors of single crystals for $\{110\}$ and $\{112\}$ slip systems within the standard stereographic triangle. Depending on type of the slip planes that slip occurs, stress projection at different crystal orientations can be different. Thus, it will change the prediction of the yield stress of the material for different crystal orientations. In addition to crystal orientation dependent yield stress, crystal rotation upon uniaxial tension and compression show different paths depending on active slip planes as shown in Figure 60 (b).

In order to investigate the effects of different slip systems on CP-FEM predictions, two oligocrystal specimens, 1 and 2, are simulated using 24 $\{112\}$ slip systems while all other material parameters are kept the same as $\{110\}$ slip simulations. Table 11 lists 24 $\{112\}$ slip systems used in the simulation.

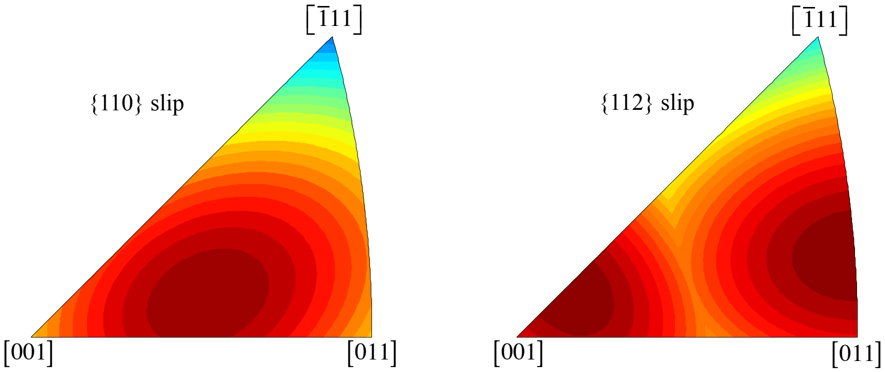

(a) The maximum Schmid factors

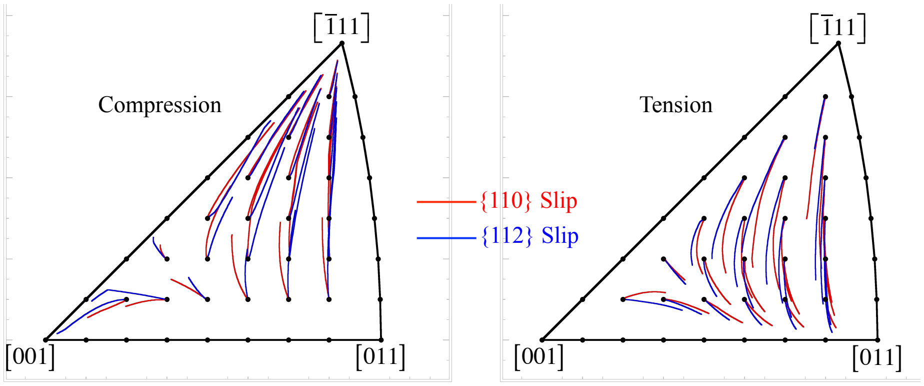

(b) Single crystal rotations upon isochoric deformation

Figure 60. (a) The maximum Schmid factors in {110} and {112} slip systems and (b) single crystal rotations under isochoric deformations in uniaxial compression and tension.

Table 11. The twenty-four {112} slip systems.

α	Slip System	α	Slip System	α	Slip System	α	Slip System
1	$(11\bar{2})[111]$	7	$(\bar{1}\bar{1}\bar{2})[\bar{1}\bar{1}1]$	13	$(11\bar{2})[\bar{1}\bar{1}\bar{1}]$	19	$(\bar{1}\bar{1}\bar{2})[11\bar{1}]$
2	$(\bar{2}11)[111]$	8	$(2\bar{1}1)[\bar{1}\bar{1}1]$	14	$(\bar{2}11)[\bar{1}\bar{1}\bar{1}]$	20	$(2\bar{1}1)[11\bar{1}]$
3	$(1\bar{2}1)[111]$	9	$(\bar{1}21)[\bar{1}\bar{1}1]$	15	$(1\bar{2}1)[\bar{1}\bar{1}\bar{1}]$	21	$(\bar{1}21)[11\bar{1}]$
4	$(\bar{1}1\bar{2})[\bar{1}11]$	10	$(1\bar{1}\bar{2})[1\bar{1}1]$	16	$(\bar{1}1\bar{2})[1\bar{1}\bar{1}]$	22	$(1\bar{1}\bar{2})[\bar{1}1\bar{1}]$
5	$(\bar{1}\bar{2}1)[\bar{1}11]$	11	$(121)[1\bar{1}1]$	17	$(\bar{1}\bar{2}1)[1\bar{1}\bar{1}]$	23	$(121)[\bar{1}1\bar{1}]$
6	$(211)[\bar{1}11]$	12	$(\bar{2}\bar{1}1)[1\bar{1}1]$	18	$(211)[1\bar{1}\bar{1}]$	24	$(\bar{2}\bar{1}1)[\bar{1}1\bar{1}]$

Figure 61 compares measured ε_{xx} using DIC with the maximum Schmid factors of each grain for $\{110\}$ and $\{112\}$ slip systems. It is expected to have a strong correlation between ε_{xx} and the maximum Schmid factor in the simulation. In accordance with previous studies by Carroll et al. [26], stronger correlations between the axial strain and the maximum Schmid factor for $\{110\}$ slip are observed for both specimen 1 and 2 at the room temperature. For example, in $\{112\}$ slip case, the maximum Schmid factors for grains 6, 7, 10 and 11 in specimen 1 and grains 12, 13, 15, 16, and 17 in specimen 2 are relatively large while measured ε_{xx} are small.

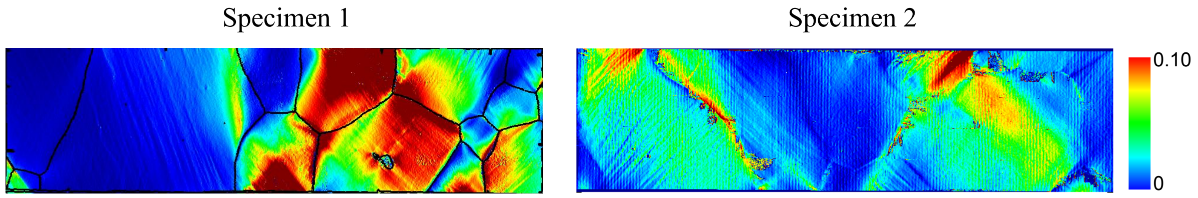

(a) Measured ε_{xx} (DIC)

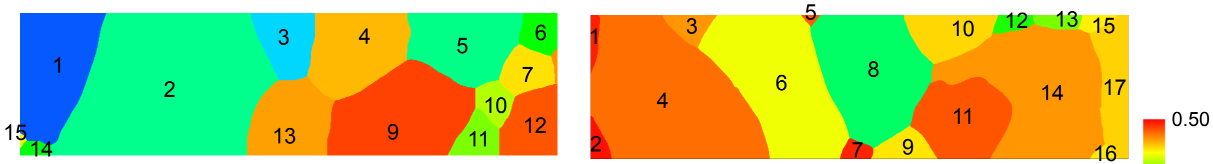

(b) Maximum Schmid Factor: $\{110\}$ slip

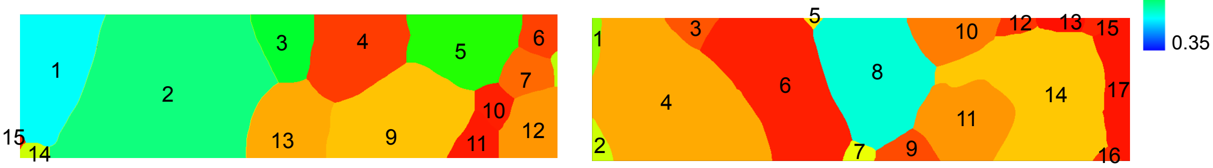

(c) Maximum Schmid Factor: $\{112\}$ slip

Figure 61. A plot of (a) ε_{xx} obtained from the DIC measurement (b) the maximum Schmid factors for $\{110\}$ slip systems and (c) the maximum Schmid factors for $\{112\}$ slips for specimen 1 and 2, respectively.

Figure 62 shows measured and predicted strain fields of specimen 1 at $\Delta\varepsilon_{CD}$=3.4 % (Point C to D). Although Schmid analysis showed relatively large difference in the maximum Schmid factors for many grains, predicted strain map showed similar distribution for both slip systems. Figure 63 compares predicted ε_{xx} for specimen 2 at 19.2% applied strain. In contrast to surface strain field analysis of specimen 1 in Figure 62, noticeable deviation between $\{110\}$ and $\{112\}$ predictions are observed for specimen 2, at large applies strain. Comparing predicted ε_{xx} and observed notch in specimen 2, it is shown that the predictions using the $\{110\}$ slip agrees better than $\{112\}$ slip.

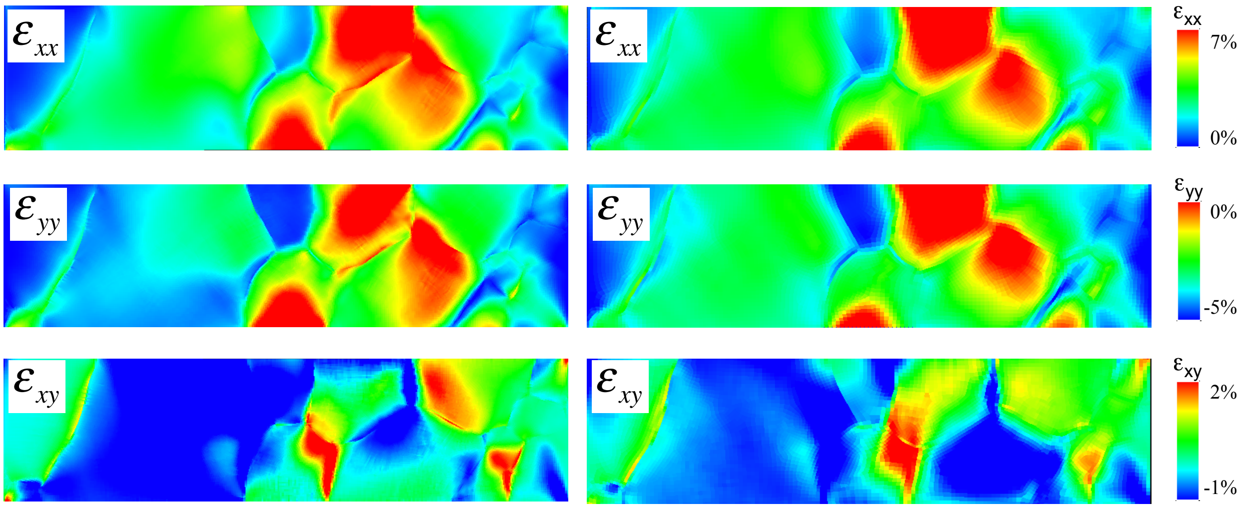

(a) {110} slip system (b) {112} slip system

Figure 62. A comparison of predicted ε_{xx}, ε_{yy} and ε_{xy} maps for specimen 1 at $\Delta\varepsilon_{CD}$=3.4 % (Point C to D). Predictions using (a) {110} slip and (b) {112} slip.

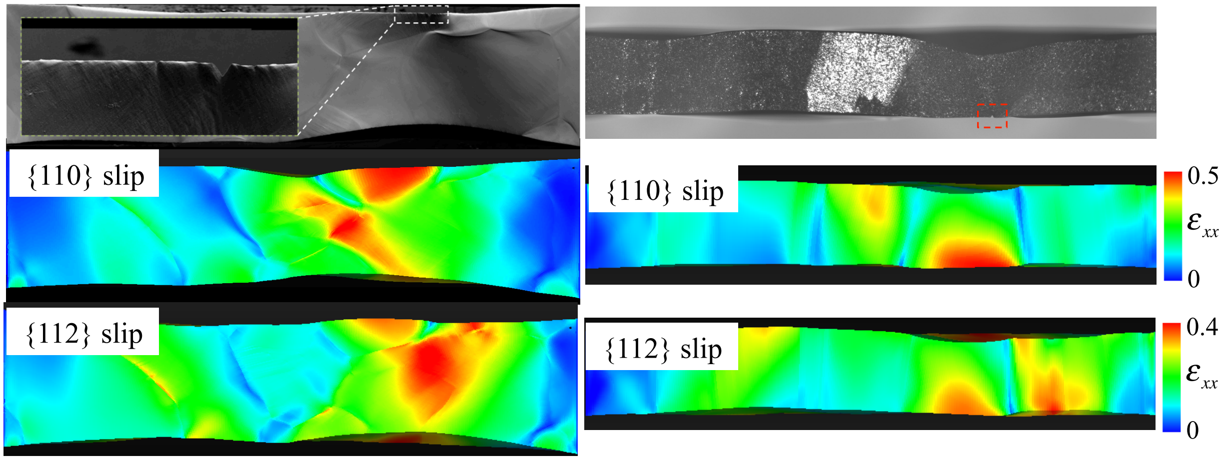

(a) Side view (b) Top view

Figure 63. Deformed specimen and simulated ε_{xx} of specimen 2 at 19.2 % applied strain for {110} and {112} slips. (a) Side view and (b) top view.

Figures 64 (a) and (b) compare images of deformed specimen and simulated shapes using $\{110\}$ and $\{112\}$ slip systems. It is shown that both $\{110\}$ and $\{112\}$ slip accurately predicts deformed shape of specimen 1 at 6.8 % straining while more deviations are observed for specimen 2 at 19.2 % deformation. At large deformation (specimen 2), CP-FEM simulations failed to accurately predict deformed shape, mainly due to crack initiation at the specimen surface.

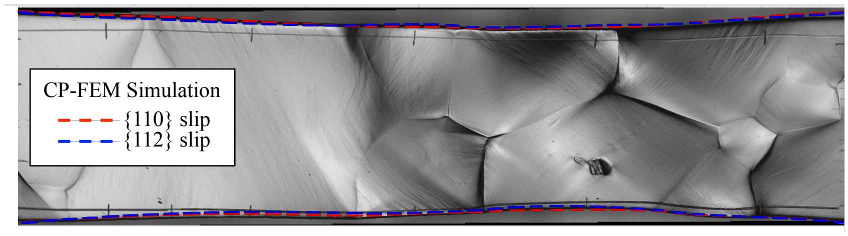

(a) Specimen 1

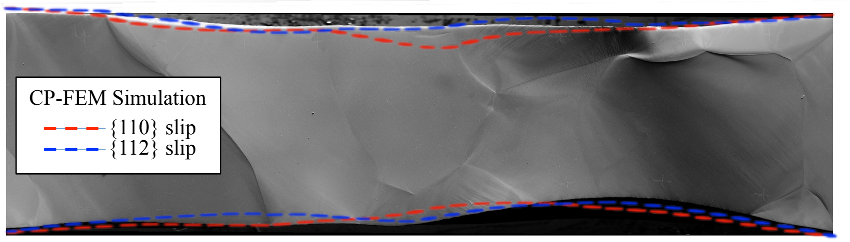

(b) Specimen 2

Figure 64. Deformed specimen and simulated shape of specimens for $\{110\}$ and $\{112\}$ slip. (a) Specimen 1 at 6.8 % and (b) Specimen 2 at 19.2 %.

The choice of slip systems are more sensitive in texture predictions as shown in Figure 65. Figures 65 (a) and (b) compare texture predictions using $\{110\}$ and $\{112\}$ slips for specimen 2 at 19.2 % deformation. It is observed that the prediction using $\{110\}$ slip agree better with measured texture from EBSD. Figure 66 compares predicted misorientation angles of specimen 1 relative to the initial orientations using $\{110\}$ and $\{112\}$ slip systems at 4.2 % applied strain. CP-FEM simulations using $\{110\}$ and $\{112\}$ slip system show similar trend in crystal rotations but $\{112\}$ predicted larger rotations.

A series of comparisons between measured and predicted quantities such as Schmid factors, strain distributions, deformed shapes and texture evolution, suggest that it is difficult to conclusively determine the favored slip systems. It is shown that macro-scale observations, such as DIC strain measurements and deformed shape are relatively less sensitive to the choice of slip systems. On the other hand, experimental measurements at smaller scales, e.g. texture evolution, is more sensitive to assumptions made in the simulation.

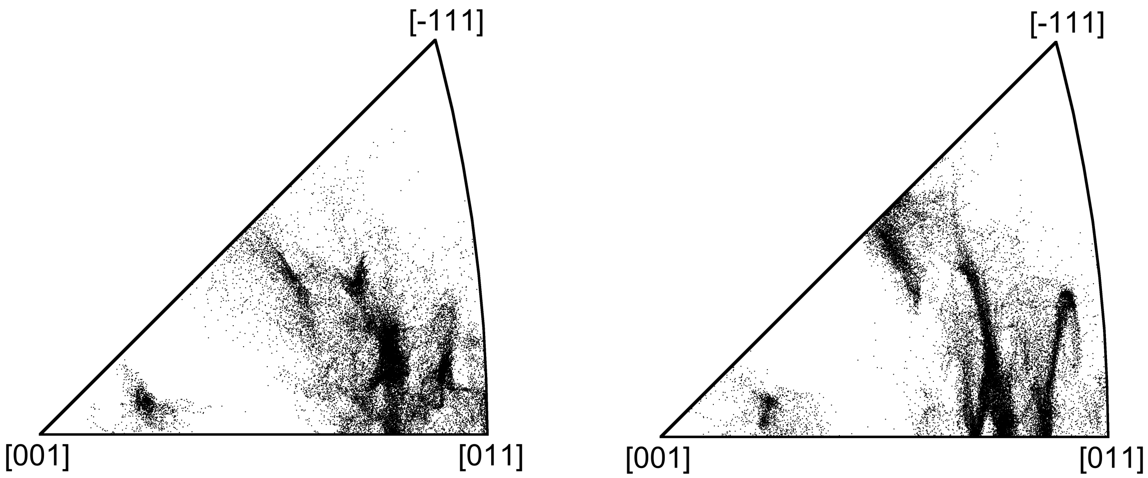

(a) {110} slip system (b) {112} slip system

Figure 65. Effects of slip systems on texture evolutions. (a) {110} slip and (b) {112} slip.

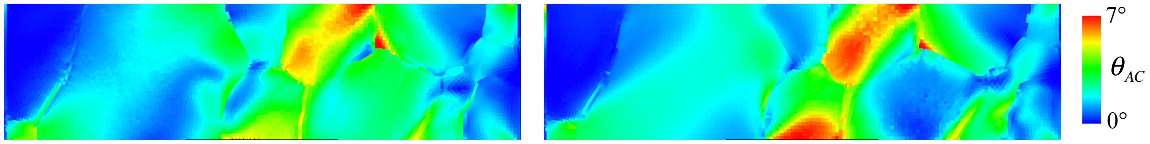

(a) CP-FEM, {110} slip (b) CP-FEM, {112} slip

Figure 66. Predicted disorientation angles relative to initial crystal orientations at 4.2 % applied strain using different slip systems. (a) {110} slip systems and (b) {112} slip systems.

7 Conclusions

In this work, we developed multi-scale computational model for tantalum. The dislocation kink-pair theory is used to incorporate temperature and strain rate dependent flow behaviors of single crystal tantalum and the model is calibrated to single crystal experiments. A BCC crystal plasticity finite element model developed from dislocation kink-pair theory accurately captures temperature and strain rate dependent yield stresses of single crystal tantalum. Simulated yield stresses of polycrystalline tantalum are fit to three continuum constitutive formulations that model flow stresses at high temperatures and strain rates. These models, when calibrated to CP-FEM simulations, can be used to predict yield behavior of polycrystals without the need to perform expensive, direct CP-FEM simulations. The Mechanical Threshold Stress model is found to reproduce the simulated yield stresses of polycrystal BCC metals most accurately. The MTS model fit to the dislocation kink pair theory in Taylor impact tests showed excellent agreement with experimental data. In order to further validate the proposed model, CP-FEM simulations of tantalum oligocrystals are compared directly to EBSD and DIC experiments. It is shown that both strain fields and texture predictions using CP-FEM model agreed well with measured data.

The framework developed in this work provides a method to connect dislocation physics to the continuum scale models. In particular, meso-scale simulation technique used in this work, BCC CP-FEM model, allows microstructure-informed, predictive computational capability to enable more realistic engineering scale simulations of polycrystalline metals for a variety of applications.

References

[1] H. Abdolvand and M. R. Daymond. Multi-scale modeling and experimental study of twin inception and propagation in hexagonal close-packed materials using a crystal plasticity finite element approach - Part I: Average behavior. *J. Mech. Phys, Sol.*, 61:783–802, 2013.

[2] F. Ackermann, H. Mughrabi, and A. Seeger. Temperature- and strain-rate dependence of the flow stress of ultrapure niobium single crystals in cyclic deformation. *Acta. Metall.*, 31:1353–1366, 1983.

[3] M. A. Adams and A. Iannucci. The mechanical properties of tantalum with special reference to the ductile-brittle transition. *ASD Technical Report*, pages 61–203, 1961.

[4] A. Alankar, D. P. Field, and D. Raabe. Plastic anisotropy of electro-deposited pure α-iron with sharp crystallographic $< 111 >$ texture in normal direction: Analysis by an explicitly dislocation-based crystal plasticity model. *Int. J. Plast.*, 52:18–32, 2014.

[5] L. Anand. Constitutive equations for hot working of metals. *Int. J. Plast.*, 1:213–231, 1985.

[6] L. Anand and S. R. Kalidindi. The process of shear-band formation in plane- strain compression of fcc metals - effects of crystallographic texture. *Mech. Materials*, 17:223–243, 1994.

[7] Y. Aoyagi, R. Kobayashi, Y. Kaji, and K. Shizawa. Modeling and simulation on ultrafine-graining based on multiscale crystal plasticity considering dislocation patterning. *Int. J. Plast.*, 47:13–28, 2013.

[8] Y. Aoyagi, T. Tsuru, and T. Shimokawa. Crystal plasticity modeling and simulation considering the behavior of the dislocation source of ultrafine-grained metal. *Int. J. Plast.*, 55:18–32, 2014.

[9] A. Argon. *Strengthening mechanisms in crystal plasticity*. Oxford University Press, 2008.

[10] R. J. Asaro. Micromech. crystals and polycrystals. *Adv. Appl. Mech.*, 23:1–115, 1983.

[11] R. J. Asaro and A. Needleman. Texture development and strain hardening in rate dependent polycrystals. *Acta Metall.*, 33:923–953, 1985.

[12] R. J. Asaro and J. R. Rice. Strain localization in ductile single crystals. *J. Mech. Phys. Sol.*, 25:309–338, 1977.

[13] D. J. Bacon, D. M. Barnett, and R. O. Scattergood. Anisotropic continuum theory of lattice defects. *Prog. Mater. Sci.*, 23:51–262, 1979.

[14] C. Badulescu, M. Grédiac, H. Haddadi, J.-D. Mathias, X. Balandraud, and H.-S. Tran. Applying the grid method and infrared thermography to investigate plastic deformation in aluminium multicrystal. *Mech. Mater.*, 43:36–53, 2011.

[15] D. M. Barnett, R. J. Asaro, S. D. Gavazza, D. J. Bacon, and R. O. Scattergood. The effects of elastic anisotropy on dislocation line tension in metals. *J. Phys. F: Metal Phys.*, 2:854–864, 1972.

[16] C. C. Battaile, L. N. Brewer, J. M. Emery, and B. L. Boyce. Quantifying uncertainty from material inhomogeneity. *SAND2009-6169*, 2009.

[17] J. H. Biffle. *A three-dimensional finite element computer program for the nonlinear quasi-static response of solids with the conjugate gradient method, SAND87-1305*. Sandia National Laboratories, 1987.

[18] B. L. Boyce, B. G. Clark, P. Lu, J. D. Carroll, and C. R. Weinberger. The morphology of tensile failure in tantalum. *Metall. Mater. Trans. A-Phys. Metall. Mater. Sci.*, 44:4567–4580, 2013.

[19] C. A. Bronkhorst, S. R. Kalidindi, and L. Anand. Polycrystalline plasticity and the evolution of crystallographic texture in fcc metals. *Philos. Trans. Roy. Soc. London A*, 341:443, 1992.

[20] D. Brunner. Comparison of flow-stress measurements on high-purity tungsten single crystals with the kink-pair theory. *Mater. Trans. JIM*, 41:152–160, 2000.

[21] D. Brunner and J. Diehl. Strain-rate and temperature dependence of the tensile flow stress of high-purity α-iron above 250 K (regime I) Studied by means of stress-relaxation tests. *Phys. Status Solidi A*, 124:155–170, 1991.

[22] M. Z. Butt. Kinetics of flow stress in crystals with high intrinsic lattice friction. *Philos. Mag.*, 87:3595–3614, 2007.

[23] D. Caillard and J. L. Martin. *Thermally activated mechanisms in crystal plasticity*. Pergamon, 2003.

[24] J. D. Carroll, W. Abuzaid, J. Lambros, and H. Sehitoglu. An experimental methodology to relate local strain to microstructural texture. *Rev. Sci. Instrum.*, 81:083703, 2010.

[25] J. D. Carroll, L. N. Brewer, C. C. Battaile, B. L. Boyce, and J. M. Emery. The effect of grain size on local deformation near a void-like stress concentration. *Int. J. Plast.*, 39:46–60, 2012.

[26] J. D. Carroll, B. G. Clark, T. E. Buchheit, B. L. Boyce, and C. R. Weinberger. An experimental statistical analysis of stress projection factors in bcc tantalum. *Mat. Sci. Eng. A*, 581:108–118, 2013.

[27] V. Celli, M. Kabler, T. Ninomiya, and R. Thomson. Theory of dislocation mobility in semiconductors. *Phys. Rev.*, 131:58–72, 1963.

[28] C. Q. Chen, G. Hu, J. N. Florando, M. Kumar, K. J. Hemker, and T. K. Ramesh. Interplay of dislocation slip and deformation twinning in tantalum at high strain rates. *Scripta Mater.*, 69:709–712, 2013.

[29] S. R. Chen and G. T. Gray. Constitutive behavior of tantalum and tantalum-tungsten alloys. *Met. Mater. Trans. A*, 27:2994–3005, 1996.

[30] J. Cheng, S. Nemat-Nasser, and W. Guo. A unified constitutive model for strain-rate and temperature dependent behavior of molybdenum. *Mech. Mat.*, 33:603–616, 2001.

[31] K. Cheong and E. P. Busso. Effects of lattice misorientations on strain heterogeneities in fcc polycrystals. *J. Mech. Phys. Sol.*, 54:671–689, 2006.

[32] J. W. Christian. Some surprising features of the plastic deformation of body-centered-cubic metals and alloys. *Met. Trans. A*, 14A:1237–1256, 1983.

[33] W. Counts, M. Braginsky, C. Battaile, and E. Holm. Predicting the Hall-Petch effect in fcc metals using non-local crystal plasticity. *Int. J. Plast.*, 24:1243–1263, 2008.

[34] P. R. Dawson. Computational crystal plasticity. *Int. J. Sol. Struct.*, 37:115–130, 2000.

[35] P. R. Dawson, S. R. MacEwen, and P. D. Wu. Advances in sheet metal forming analyses: dealing with mechanical anisotropy from crystallographic texture. *Int. Mater. Rev.*, 48:86–122, 2003.

[36] F. Delaire, J. L. Raphanel, and C. Rey. Plastic heterogeneities of a copper multicrystal deformed in uniaxial tension: Experimental study and finite element simulations. *Acta Mater.*, 48:1075–1087, 2000.

[37] R. Dingreville, C. C. Battaile, L. N. Brewer, E. A. Holm, and B. L. Boyce. The effect of microstructural representation on simulations of microplastic ratcheting. *Int. J. Plast.*, 21:617–633, 2010.

[38] J. E. Dorn and S. Rajnak. Nucleation of kink pairs + Peierls mechanism of plastic deformation. *Trans. Metall. Soc. AIME*, 230:1052, 1964.

[39] M. S. Duesbery and V. Vitek. Plastic anisotropy in B.C.C. transition metals. *Acta. Mater.*, 46:1481–1492, 1998.

[40] J. D. Eshelby. The interactions of kinks with elastic waves. *Proc. R. Soc. Lond. A*, 266:222–246, 1962.

[41] P. S. Follansbee and U. F. Kocks. A constitutive description of the deformation of copper based on the use of the mechanical threshold stress as an internal state variable. *Acta metall.*, 1:81–93, 1988.

[42] C. Gérard, G. Cailletaud, and B. Bacroix. Modeling of latent hardening produced by complex loading paths in fcc alloys. *Int. J. Plast.*, 42:194–212, 2013.

[43] A. Godfrey, O. V. Mishin, and Q. Liu. Processing and interpretation of ebsd data gathered from plastically deformed metals. *Mater. Sci. Tech.*, 22:1263, 2006.

[44] D. M. Goto, J. F. Bingert, S. R. Chen, G. T. G. III, and R. K. Garrett. The mechanical threshold stress constitutive-strength model description of HY-100 steel. *Metall. Mater. Trans. A*, 31:1985–1996, 2000.

[45] M. Guyot and J. E. Dorn. A critical review of the Peierls mechanism. *Can. J. Phys.*, 43:983–1016, 1964.

[46] F. Havliček, J. Kratochvil, M. Tokuda, and V. Lev. Finite element model of plastically deformed multicrystal. *Int. J. Plast.*, 6:281–291, 1990.

[47] E. Héripré, M. Dexet, J. Crépin, L. Gélébart, A. Roos, M. Bornert, and D. Caldemaison. Coupling between experimental measurements and polycrystal finite element calculations for micromechanical study of metallic materials. *Int. J. Plast.*, 23:1512–1539, 2007.

[48] R. Hill and J. R. Rice. Constitutive analysis of elastic plastic crystals at arbitrary strain. *J. Mech. Phys. Sol.*, 20:401–413, 1972.

[49] J. Hirth and J. Lothe. *Theory of Dislocations*. Krieger, 1982.

[50] T. Hoc, J. Crépin, L. Gélébart, and A. Zaoui. A procedure for identifying the plastic behavior of single crystals from the local response of polycrystals. *Acta Mater.*, 51:5477–5488, 2003.

[51] K. G. Hoge and A. K. Mukherjee. The temperature and strain rate dependence of the flow stress of tantalum. *J. Mat. Sci.*, 12:1666–1672, 1977.

[52] L. Hollang, D. Brunner, and A. Seeger. Work hardening and flow stress of ultrapure molybdenum single crystals. *Mater. Sci. Eng. A*, 319:233–236, 2001.

[53] L. Hollang, M. Hommel, and A. Seeger. The flow stress of ultra-high-purity molybdenum single crystals. *Phys. Status Solidi A*, 160:329–354, 1997.

[54] J. W. Hutchinson. Bounds and self-consistent estimates for creep of polycrystalline materials. *Proc. R. Soc. Lond. A*, 348:101–127, 1976.

[55] G. R. Johnson and W. H. Cook. Fracture characteristics of three metals subjected to various strains, strain rates, temperatures and pressures. *Eng. Fract. Mech.*, 21:31–48, 1985.

[56] G. R. Johnson and W. J. Cook. A constitutive model and data for metals subjected to large strains, high strain rates and high temperatures. *Seventh International Symposium on Ballistics, The Hague, The Netherlands*, pages 541–547, 1983.

[57] S. R. Kalidindi, C. A. Bronkhorst, and L. Anand. Crystallographic texture evolution in bulk deformation processing of fcc metals. *J. Mech. Phys. Sol.*, 40:537, 1992.

[58] G. I. Kerley. CTH reference manual: The equation of state package. *Technical report SAND98-0947, Sandia National Laboratories, Albuquerque, NM*, 1998.

[59] A. S. Khan and R. Liang. Behaviors of three bcc metal over a wide range of strain rates and temperatures: experiments and modeling. *Int. J. Plast.*, 15:1089–1109, 1999.

[60] B. Klusemann, B. Svendsen, and H. Vehoff. Investigation of the deformation behavior of Fe-3%Si sheet metal with large grains via crystal plasticity and finite-element modeling. *Comp. Mater. Sci.*, 52:25–32, 2012.

[61] B. Klusemann, B. Svendsen, and H. Vehoff. Modeling and simulation of deformation behavior, orientation gradient development and heterogeneous hardening in thin sheets with coarse texture. *Int. J. Plast.*, 50:109–126, 2013.

[62] U. F. Kocks. Laws for work-hardening and low-temperature creep. *J. Eng. Mater. Tech., ASME*, 98:76–85, 1976.

[63] U. F. Kocks. *Textures and Anisotropy*, chapter 8, pages 326–389. Cambridge University Press, 1998.

[64] U. F. Kocks, A. S. Argon, and M. F. Ashby. Thermodynamics and kinetics of slip. *Prog. Mater. Sci.*, 19:1–289, 1975.

[65] E. H. Lee. Elastic-plastic deformation at finite strains. *Appl. Mech.*, 36:1–6, 1969.

[66] M. G. Lee, H. Lim, J. H. Kim, B. L. Adams, and R. H. Wagoner. A dislocation density-based single crystal constitutive equation. *Int. J. Plast.*, 26:925–938, 2010.

[67] A. M. Lennon and K. T. Ramesh. The thermoviscoplastic response of polycrystalline tungsten in compression. *Mat. Sci. Eng. A*, 276:9–21, 2000.

[68] K. P. Li, W. P. Carden, and R. H. Wagoner. Simulation of springback. *Int. J. Mech. Sci.*, 44:103–122, 2002.

[69] H. Lim, C. C. Battaile, J. D. Carroll, B. L. Boyce, and C. R. Weinberger. A physically based temperature and strain rate dependent crystal plasticity model for bcc metals. *J. Mech. Phys. Sol.*, 74:80–96, 2015.

[70] H. Lim, J. D. Carroll, C. C. Battaile, B. L. Boyce, and C. R. Weinberger. Quantitative comparison between experimental measurements and cp-fem predictions of plastic deformation in a tantalum oligocrystal. *Int. J. Mech. Sci.*, 92:98–108, 2015.

[71] H. Lim, L. M. Hale, Z. A. Zimmerman, C. C. Battaile, and C. R. Weinberger. A multiscale model of dislocation plasticity in α-Fe: Incorporating temperature, strain rate and non-schmid effects. *Int. J. Plast.*, 73:100–118, 2015.

[72] H. Lim, M. G. Lee, J. H. Kim, B. L. Adams, and R. H. Wagoner. Simulation of polycrystal deformation with grain and grain boundary effects. *Int. J. Plast.*, 27:1328–1354, 2011.

[73] H. Lim, C. R. Weinberger, C. C. Battaile, and T. E. Buchheit. Application of generalized non-Schmid yield law to low temperature plasticity in bcc transition metals. *Model. Simul. Mater. Sci. Eng.*, 21:045015, 2013.

[74] P. Ludwik. *Element der Technologischen Mechanik.* Springer, 1909.

[75] P. J. Maudlin, J. F. Bingert, J. W. House, and S. R. Chen. On the modeling of the Taylor cylinder impact test for orthotropic textured materials: experiments and simulations. *Int. J. Plast.*, 15:139–166, 1999.

[76] T. Mayama, M. Noda, R. Chiba, and M. Kuroda. Crystal plasticity analysis of texture development in magnesium alloy during extrusion. *Int. J. Plast.*, 27:1916–1935, 2011.

[77] L. E. Murr, M. A. Meyers, C. S. Niou, Y. H. Chen, S. Pappu, and C. Kennedy. Shock-induced deformation twinning in tantalum. *Acta Mater.*, 45:157–175, 1997.

[78] S. Narayanan, D. L. McDowell, and T. Zhu. Crystal plasticity model for bcc iron atomistically informed by kinetics of correlated kinkpair nucleation on screw dislocation. *J. Mech. Phys, Sol.*, 65:54–68, 2014.

[79] S. Nemat-Nasser and W. Guo. Flow stress of commercially pure niobium over a broad range of temperatures and strain rates. *Mater. Sci. Eng. A*, 284:202–210, 2000.

[80] S. Nemat-Nasser and W. Guo. High strain-rate response of commercially pure vanadium. *Mech. Mat.*, 32:243–260, 2000.

[81] S. Nemat-Nasser, W. Guo, and M. Liu. Experimentally-based micromechanical modeling of dynamic response of molybdenum. *Scripta Mater.*, 40:859–872, 1999.

[82] S. Nemat-Nasser and J. B. Isaacs. Direct measurement of isothermal flow stress of metals at elevated temperatures and high strain rates with application to ta and ta-w alloys. *Acta Mater.*, 45:907–919, 1997.

[83] S. Nemat-Nasser and R. Kapoor. Deformation behavior of tantalum and a tantalum tungsten alloy. *Int. J. Plast.*, 17:1351–1366, 2001.

[84] T. Ohashi, M. Kawamukai, and H. Zbib. A multiscale approach for modeling scale-dependent yield stress in polycrystalline metals. *Int. J. Plast.*, 23:897–914, 2007.

[85] C. H. Park, S. G. Hong, and C. S. Lee. A unified constitutive model for quasi-static flow responses of pure Ta and Ta-W alloys. *Mat. Sci. Eng. A*, 528:1154–1161, 2011.

[86] D. Peirce, R. J. Asaro, and A. Needleman. An analysis of nonuniform and localized deformation in ductile single crystals. *Acta Metall.*, 30:1087–1119, 1982.

[87] D. Raabe, Z. Z. M. Sachtleber, F. Roters, and S. Zaefferer. Micromechanical and macromechanical effects in grain scale polycrystal plasticity experimentation and simulation. *Acta Mater.*, 49:3433–3441, 2001.

[88] J. R. Rice. Inelastic constitutive relations for solids, an internal-variable theory and its application to metal plasticity. *J. Mech. Phys. Sol.*, 19:443–455, 1971.

[89] P. A. Sabnis, S. Forest, N. K. Arakere, and V. A. Yastrebov. Crystal plasticity analysis of cylindrical indentation on a Ni-base single crystal superalloy. *Int. J. Plast.*, 51:200–217, 2013.

[90] M. Sachtleber, Z. Zhao, and D. Raabe. Experimental investigation of plastic grain interaction. *Mat. Sci. Eng. A*, 336:81–87, 2002.

[91] A. Seeger. The temperature and strain-rate dependence of the flow stress of body-centered cubic metals: A theory based on kink–kink interactions. *Z. Metallikd*, 72:369–380, 1981.

[92] A. Seeger. The flow stress of high-purity refractory body-centered cubic metals and its modification by atomic defects. *J. Phys. IV*, 5:C7–45–C7–65, 1995.

[93] A. Seeger. Why anomalous slip in body-centred cubic metals? *Mater. Sci. Eng. A*, 319-321:254–260, 2001.

[94] A. Seeger and U. Holzwarth. Slip planes and kink properties of screw dislocations in high-purity niobium. *Philos. Mag.*, 86:3861–3892, 2006.

[95] G. Taylor. The use of flat-ended projectiles for determining dynamic yield stress. I. theoretical considerations. *Proc. R. Soc. Lond. A*, 194:289–299, 1948.

[96] G. Taylor. Thermally-activated deformation of BCC metals and alloys. *Prog. Mater. Sci.*, 36:29–61, 1992.

[97] G. I. Taylor. The mechanism of plastic deformation of crystals. Part I. Theoretical. *Proc. Roy. Soc. A*, 165:362–387, 1934.

[98] G. I. Taylor. Plastic strain in metals. *J. Inst. Metals*, 62:307–324, 1938.

[99] T. J. Turner, P. A. Shade, J. C. Schuren, and M. Groeber. The influence of microstructure on surface strain distributions in a nickel micro-tension specimen. *Modell. Sim. Mater. Sci. Eng.*, 21:015002, 2013.

[100] G. Z. Voyiadjis and F. H. Abed. A coupled temperature and strain rate dependent yield function for dynamic deformations of bcc metals. *Int. J. Plast.*, 22:1398–1431, 2006.

[101] R. H. Wagoner, H. Lim, and M. G. Lee. Advanced issues in springback. *Int. J. Plast.*, 45:3–20, 2013.

[102] H. Wang, P. Wu, J. Wang, and C. Tomé. A crystal plasticity model for hexagonal close packed (hcp) crystals including twinning and de-twinning mechanisms. *Int. J. Plast.*, 49:36–52, 2013.

[103] C. R. Weinberger, C. C. Battaile, T. E. Buchheit, and E. A. Holm. Incorporating atomistic models of lattice friction into bcc crystal plasticity models. *Int. J. Plast.*, 37:16–30, 2012.

[104] C. R. Weinberger, B. L. Boyce, and C. C. Battaile. Slip planes in bcc transition metals. *Int. Mater. Rev.*, 58:296–314, 2013.

[105] C. R. Weinberger, G. J. Tucker, and S. Foiles. The Peierls potential of screw dislocations in bcc transition metals: predictions form density functional theory. *Phys. Rev. B*, 87:054114, 2013.

[106] M. Werner. Temperature and strain-rate dependence of the flow stress of ultrapure tantalum single crystal. *Phys. Status Solidi A*, 104:63–78, 1987.

[107] T. Yalcinkaya, W. A. M. Brekelmans, and M. G. D. Geers. Bcc single crystal plasticity modeling and its experimental identification. *Modell. Simul. Mater. Sci. Eng.*, 16:085007, 2008.

[108] Z. Yao and R. H. Wagoner. Active slip in aluminum multicrystals. *Acta metall. mater.*, 41:451–468, 1993.

[109] N. Zaafarani, Raabe, R. Singh, F. Roters, and S. Zaefferer. Three-dimensional investigation of the texture and microstructure below a nanoindent in a Cu single crystal using 3D EBSD and crystal plasticity finite element simulations. *Acta Mater.*, 54:1863–1876, 2006.

[110] F. J. Zerilli and R. W. Armstrong. Dislocation-mechanics-based constitutive relations for material dynamics calculations. *J. Appl. Phys.*, 61:1816–1825, 1987.

[111] F. J. Zerilli and R. W. Armstrong. Description of tantalum deformation behavior by dislocation mechanics based constitutive relations. *J. Appl. Phys.*, 68:1580–1591, 1990.

[112] Z. Zhao, M. Ramesh, D. Raabe, A. Cuitiño, and R. Radovitzky. Experimental investigation of plastic grain interaction. *Int. J. Plast.*, 24:2278–2297, 2008.

[113] A. Ziegenbein, H. Neuhäuser, J. Thesing, R. Ritter, H. Wittich, E. Steck, M. Levermann, and E. Woldt. Local plasticity of Cu-AI polycrystals - measurements and FEM-simulation. *J. Phys. IV France*, 8:407–412, 1998.

DISTRIBUTION:

1	MS 0889	Corbett Battaile, 01814
1	MS 0889	Thomas Buchheit, 01814
1	MS 0889	Brad Boyce, 01831
1	MS 0889	Jay Carroll, 01831
1	MS 1411	Hojun Lim, 01814
1	MS 1411	Amy Sun, 01814
1	MS 0899	Technical Library, 09536

Sandia National Laboratories